THEORETICAL MAGNETOTELLURIC REPSONSE FOR SIMPLE THREE DIMENSIONAL MODELS

THEORETICAL MAGNETOTELLURIC RESPONSE FOR SIMPLE THREE DIMENSIONAL MODELS.

A Dissertation Presented to the Graduate Faculty of

Dedman College

of

Southern Methodist University

in

Partial Fulfillment of the Requirements

for the degree of

Doctor of Philosophy

in

Geophysics

by

Muhammad A. Daniyan

(B.Sc, Ahmadu Bello University, Nigeria, 1974)

(M.Sc, Ahmadu Bello University, Nigeria, 1978)

February 10, 1983.

Daniyan, Muhammad Abdullahi B.Sc., 1974, Ahmadu Bello University, Zaria, Nigeria.
M.Sc., 1978, Ahmadu Bello University, Zaria, Nigeria.

Theoretical Magnetotelluric Response for Simple Three Dimensional Models.
Advisor: Adjunct Professor Wayne J. Peeples.

Doctor of Philosophy degree conferred May 21, 1983.

Thesis completed February 10, 1983.

The magnetotelluric response for earth models with non-planar subsurface interfaces has been investigated. Partial differential equations obtained from Maxwell's equations and the constitutive relations were solved directly in order to obtain relations for the electromagnetic fields. The Rayleigh-FFT technique was used to compute the spectral coefficients of the fields in the wavenumber domain. This technique takes advantage of the Fast Fourier Transform which simplifies the calculation of the spectral coefficients. The reliability of the solutions was determined by comparing the results from the 3D program with 1D and 2D solutions obtained independently. The agreement is better than 0.1 percent. Mismatch of the boundary conditions at the non-planar interface was calculated to check the accuracy of the solution for 3D results. The magnetic and electric field components determined at the model's surface, impedances, apparent resistivities and dimensionality parameters such as skew and tipper were calculated for both resistive and

conductive inhomogeneities. For models investigated which were similar to previously published 3D results calculated by finite difference and integral equation techniques, the solutions are in close agreement.

This study has demonstrated several advantages of the Rayleigh-FFT technique. The Rayleigh-FFT 3D modeling technique has a simple mathematical formulation, is efficient in handling simple 3D problems and has the potential of handling problems of considerable geometric complexity. The Rayleigh-FFT numerical technique requires neither griding nor the numerical differentiation required by other 3D MT modeling techniques. Although all available techniques require large memory allocation and computation time, the structures that can be modeled by the Rayleigh-FFT technique are more complex and thus geologically reasonable. The main limitation is that the Rayleigh-FFT method is an effective computational technique for modeling strutures with gently varying interfaces. The time required for obtaining solutions for a 3D model with maximum interface slope of 18 degrees for one source polarization on a CDC 6600 is about 30 minutes. Inhomogeneities with either large or small resistivity contrasts, buried at shallow or deep depths, and in either homogeneous or layered half-spaces can be modeled. The effect of interface slope on the reliability of the solution and also the effect of an increased aspect ratio on the three dimensionality were investigated.

TABLE OF CONTENTS

	Page
ABSTRACT	iv
LIST OF FIGURES	viii
LIST OF TABLES	xii
ACKNOWLEDGEMENTS	xiii
CHAPTER 1. INTRODUCTION	1
CHAPTER 2. GENERAL THEORY OF MAGNETOTELLURICS	6
2.1. Maxwell's Equations	6
2.2. Previous Models	10
2.3. Solutions to Maxwell's Equations	17
2.4. Boundary Conditions	21
CHAPTER 3. NUMERICAL SOLUTION TO THE INTEGRAL EQUATIONS	25
3.1. Rayleigh-FFT Technique	25
3.2. Reliability of Rayleigh-FFT Technique	30
CHAPTER 4. MAGNETOTELLURIC RESPONSE FOR CONDUCTIVE AND RESISTIVE 3D INHOMOGENEITIES	54
4.1. 3D Models	54
4.2. Model A	55
4.2.1. Field Components for Model A	57
4.2.2. Apparent Resistivities and other Parameters for Model A	62
4.3. Model B	65

4.3.1. Field Components for Model B 65

4.3.2. Apparent Resistivities and other Parameters for Model B 69

CHAPTER 5. INTERPRETATION OF MAGNETOTELLURIC RESPONSES 78

CHAPTER 6. DISCUSSIONS AND CONCLUSIONS 100

APPENDIX A 107

APPENDIX B 111

APPENDIX C 123

APPENDIX D 129

REFERENCES 141

LIST OF FIGURES

Figure		Page
1.	A model for a possible subsurface structure of the Earth.	4
2.	Induced current flow patterns in the region of; a) Conductive inhomogeneity (x-y plane), b) Resistive inhomogeneity (x-y plane), c) Conductive inhomogeneity (x-z plane) d) Resistive inhomogeneity (x-z plane).	12
3.	Spatial plots of the magnitudes and phases of Ex and Hy from Stodt et al., 1981.	15
4.	Spatial plots of the amplitudes of the components of the electric and magnetic field components, from Hibbs and Jones, 1977.	16
5.	A cross-section of the subsurface structure of the earth model used for the application of the boundary conditions.	19
5.	a) TE and TM apparent resistivities and phases obtained from 2D and 3D programs. b) Cross-section of 2D model used.	31
7.	a) Topography of non-planar interface. b) Derivative of the interface along x-axis, c) Derivative of the interface along y-axis.	35
8.	Normalized residuals at the non-planar interface of the x-component of the electric field for scattering orders of a) 9, b) 11 and c) 13.	36
9.	Normalized residuals at the non-planar interface of the y-component of the mgnetic field for scattering orders of a) 9, b) 11 and c) 13.	37
10.	Amplitudes of the magnetic field components for the model in Figure 7, a) Hx, b) Hy and c) Hz.	38
11.	Amplitudes of the electric field components	

for the model in Figure 7, a) Ex, b) Ey and c) Ez. 39

12. Profiles of the amplitudes of Ex and Hy the x-axis for scattering orders of a) 9, b) 11 and c) 13. 41

13. Profiles of the amplitudes of Ex and Hy along the y-axis for scattering orders of a) 9, b) 11 and c) 13. 42

14. Total scattering orders versus CPU times for matrix inversion and .FFT and matrix size. 44

15. a) Topography of the non-planar interface.
b) Derivative of the interface along x-axis.
c) Derivative of the interface along y-axis. 45

16. Maximum interface slope versus percentage RMS errors for Ex and Hy. 48

17. Normalized residuals for the x-component of the electric field (NREx) and y-component of the magnetic field (NRHy) at the non-planar interface for different values of maximum interface slopes.
a) NREx with maximum slope of 8 degrees.
b) NRHy with maximum slope of 8 degrees.
c) NREx with maximum slope of 18 degrees.
d) NRHy with maximum slope of 18 degrees.
e) NREx with maximum slope of 27 degrees.
f) NRHy with maximum slope of 27 degrees.
g) NREx with maximum slope of 42 degrees.
h) NRHy with maximum slope of 42 degrees. 49

18. Total number of scattering orders versus percentage RMS errors for inhomogeneities of resistivities of 5 and 10 Ohm-m and slopes of 15 and 28 degrees in 100 Ohm-m half-space. 52

19. A cross-section of the subsurface model (x-z plane), used for forming 3D inhomogeneity. 56

20. a) Topography of the non-planar interface for model A
b) A cross-section of the model along x-axis. 58

21. Amplitudes of the magnetic field components for model A. 59

22. Amplitudes of the electric field components for model A. 60

23. Profiles of the amplitudes of the x-component of the electric field and y-component of the magnetic field through the center of the inhomogeneity along a) x-axis anb b) y-axis. 61

24. Apparent resistivities for model A. 64

25. a) Skew, b) Tipper magnitude and c) Tipper azimuth in the 4th quadrant for model A. 66

26. a) Skew, b) Tipper magnitude and c) Tipper azimuth from Ting and Hohmann, 1981. 67

27. a) Topography of the non-planar interface for model B. b) A cross-section of the model along x-axis. 68

28. Amplitudes of the magnetic field components for model B. 70

29. Amplitudes of the electric field components for model B. 71

30. Profiles of the amplitudes and phase angles of the x-component of the electric field and y-component of the magnetic field along the y-axis through the center of the inhomogeneity. 72

31. Amplitudes of Ex, Hy, Hz, Hz Hy and a profiles with normalized phases through the center of the inhomogeneity, from Hibbs and Jones, 1977. 73

32. a) Phase angle of the z-component of the electric field along x-axis. b) Phase angle of the z-component of the magnetic field along y-axis. 74

33. Apparent resistivities for model B. 76

34. a) Skew, b) Tipper magnitude, and c) Tipper azimuth in the 4th quadrant for model B. 77

35. Apparent resistivities for a 5 Ohm-m inhomogeneity buried at a 2Km depth in a 100 Ohm-m half-space. ρ_{xx} at a) 10, b) 1.0, c) 0.1 and d) 0.01 Hz.

ρxy at e) 10, f) 1.0, g) 0.1 and d) 0.01 Hz. 80

36. Skew and Tipper magnitudes for a 5 Ohm-m inhomogeneity buried 2 Km in 100 Ohm-m half-space.
Skew at a) 10., b) 1.0, c) 0.1 and d) 0.01 Hz.
Tipper at a) 10., b) 1., c) .1 and d) 0.01 Hz. 81

37. a) Topography for 'flat' magma.
b) Topography of dome shaped magma. 83

38. ρxx for magma 1 at a) 0.01 and b) 0.001 Hz.
ρxy for magma 1 at c) 0.01 and d) 0.001 Hz.
Skew for magma 1 at e) 0.01 and f) 0.001 Hz.
Tipper for magma 1 at g) .01 and h) .001 Hz. 85

39. ρxx for magma2 at a) 0.01 and b) 0.001 Hz.
ρxx for magma 3 at c) 0.01 and d) 0.001 Hz.
ρxy for magma 2 at e) 0.01 and f) 0.001 Hz.
ρxy for magma 3 at g) 0.01 and h) 0.001 Hz. 87

40. Skew for magma 2 at a) 0.01 and b) 0.001 Hz.
Skew for magma 3 at c) 0.01 and d) 0.001 Hz.
Tipper for magma 2 at e) .01 and f) .001 Hz.
Tipper for magma 3 at g) .01 and h) .001 Hz. 88

41. a) ρxx, b) ρxy, c) Tipper and d) Skew for magma 4 at 0.001 Hz. 89

42. Apparent resistivity (ρxx) for models D and E. 93

43. Apparent resistivity (ρyy) for models D and E. 94

44. Apparent resistivity (ρxy) for models D and E. 95

45. Apparent resistivity (ρyx) for models D and E. 96

46. Tipper magnitudes for models D and E. 97

47. Tipper azimuth for models D and E. 98

LIST OF TABLES

Table		Page
1.	The relationship between the total number of scattering orders and computation time.	43
2.	The relationship between interface slope and percentage root mean square error.	47

ACKNOWLEDGEMENTS

I would like to express my appreciation to Drs. Wayne J. Peeples, Ian Duncan, Roger J. Phillips and David D. Blackwell for the contributions they made towards the success of this project in terms of discussions, criticisms and suggestions.

To Dr. John Ferguson, Dr. John Steel, Mohammed Ghassem-Al-Askari, Rotimi Aderohummu, Dr. R. Helgason, Patrick Shore, Cary Caruso, Shari and Richard Kelley and others with whom I discussed certain aspects of this research, I express many thanks. I am grateful to Cindy Gwinn and Deborah Ledbedder for typing the equations in the Appendices.

This research was undertaken while the author was on Niger State Government of Nigeria's scholarship and a Study Fellowship from Ahmadu Bello University Zaria, Nigeria.

This research was partially funded by USGS Grant No. 5-27506 and ISEM, SMU. Most of the computations were done at the Bradfield Computer Centre SMU.

The first step towards more realistic interpretation techniques was the extension of Cagniard's one dimensional model to two dimensions. A one dimensional model (1D) has the electrical characteristics varying in one direction, a two dimensional model (2D) varies in two perpendicular directions, and a three dimensional (3D) model varies in three directions. Rankin (1962) and d'Erceville and Kunetz (1962) analytically solved the 2D dike and vertical contact problems. For the general two dimensional problem, Maxwell's equations must be approximated by numerical methods. Typical approaches have been: finite difference (Neves, 1957), transmission surface analogy (Swift, 1967) and finite element techniques (Silvester and Haslam, 1972). Some of the two dimensional models considered include a one dimensionally varying subsurface interface (Mann, 1964; Jiracek, 1973; and Peeples, 1983).

In the mid to late 1970's, investigations of three dimensional inhomogeneities were initiated. Three dimensional modeling has been done for both MT and electromagnetic induction. Most of the models used so far have a zone of inhomogeneity in an otherwise isotropic and homogeneous half-space. This zone is usually in a form of one or more homogeneous and isotropic parallelipipeds with a different conductivity to that of the half-space. The numerical schemes that have been used for solving 3D problems for MT and electromagnetic induction include: integral equations (Hohmann, 1975; Weidelt, 1975; Meyer,

1977; Ting and Hohmann, 1981), finite element technique (Reddy et al., 1977; Pridmore, 1978), finite difference methods (Lines and Jones, 1973; Hibbs and Jones, 1978), and a hybrid method combining finite element technique with integral equations (Lee et al., 1981). The main problems associated with these models and numerical schemes are: (1) the models may be inadequate in representing the subsurface geology, (2) the number of the equations to be solved is very large so that the computer cost can be prohibitive, and (3) numerical differentiation of the solution, which is necessary to compute the full set of fields, is not always reliable (Lee et al., 1981).

In this work, the magnetotelluric response for a two dimensionally varying subsurface interface separating homogeneous, linear and isotropic regions will be investigated (Figure 1). Aki and Larner (1970) solved the wave equation for a one dimensionally varying subsurface interface. They applied the Rayleigh hypothesis of a periodic surface to the seismic scattering problem. Aki and Larner (1970) took advantage of the Fast Fourier Transform (FFT) in simplifying the computation of the spectral amplitudes in wavenumber domain. The same technique was used by Bard and Bouchon (1980a,b) to study the seismic response of sediment filled valleys. Jiracek (1973) applied the technique to obtain the relations for the fields for 2D varying interfaces and computed the MT response for one dimensionally varying interfaces at high frequencies.

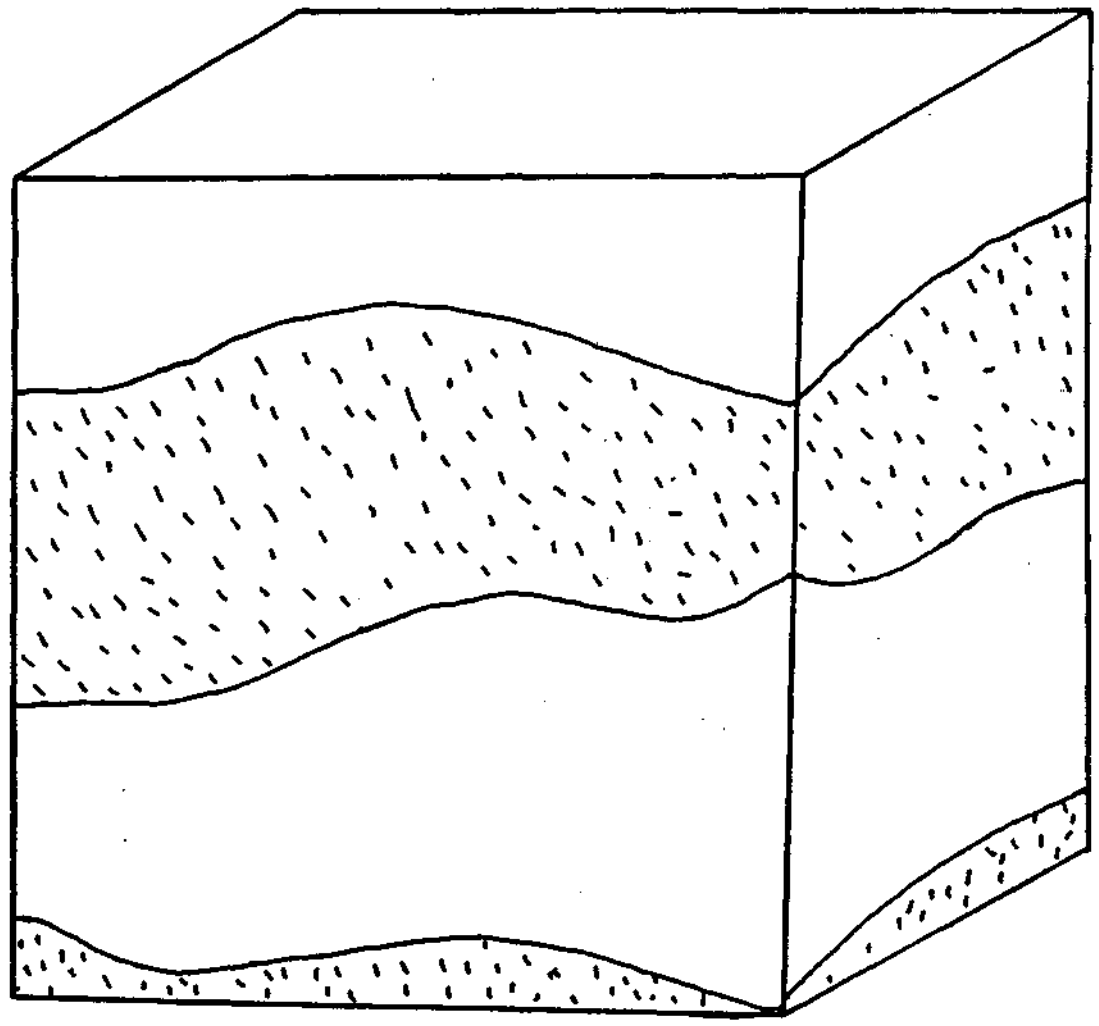


Figure 1. A model for a possible subsurface structure of the Earth.

Recently, Peeples (1983) investigated the MT response from one dimensionally varying subsurface interfaces and presented an analysis for both the forward and the inverse problems.

In this work, Maxwell´s equations in three dimensions for a two dimensionally varying subsurface interfaces will be solved using the spectral method (following Aki and Larner, 1970). Although equivalent solutions for a 2D varying interface were derived previously by Jiracek (1973) a numerical solution was only presented for 1D varying interfaces. This study presents both a rederivation of the equations for 2D varying interface and an extension of Aki and Larner (1970) approach to produce a numerical scheme for solving this more complex class of problems. The fields, impedances, apparent resistivities, and dimensionality parameters, such as skew and tipper will be investigated for a series of models previously studied by other techniques. Also responses for different frequencies from possible magma chambers of different shapes and resistivity contrast will be invetigated.

CHAPTER 2

GENERAL THEORY OF MAGNETOTELLURICS

Plane electromagnetic waves with an $e^{i\omega t}$ time dependence are assumed to be normally incident on the surface of the earth. The subsurface structure of a possible earth model is shown in Figure (1). It consists of different electrically homogeneous and isotropic regions with conductivity σ_i separated by subsurface interfaces where depths are described by $Z = f(x,y)$. The permittivity and magnetic permeability are assumed to be their free space value everywhere.

2.1 Maxwell's Equations.

Maxwell's equations and the constitutive relations for an electrically linear, isotropic and homogeneous medium are given by

$$\nabla \times \vec{E} = -\frac{\partial \vec{B}}{\partial t} \qquad 1.$$

$$\nabla \times \vec{H} = \vec{J} + \frac{\partial \vec{D}}{\partial t} \qquad 2.$$

$$\vec{D} = \epsilon \vec{E} \qquad 3.$$

$$\vec{B} = \mu \vec{H} \qquad 4.$$

$$\vec{J} = \sigma \vec{E} \qquad 5.$$

where $\vec{E}$ is the electric field intensity,

$\vec{B}$ is the magnetic induction,

$\vec{H}$ is the magnetic field intensity,

$\vec{D}$ is the dielectric displacement,

$\vec{J}$ is the current density,

t is the time,

σ is the conductivity,

ω is the angular frequency,

μ is the magnetic permeability of free space,

ϵ is the permittivity of free space and

$i = \sqrt{-1}$.

For plane waves with an $e^{i\omega t}$ time dependence, substituting equations (3) and (5) into (2) and (4) into (1),

$$\nabla \times \vec{E} = -i\mu\omega\vec{H} = -\hat{Z}\vec{H} \qquad 6a.$$

$$\nabla \times \vec{H} = (\sigma + i\omega\epsilon)\vec{E} = \hat{Y}\vec{E} \qquad 6b.$$

where $\hat{Z} = i\mu\omega$ and $\hat{Y} = \sigma + i\omega\epsilon$

Take curl of equations (6a) and (6b),

$$\nabla \times (\nabla \times \vec{E}) = -\hat{Z}\nabla \times \vec{H} = -\hat{Z}\hat{Y}\vec{E} \qquad 7.$$

$$\nabla \times (\nabla \times \vec{H}) = \hat{Y}\nabla \times \vec{E} = -\hat{Z}\hat{Y}\vec{H} \qquad 8.$$

Let $\vec{R}$ represent either $\vec{E}$ or $\vec{H}$,

$$\nabla \times (\nabla \times \vec{R}) = -\hat{Z}\hat{Y}\vec{R} \qquad 9.$$

$$\text{but } \nabla \times (\nabla \times \vec{R}) = \nabla (\nabla \cdot \vec{R}) - \nabla^2 \vec{R} \qquad 10.$$

Rewriting equation (9) in Cartesian coordinates and using equation (10);

$$\frac{\partial^2 Rx}{\partial y^2} + \frac{\partial^2 Rx}{\partial z^2} - \frac{\partial}{\partial x}\left(\frac{\partial Ry}{\partial y} + \frac{\partial Rz}{\partial z}\right) = \hat{Z}\hat{Y}Rx$$

$$\frac{\partial^2 Ry}{\partial x^2} + \frac{\partial^2 Ry}{\partial z^2} - \frac{\partial}{\partial y}\left(\frac{\partial Rx}{\partial y} + \frac{\partial Rz}{\partial z}\right) = \hat{Z}\hat{Y}Ry \qquad 11.$$

$$\frac{\partial^2 Rz}{\partial x^2} + \frac{\partial^2 Rz}{\partial y^2} - \frac{\partial}{\partial z}\left(\frac{\partial Rx}{\partial x} + \frac{\partial Ry}{\partial y}\right) = \hat{Z}\hat{Y}Rz$$

The solution to the above system of partial differential equations gives the electromagnetic field components. The models described in this study are in Cartesian coordinates, z is the vertical axis and the x and y axes are in the two perpendicular horizontal directions. In the case of a one-dimensional model, it is assumed that the induced current distribution in the model structure

exhibits only z-dependence. In this case equations (11) reduce to;

$$\frac{\partial^2 Rx}{\partial z^2} = \hat{z}\hat{y}R_x$$

The above equation can easily be solved analytically for 1D models (Ward et al., 1973).

For a 2D model, if the induced current distribution is assumed to be x- and z-dependent, equations (11) result in;

$$\frac{\partial^2 Rx}{\partial z^2} - \frac{\partial}{\partial x}\frac{\partial Rz}{\partial z} = \hat{z}\hat{y}Rx$$

$$\frac{\partial^2 Ry}{\partial x^2} + \frac{\partial^2 Ry}{\partial z^2} = \hat{z}\hat{y}Ry$$

$$\frac{\partial^2 Rz}{\partial x^2} - \frac{\partial}{\partial z}\frac{\partial Rx}{\partial x} = \hat{z}\hat{y}Rz$$

These system of equations (for the 2D model) and equations (11) (for 3D model) are difficult to solve analytically. Some specific 2D models have been solved exactly, for example, the dike problem of Rankin (1962) and the vertical contact problem of d'Erceville and Kunetz (1962). More general 2D and 3D models require numerical solutions. Such techniques for solving 2D models are discussed in detail by Ward et al. (1973). They include; transmission surface analogy, finite element, finite

difference and integral equations techniques.

Various numerical techniques have been used in solving Maxwell's equations for 3D inhomogeneities. In all the techniques previously considered, the zone under investigation is divided into cells and equations (11) are written in finite difference form (Lines and Jones, 1973a and b; Hibbs and Jones, 1977; Jones and Vozoff, 1978 etc), finite element form (Reddy et al., 1977), or in integral equation form (Ting and Hohmann, 1981; Stodt et al., 1981).

All numerical techniques for solving Maxwell's equations for 3D models have the disadvantage of requiring the inversion of large matrices, due to large number of grid points needed. Thus the solutions require very large computer time and memory allocation. These requirements limit the tractable models to some form of parallelipipeds or other simple shapes. There is also the problem of crude approximations at the boundary (Reddy et al.,1977).

2.2 Previous Models.

Magnetic and electric field components can be theoretically determined at the models' upper surface by choosing a model and either analytically or numerically calculating the fields. In the case of 3D earth, the models considered have been a parallelipiped or a combination of parallelipipeds in an otherwise homogeneous

half-space with plane electromagnetic waves incident at the surface. These models are of two kinds: resistive block in a conductive medium (Hibbs and Jones, 1977); island structure; and a conductive body in a resistive half-space (Reddy et al., 1977; Ting and Hohmann, 1981, and Stodt et al., 1981). Hibbs and Jones used a finite difference numerical technique to determine the fields whereas Stodt et al. (1981) and Ting and Hohmann (1981) used an integral equation approach.

One of the models considered by Stodt et al. (1981) is a buried parallelipiped 0.25Km below the earth's surface and with dimensions 1 by 2 by 1 Km. The inhomogeneity has a resistivity of 5 Ohm-m and that of the half-space is 100 Ohm-m. They obtained fields and phases at frequencies of 0.1, 1 and 10Hz. Hibbs and Jones (1981) considered 6 by 6 Km island block in sea water of resistivity 0.25 Ohm-m. The height of the block is 4 Km and its resistivity and that of the half-space is 1000 Ohm-m. They assumed plane electromagnetic waves with the magnetic field component polarized in the y direction and of frequency 0.001Hz normally incident at the sea-island surface.

In order to understand the behaviour of the fields observed near the inhomogeneities, let us consider the induced current flow. Figures 2a-d show the current patterns near both a resistive and a conductive inhomogeneity in x-y and x-z planes. From Figure 2c, it can be

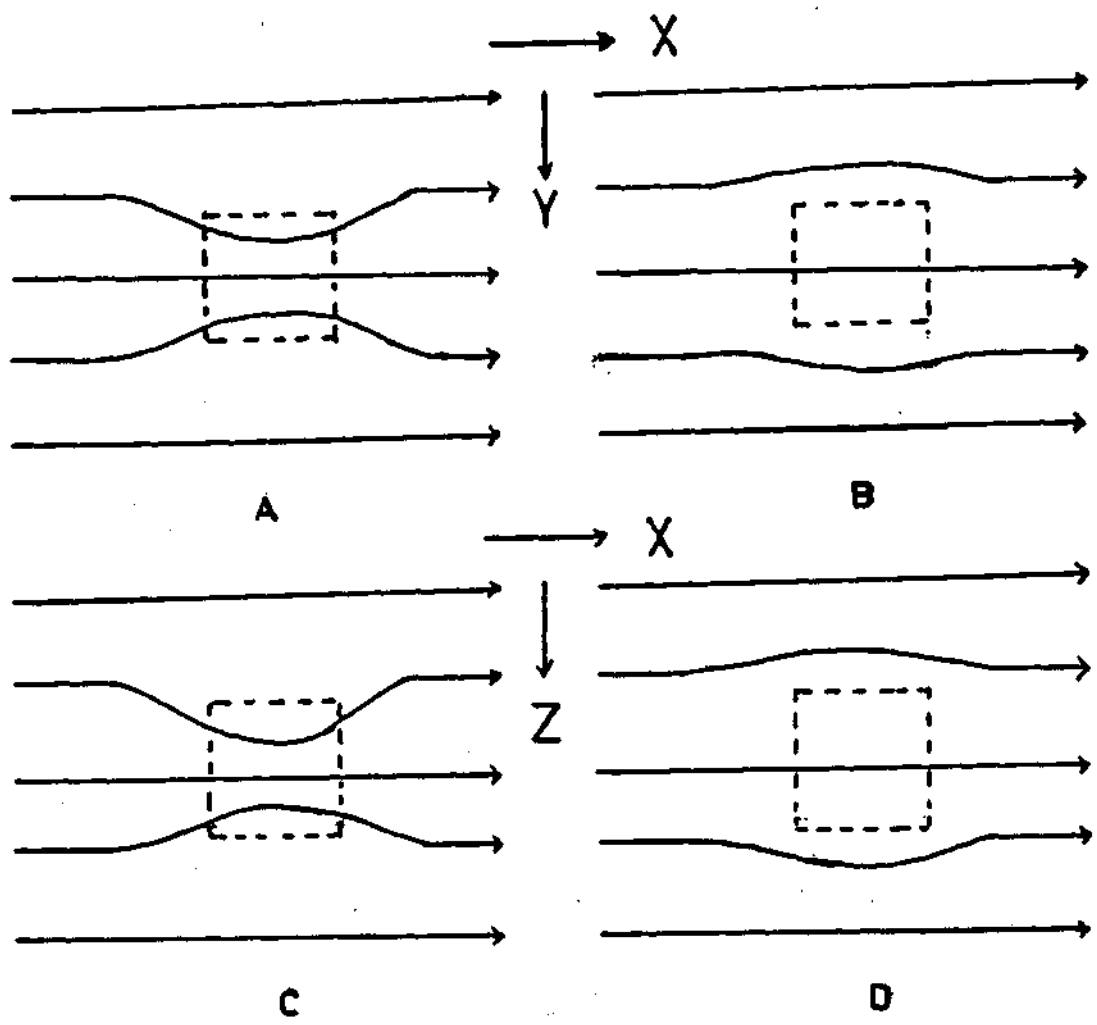


Figure 2. Induced current flow patterns in the region of
a) Conductive inhomogeneity (x-y plane),
b) Resistive inhomogeneity (x-y plane),
c) Conductive inhomogeneity (x-z plane) and
d) Resistive inhomogeneity (x-z plane).

seen that the x-component of the currents near the surface in the zone of the conductor decreases in magnitude and it increases for a resistive case (Figure 2d) as compared to the half-space. So the x-component of the electric field should have lower values just above a conductive inhomogeneity and higher values above a resistive one (Figures 3 and 4). Further away from the inhomogeneity, they are deflected either away from or into the body. The deflection is a maximum diagonally off the corners. The magnitudes of the y-components of the electric field are therefore at their maximum off the corners of the inhomogeneities (Figure 4). At the center of the bodies, the current passes straight through, so there is no y-component of the electric field along the axis of symmetry parallel to the current flow. In the case of the z-component of electric field, the maximum values occur off the edges of the inhomogeneity perpendicular to the direction of current flow where the z-component of the current is maximum (Figure 2c,d and 4). Here the magnitude of the z-component of the electric field is zero along the axis of symmetry perpendicular to the current flow.

The magnitudes of the magnetic field components can easily be understood from those of the electric field components by applying Maxwell's equations (6a). The magnetic field components are given by;

$$Hx = \frac{-1}{i\mu\omega}\left(\frac{\partial Ez}{\partial y} - \frac{\partial Ey}{\partial z}\right)$$

$$Hy = \frac{-1}{i\mu\omega}\left(\frac{\partial Ex}{\partial z} - \frac{\partial Ez}{\partial x}\right)$$

$$Hz = \frac{-1}{i\mu\omega}\left(\frac{\partial Ey}{\partial x} - \frac{\partial Ex}{\partial y}\right)$$

Figure 3 is a spatial plot of the x-component of the electric field and the y-component of the magnetic field (magnitude and phase) for a conductive inhomogeneity from Stodt et al. (1981), and Figure 4 is the amplitude plot for all the components of the magnetic and electric fields for the island model discussed by Hibbs and Jones (1977).

From the above analysis, the field patterns for the resistive and conductive 3D inhomogeneities are the same for y and z components of the electric field and x and z components of the magnetic field for Hy or Ex polarization. In the case of a conductive inhomogeneity, the magnitudes of the x-component of the electric field are lower in the vicinity of the inhomogeneity and higher for a resistive case as compared to the half-space values. The reverse is true for the y-component of the magnetic field (for Hy or Ex polarization). These field patterns are peculiar to 3D type inhomogeneities. In the case of 1D model and parallel to the strike for a 2D model, there is no change in the field values. These features of the magnitudes of the fields will help in understanding the patterns of the apparent resistivities to be discussed later.

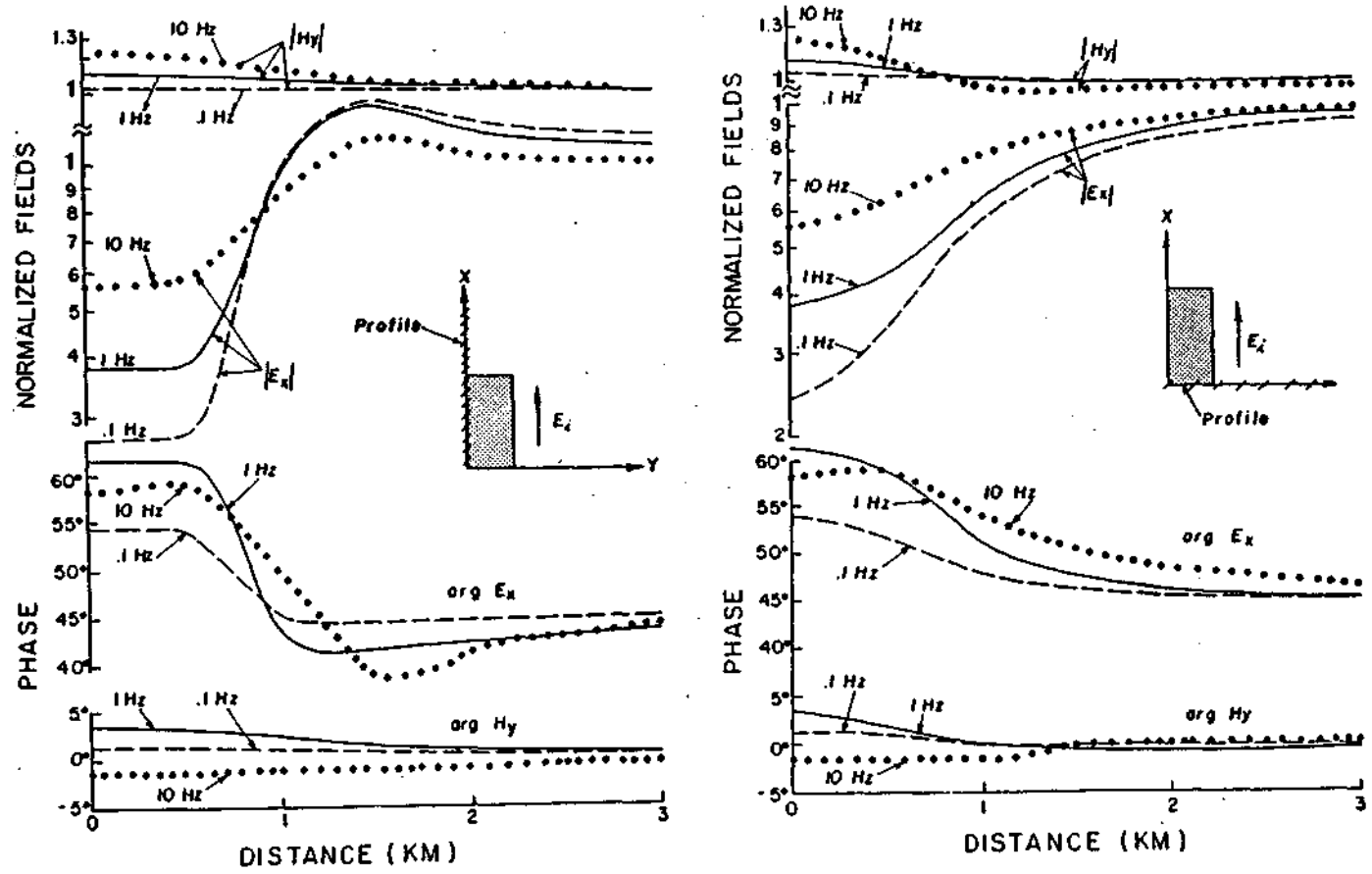


Figure 3. Spatial plots of the magnitudes and phases of Ex and Hy, from Stodt et al., 1981.

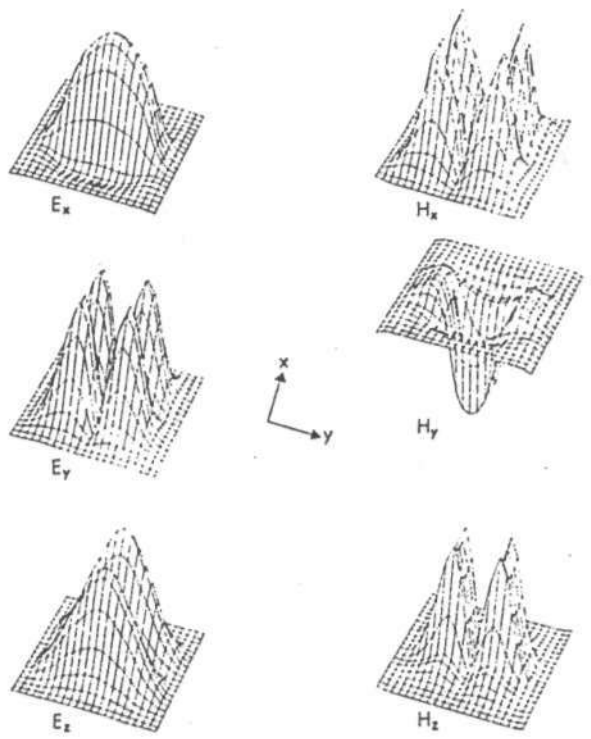


Figure 4. Spatial plots of the amplitudes of the components of the electric and magnetic field components, from Hibbs and Jones, 1977.

2.3 Solutions to Maxwell's Equations.

Solutions to the system of partial differential equations (11) are obtained by Fourier transform analysis (Appendix A). The results are as follows;

$$R_{\mu x}(x,y,z) = \frac{1}{4\pi^2}\iint_{-\infty}^{\infty}\left\{A_\lambda(\xi,\eta)\exp(z\alpha_\lambda) + B_\lambda(\xi,\eta)\exp(-z\alpha_\lambda)\right\}x \exp(i\xi x + i\eta y)d\xi\, d\eta$$

$$R_{\mu y}(x,y,z) = \frac{1}{4\pi^2}\iint_{-\infty}^{\infty}\left\{C_\lambda(\xi,\eta)\exp(z\alpha_\lambda) + D_\lambda(\xi,\eta)\exp(-z\alpha_\lambda)\right\}x \exp(i\xi x + i\eta y)d\xi\, d\eta$$

$$R_{\mu z}(x,y,z) = \frac{-i\omega}{4\pi^2}\iint_{-\infty}^{\infty}\frac{1}{\alpha_\lambda}\left\{P_\lambda(\xi,\eta)\exp(z\alpha_\lambda) - Q_\lambda(\xi,\eta)\exp(-z\alpha_\lambda)\right\}x \exp(i\xi x + i\eta y)d\xi\, d\eta \quad (12)$$

where:

$R_{\mu x}(x,y,z)$ represents either the magnetic or electric field component along the x direction in the region λ which can be computed for any coordinate position (x,y,z),

α_λ is the propagation constant; Al,Bl, etc are the spectral amplitudes and where ξ and η are the wave numbers in the x and y directions respectively.

Equation (12) provides the solution to Maxwell's equations in three dimensions for an isotropic and homogeneous medium. The fields are a function of the position

and the electric characteristics of the medium. Careful examination of the equations reveals that the fields are represented by the superposition of plane waves of different wave numbers. If the surface on which the waves are incident is non-planar, then the problem will be very similar to Rayleigh's acoustic wave scattering problem (Rayleigh,1896). His basic assumption is that all scattered fields from a rough surface could be expressed as a superposition of outgoing radiating and nonradiating plane waves (Jiracek, 1973).

The above equations are in a generalized form, and could be written for magnetic field components for different regions l for the configuration shown in Figure (5). The magnetic field component of a normally incident plane wave is assumed polarized along the y-axis and of unit amplitude. The surface of the earth model is considered flat, the first subsurface interface varies in two dimensions and the second interface is planar. All regions are isotropic and homogeneous. The air layer has a zero conductivity and the other three layers have conductivities σ_1, σ_2, and σ_3 respectively. The permittivity and the permeability of all the regions are considered to be those of free space.

The magnetic and the electric field components for the different regions for the configuration shown in Figure (5) are given in Appendix A.

The x component of the magnetic field in a region 1 is:

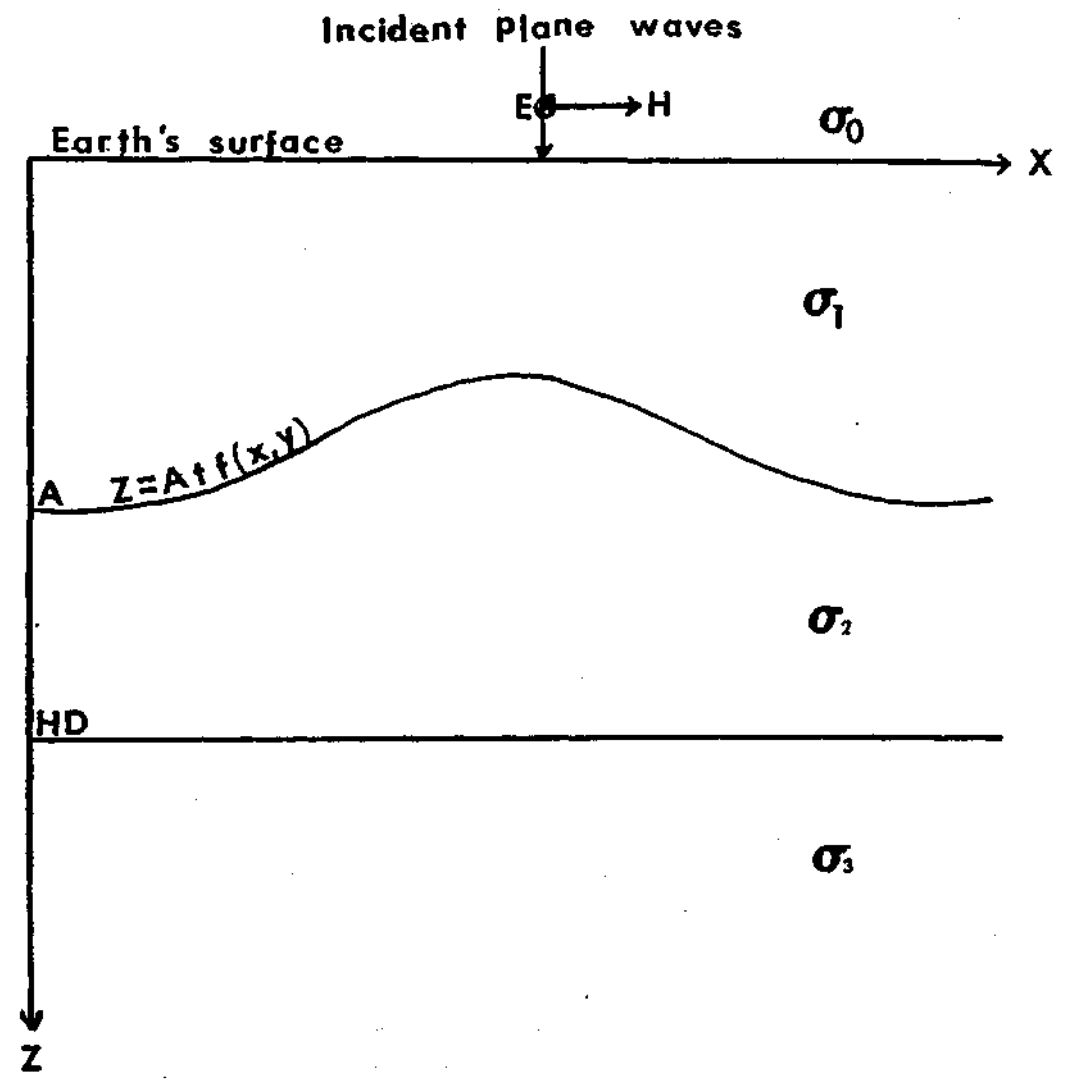


Figure 5. A cross-section of the subsurface structure of the earth model used for the application of the boundary conditions.

$$H_{\ell x}(x,y,z) = \frac{1}{4\pi^2}\int_{-\infty}^{\infty}\int\left\{A_\ell(\xi,\eta)\exp(z\alpha_\ell) + B_\ell(\xi,\eta)\exp(-z\alpha_\ell)\right\}x$$
$$\exp(i\,\xi\,x + i\,\eta\,y)\,d\xi\,d\eta$$

Using Ampere's law (equation 2), similar relations for the electric field components could be derived.

From equation (6b),

$$\nabla \times \vec{H} = (\sigma + i\omega\epsilon)\vec{E} = \hat{Y}\vec{E} = \hat{Y}(Ex\hat{i} + Ey\hat{j} + Ez\hat{k})$$

Assuming that the conductivities of the subsurface layers,

$|\sigma_\ell| \gg |i\,\omega\epsilon_o|$

For air,

$$E0x = \frac{1}{i\omega\epsilon_o}\left(\frac{\partial H0z}{\partial y} - \frac{\partial H0y}{\partial z}\right)$$

$$E0y = \frac{1}{i\omega\epsilon_o}\left(\frac{\partial H0x}{\partial z} - \frac{\partial H0z}{\partial x}\right) \qquad 14.$$

$$E0z = \frac{1}{i\omega\epsilon_o}\left(\frac{\partial H0y}{\partial x} - \frac{\partial H0x}{\partial y}\right)$$

For the subsurface regions;

$$Ejx = \frac{1}{\sigma_j}\left(\frac{\partial Hjz}{\partial y} - \frac{\partial Hjy}{\partial z}\right)$$

$$Ejy = \frac{1}{\sigma_j}\left(\frac{\partial Hjx}{\partial z} - \frac{\partial Hjz}{\partial x}\right) \qquad 15.$$

$$Ejz = \frac{1}{\sigma_j}\left(\frac{\partial Hjy}{\partial x} - \frac{\partial Hjx}{\partial y}\right)$$

for j=1,2,3.

From the above relations, the electric field components in the different regions of the model in Figure (5) are derived and stated in Appendix A. The x component of the electric field in a region 1 is given by;

$$E_{lx}(x,y,z) = \frac{1}{4\pi^2\sigma_l}\int_{-\infty}^{\infty}\int_{-\infty}^{\infty}\left\{\frac{1}{\alpha_l}\left[P_l(\xi,\eta)\exp(z\alpha_l) - Q(\xi,\eta)\exp(-z\alpha_l)\right]\right.$$
$$\left. -\alpha_l\left[C_l(\xi,\eta)\exp(z\alpha_l) - D(\xi,\eta)\exp(-z\alpha_l)\right]\right\}\chi$$
$$\exp(i\,\xi\,x + i\,\eta\,y)\,d\xi\,d\eta$$

The only unknowns in the above equations are the spectral coefficients, Ai's etc. In order to determine these spectral coefficients, the boundary conditions are applied.

2.4 Boundary Conditions.

For the magnetic fields, the condition that has to be satisfied at the boundary between two media of finite conductivity is;

$$\hat{n}X(\vec{H1} - \vec{H2}) = 0 \qquad 17.$$

and for the electric fields it is;

$$\hat{n} \times (\vec{E}1 - \vec{E}2) = 0 \qquad 18.$$

where $\vec{H}1$ and $\vec{H}2$ are the magnetic fields in adjacent regions 1 and 2 and $\vec{E}1$ and $\vec{E}2$ are the corresponding electric fields (Stratton, 1941).

The unit normal vector to the non-planar interface, n, is given by;

$$\hat{n} = -\frac{\nabla f(x,y)}{|\nabla f(x,y)|} = nx\hat{i} + ny\hat{j} + nz\hat{k}$$

where

$$nx = -\frac{\partial f}{\partial x}(x,y)\, nz$$

$$ny = -\frac{\partial f}{\partial y}(x,y)\, nz \qquad 19.$$

$$nz = \left\{ \left(\frac{\partial f}{\partial x}(x,y)\right)^2 + \frac{\partial f}{\partial y}(x,y) + 1 \right\}^{-1/2}$$

where f(x,y) describes the surface of the non-planar interface.

As shown in Figure 5, the earth-air interface and the second subsurface interface are planar, and the first subsurface interface is non-planar. This feature will be maintained in all the models examined. If the depth to the

second subsurface interface is HD, applying equations (17) and (18) at the two flat boundaries;

At Z = 0,

$$H0x = H1x$$
$$H0y = H1y$$
$$E0x = E1x \qquad (20.)$$
$$E0y = E1y$$

At Z = HD,

$$H2x(x,y,HD) = H3x(x,y,HD)$$
$$H2y(x,y,HD) = H3y(x,y,HD)$$
$$E2x(x,y,HD) = E3x(x,y,HD) \qquad (21.)$$
$$E2y(x,y,HD) = E3y(x,y,HD)$$

Applying the boundary conditions at the irregular subsurface interface, the x and y components of equations (17) and (18) are;

$$ny.H1z - nz.H1y = ny.H2z - nz.H2y$$
$$nz.H1x - nx.H1z = nz.H2x - nx.H2z$$
$$ny.E1z - nz.E1y = ny.E2z - nz.E2y$$
$$nz.E1x - nx.E1z = nz.E2x - nx.E2z$$

The third component of the boundary condition is a linear combination of the above two components.

Let $\gamma_x = -\frac{\partial f(x,y)}{\partial x}$ and $\gamma_y = -\frac{\partial f(x,y)}{\partial y}$, and rewriting the above equations,

$$\gamma_y H1z - H1y = \gamma_y H2z - H2y$$
$$H1x - \gamma_x H1z = H2x - \gamma_x H2z$$
$$\gamma_y E1z - E1y = \gamma_y E2z - E2y \qquad 22.$$
$$E1x - \gamma_x E1z = E2x - \gamma_x E2z.$$

The above boundary conditions (equations 20 through 22), are applied to equations (A13a) through (A20c) in Appendix A (for a detailed discussion of the application of the boundary conditions see Appendix B). From the solutions thus obtained, the spectral coefficients can be computed. The unknown coefficients A0, C0, A1, B1, C1, D1, A2, B2, C2, D2, B3 and D3 can be obtained by simultaneous solution of equations B2a-d, B4a-d, and B6a-d. Equations B2a-d and B6a-d were solved directly for the spectral amplitudes in terms of B1, B2, D1 and D2 and the values for the other coefficients were substituted into equations B4a-d, resulting in equations B7a to B7d. The solution to these equations, B7a through B7d, will be discussed in the following chapter.

CHAPTER 3

NUMERICAL SOLUTION TO THE INTEGRAL EQUATIONS

3.1 Rayleigh-FFT Technique.

The numerical solution described here is an extension of the Rayleigh-FFT technique developed by Aki and Larner (1970) and Jiracek (1973).

The spectral amplitudes can be obtained by solving equations B7a-d as described below. The model shown in Figure (5) has a flat earth-air interface and also a flat second subsurface interface. Some of the spectral amplitudes can be obtained directly by Fourier transform methods of the equations (Appendix B). The equations that involve the curved interface cannot be solved directly as the interface is irregular. To solve these equations, it is assumed that the zone containing the non-planar interface is periodic, with periods of Lx and Ly along x and y axes respectively.

If $Z = f(x,y)$ defines the non-planar interface, then

$$f(x,y) = f(x+mLx, y+nLy)$$

$$m,n = 0, \pm 1, \pm 2, \pm 3, \pm \ldots\ldots$$

From the periodicity assumption,

$$\exp(i\xi x + i\eta y) = \exp\left\{i\xi (x + Lx) + i\eta (y + Ly)\right\}$$

and therefore,

$$\xi Lx = 2\pi m \qquad m=0,\pm1,\pm2,\pm3,\pm\cdots\cdots$$

$$\eta Ly = 2\pi n \qquad n = 0,\pm1,\pm2,\pm3,\pm\cdots\cdots$$

The above definitions of ξ and η imply that the scattered plane waves form a discrete rather than continuous spectrum. The scattered directions θ^s_x (m) (along x-axis), are given by;

$$k_\mu \sin\theta^s_x(m) = 2\pi m / Lx$$

where $k_\mu = \sqrt{\mu\alpha\pi}$

and μ is the index for a given region.

Thus the periodicity assumption converts infinite integrals in equations B7a-B7d to infinite summations. The infinite summations can be truncated (an approximation) to yield;

$$\sum_{-M}^{M}\sum_{-N}^{N}(g1B1 + g2D1 + g3B2 + g4D2) = \sum_{-M}^{M}\sum_{-N}^{N} h1 \qquad 24.$$

$$\sum_{-M}^{M}\sum_{-N}^{N}(g5B1 + g6D1 + g7B2 + g8D2) = \sum_{-M}^{M}\sum_{-N}^{N} h2 \qquad 25.$$

$$\sum_{-M}^{M}\sum_{-N}^{N}(g9B1 + g10D1 + g11B2 + g12D2) = \sum_{-M}^{M}\sum_{-N}^{N}h3 \qquad 26.$$

$$\sum_{-M}^{M}\sum_{N}^{N}(g13B1 + g14D1 + g15B2 + g16D2) = \sum_{-M}^{M}\sum_{-N}^{N}h4 \qquad 27.$$

where g1 through g16 and h1 to h4 are given in Appendix B.

The solution to the above system of equations will result in the spectral amplitudes, B1, B2, D1 and D2. Rather than solving the system of equations in their present form, both sides of the equation along x and y axes can be Fourier transformed (i.e. the Fourier transform of g1-g16 and h1-h4 along x and y axes for each value of ξ and η can be taken).

Thus, $\mathcal{F}\{g1(x,y,\xi,\eta)\} = G1(k_x,k_y,\xi,\eta)$.

where $\mathcal{F}$ denotes Fourier transform operator.

Aki (personal communication quoted in Jiracek, 1973) noted that the system of equations are better behaved in the wavenumber domain. The resulting matrices Gi which are now in the wavenumber domain are truncated to 2M+1 by 2N+1. The values of M and N are chosen such that the resulting matrices are square. The choice of M and N is governed by the type of problem being solved. From equation (23), there is a maximum value of m, (M), for a given repetition distance, Lx, frequency of the waves and the conductivity of a medium for which there are scattering angles up to and

including 90 degrees. M is chosen such that all the radiating modes are included in the solution (this includes all the modes with scattering angles less than 90 degrees and a few with complex angles). The nature of these matrices were investigated. M was chosen when the amplitudes of the entries have dropped to less than one percent of the maximum value.

The Fourier transformed functions $\underline{\underline{G}}i$, can be arranged in a matrix form as shown;

$$\begin{bmatrix} G1 & G2 & G3 & G4 \\ G5 & G6 & G7 & G8 \\ G9 & G10 & G11 & G12 \\ G13 & G14 & G15 & G16 \end{bmatrix} \begin{bmatrix} B1 \\ D1 \\ B2 \\ D2 \end{bmatrix} = \begin{bmatrix} H1 \\ H2 \\ H3 \\ H4 \end{bmatrix}$$

or $\underline{\underline{G}}\underline{A} = \underline{H}$ 28.

The order of the matrix $\underline{\underline{G}}$ is $4(2M+1)$. It can be seen that a small change in the number of scattering orders causes a large change in the order of the matrix. The right hand side of equations 24-27 have values only when ξ and η are both equal to zero (Appendix B).

The spectral amplitudes ($A(\xi, \eta)$) are obtained by solving the above system of equations. The matrix, $\underline{\underline{G}}$, is well behaved for gently varying interfaces (Aki and Larner, 1970). For a small number of scattering orders

(when the size of the matrix $\underline{\underline{G}}$ is small) and the system is solved using Gaussian elimination routine (Dongarra et al., 1979). When the scattering order is large, the G matrix can become too large to store in computer memory. To overcome this problem, solutions were obtained by solving the system using a column operations technique (see Appendix C). The spectral amplitudes obtained from the matrix inversion are then substituted into equations B2a-B2d, B4a-B4d and B6a-B6d, to obtain the other spectral amplitudes. The spectral amplitudes are subsequently substituted into equations A13-A20 and the inverse Fourier transform of these equations results in the magnetic and the electric field components in the different regions and locations of the model in Figure (5). The fields at the planar interfaces are obtained by using a 2D FFT routine, whereas the fields at the non-planar interface are obtained by summing up the spectral amplitudes over the wavenumbers at each sampling position.

Although in an MT survey, the fields of interest are the ones measured at the earth's surface, the fields at the non-planar subsurface interface were computed and boundary conditions calculated to determine the accuracy of the numerical approximation. The fields at the earth's surface, the impedances, the apparent resistivities and other parameters that can be obtained from the fields from this numerical technique will be examined in the following sections.

3.2 Reliability of Rayleigh-FFT technique.

Several papers have been published recently discussing the MT response for 3D inhomogeneities (Hibbs and Jones, 1977, Reddy et al., 1977, Ting and Hohmann, 1981 etc.), but none of these results can be compared directly with the ones obtained here as the published solutions are based on rectangular inhomogeneities. To check the reliability of the computer programs and the modeling technique, three tests were performed.

1) A one dimensional model comprising of plane, electrically homogeneous, linear and isotropic layers was used. The fields obtained agreed with those from a 1D program to the 9 significant Figures.

2) TE and TM responses from Peeples (1983) 2D program for MT response from irregular interfaces were compared with the responses determined from 3D program using the same model. The model, TE and TM fields, apparent resistivities and phases of impedances are shown in Figure 6. The differences between the fields from the 2D and 3D programs were normalized by values obtained from the 2D program for each point. The results agreed to better than 0.1 percent.

3) The final step was to determine the reliability for 3D model results. This step is very important because of the approximations and assumptions made in this numerical scheme.

The reliability of the numerical solutions to the

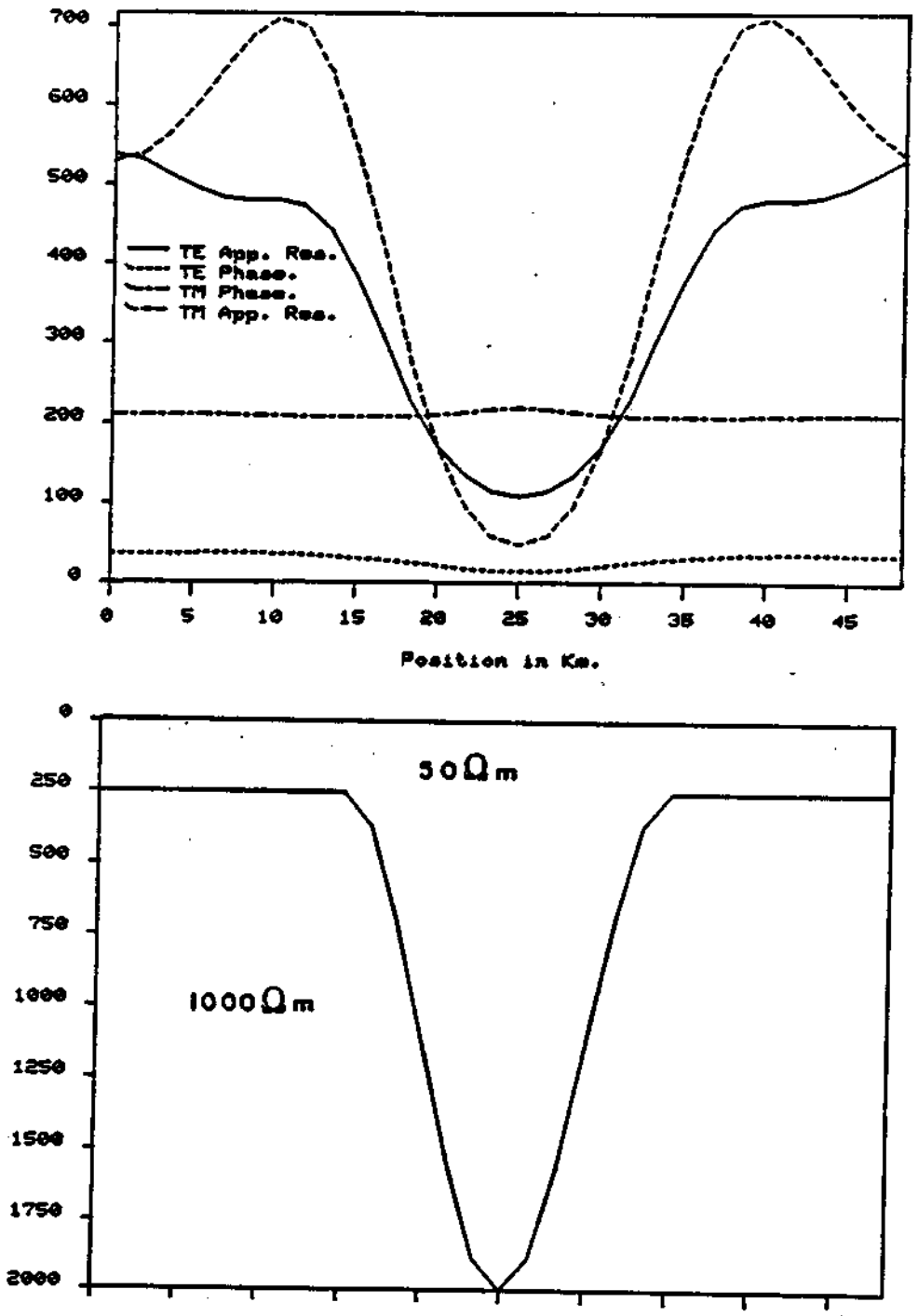


Figure 6. a) TE and TM apparent resistivities and phases obtained from 2D and 3D programs (vertical axis is apparent resistivity in Ohm-m).
b) Cross-section of the 2D model (vertical axis is depth in meters).

integral equations (B7a-B7d, Appendix B) is governed by three main sources of error (Bard and Bouchon, 1980b). Two of these are from the numerical technique and one is an inherent problem with the solution method. The first source of error is from the assumption of periodicity of the inhomogeneous zones. The solutions might be affected by 'parasitic rays' from 'adjacent' inhomogeneities. This problem is minimized by choosing repitition distances large enough such that the edge of the inhomogeneity is at least one skin depth from the outside boundary of the zone under consideration. The second source of error is from the fact that theoretically, the scattered fields should be represented by an infinite number of plane waves with discrete wavenumbers (e.g. $\xi = 2\pi m/Lx$). Since this is not numerically feasible, a maximum value M of scattering order is used such that the condition $2\pi M/\xi L_x > 1$ is satisfied. The third source of error is due to the fact that the integral equations take care of only upgoing and down going waves from the interfaces. In the case where there is a sharp curvature in the interface, there can be multiple reflections which are not accounted for. This so-called 'Rayleigh ansatz' error (error due to curvature of the interface) is the most restrictive. The error grows rapidly for slopes around unity (Bard and Bouchon, 1980b), and for a perfect electrical conductor, Jiracek (1973) suggests that the slope should be less than 0.6 to avoid intolarable errors. The effect of slope and scattering

order on the reliability of the solutions will be discussed below.

Following Aki and Larner (1970), and Jiracek (1973), the reliability of the numerical technique for the 3D problem was checked by examining the boundary conditions at the non-planar interface (equation 22), using the root mean square error of the boundary condition for a particular field component at the non-planar interface. Jiracek (1973) observed that the root mean square error is more diagnostic than the conservation of energy. Field components are calculated in the regions above and below the interface, and the normalized residue for the tangential components are determined.

For example, normalized residue for the y component of the magnetic field (NRHy) for the non-planar interface at a point is;

$$NRHy = |\gamma_y H1z - H1y - \gamma_y H2z + H2y| \,/\, |\gamma_y H1z - H1y|$$

where $\gamma_y = -\frac{\partial f(x,y)}{\partial y}$

Root mean square errors for all the observation points are calculated for a particular component of the total field. Percentage root mean square error for the x-component of the electric field (RMSEEx) is;

$$\text{RMSEEx} = \left\{ \frac{\sum_{1}^{M}\sum_{1}^{N} |\Delta Ex||\Delta Ex|}{NM \sum_{1}^{M}\sum_{1}^{N} |-\gamma_x E1z + E1x| \, |-\gamma_x E2z + E2x|} \right\}^{1/2} \times 100$$

where;

$$\Delta Ex = E1x - \gamma_x E1z - E2x + \gamma_x E2z$$

$$E1x = E1x(m\Delta x, n\Delta y) \text{ etc.,}$$

Δx and Δy are sampling intevals and

$$\gamma_x = -\frac{\partial f(x,y)}{\partial x}$$

One of the crucial numerical approximation is the truncation to a finite number of plane waves. This approximation limits the number of scattering orders to be included in a solution. In order to determine the effect of increasing the number of scattering orders on the solution, the model shown in Figure 7 was used. The inhomogeneity in this model has a resistivity of 50 Ohm-m, and the resistivity of half-space is 1000 Ohm-m. The scattering orders were varied from M = 2 to M = 6 (i.e. N = (2M+1) = 9 to N = (2M+1) = 13) for a frequency of 1Hz. Figures 8 and 9 show the plots for the normalized residuals for the x-component of the electric field and y-component of the magnetic field and Figures 10 and 11 show plots for the magnetic and electric field components at the model surface for total scattering orders of 13. It is evident from the Figures that an increase in the scattering orders decreases the mismatch of the boundary conditions. From the normalized residual plots, it can be seen that the

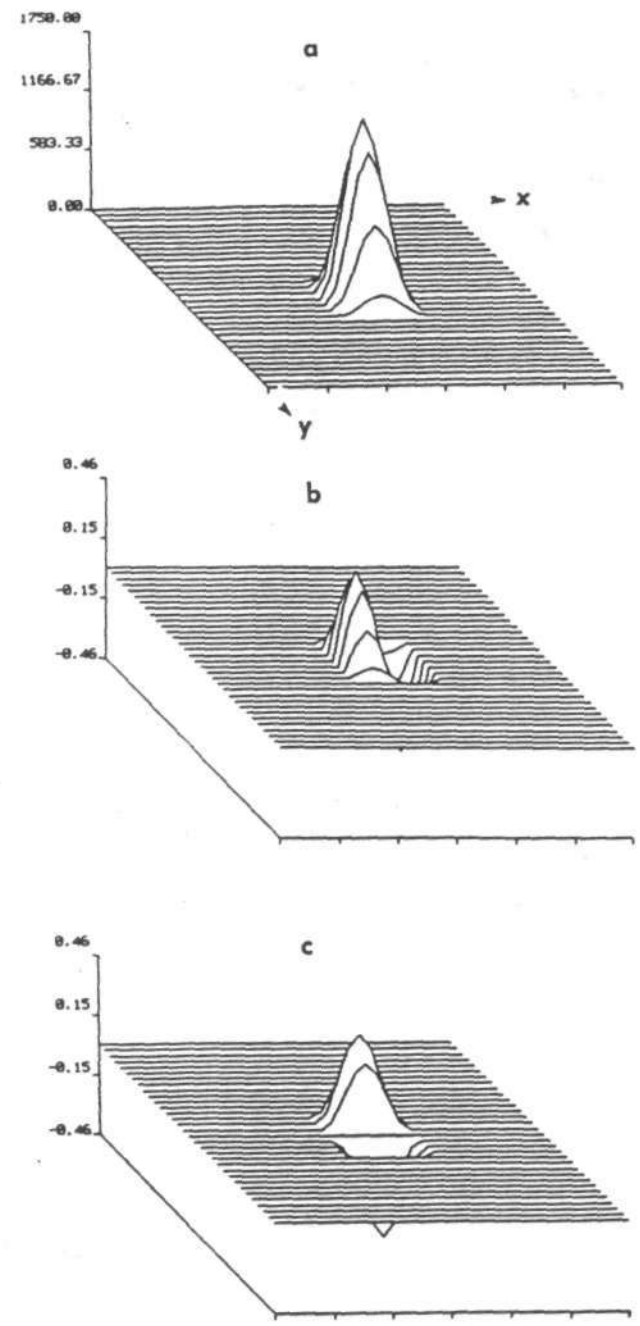


Figure 7. a) Topography of the non-planar interface (vertical scale is in meters and the horizontal dimension is 50 by 50 Km).
b) Derivative of the interface along x-axis.
c) Derivative of the interface along y-axis.

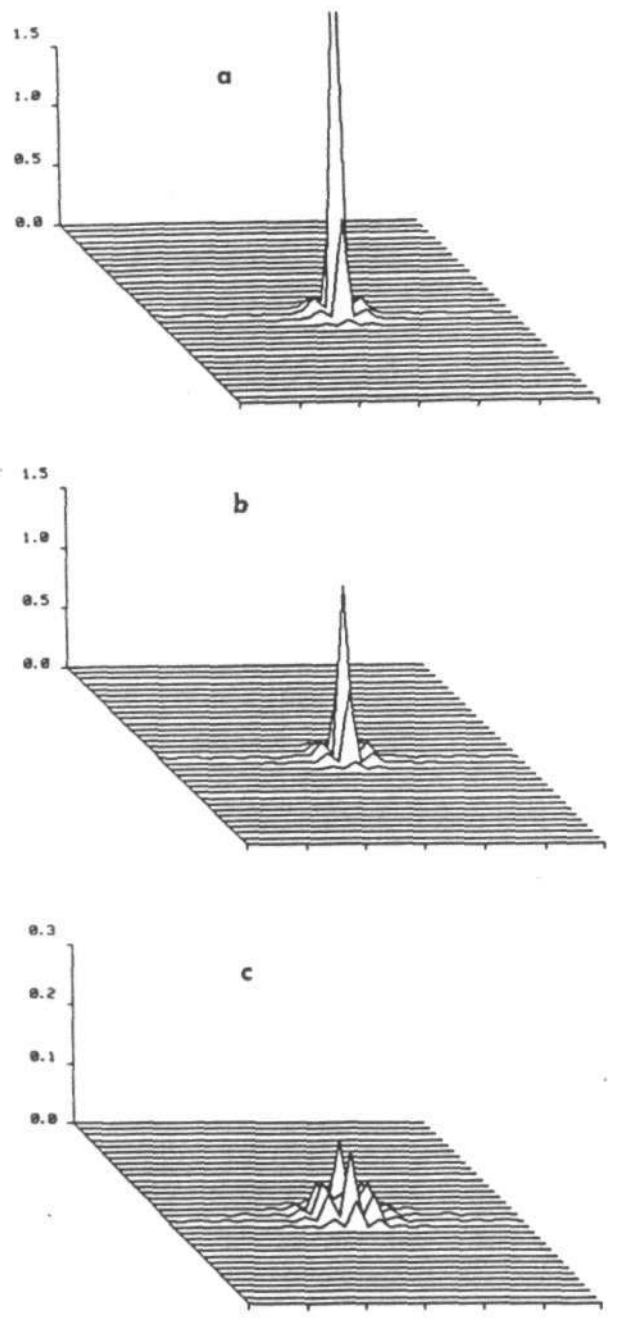


Figure 8. Normalized residuals at the non-planar interface of the x-component of the electric field for scattering orders of a) 9, b) 11 and c) 13.

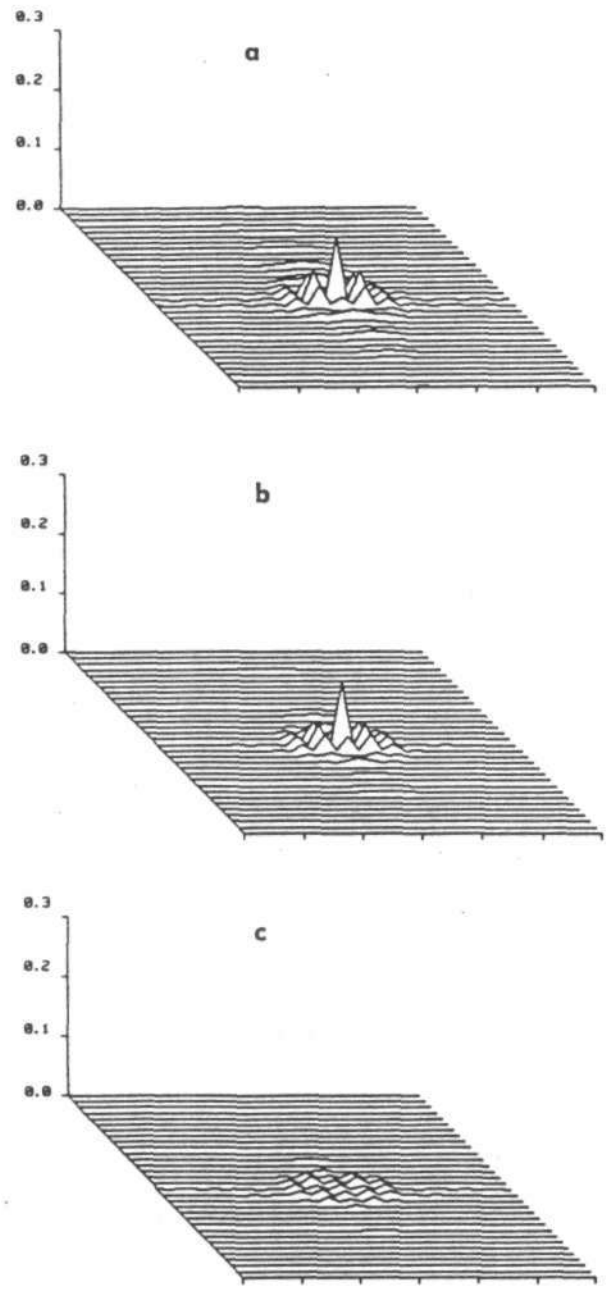


Figure 9. Normalized residuals at the non-planar interface of the y-component of the magnetic field for scattering orders of a) 9, b) 11 and c) 13.

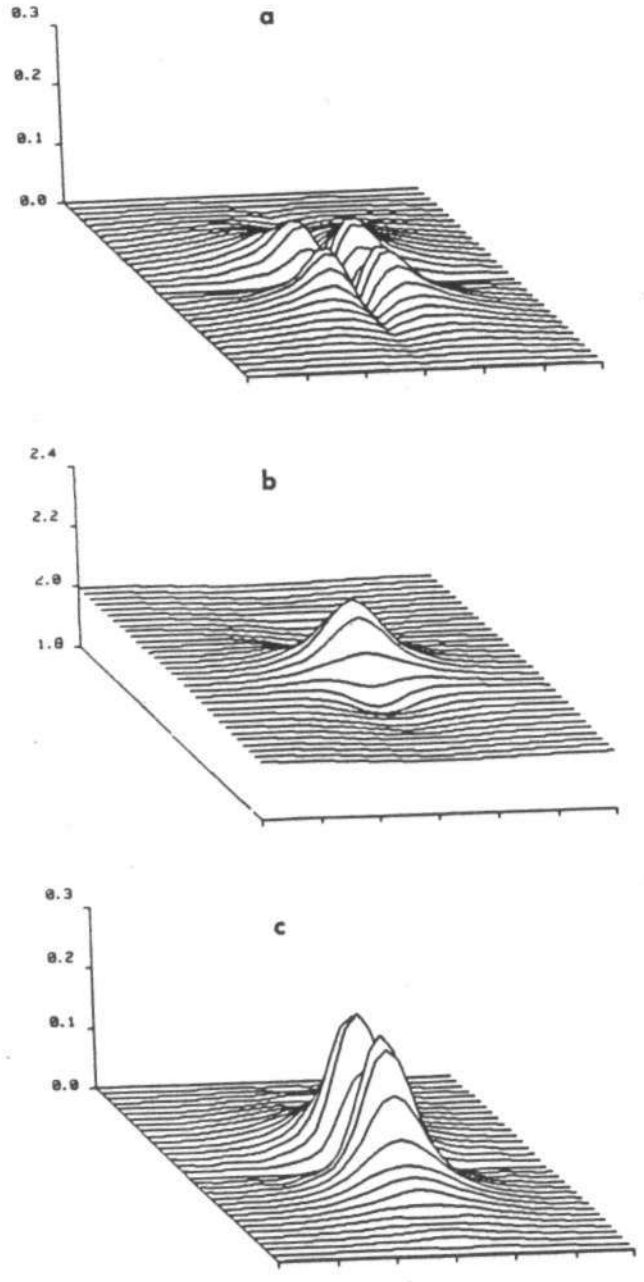


Figure 10. Amplitudes of the magnetic field components at Z=0 for the model in Figure 7, a) Hx, b) Hy and c) Hz.

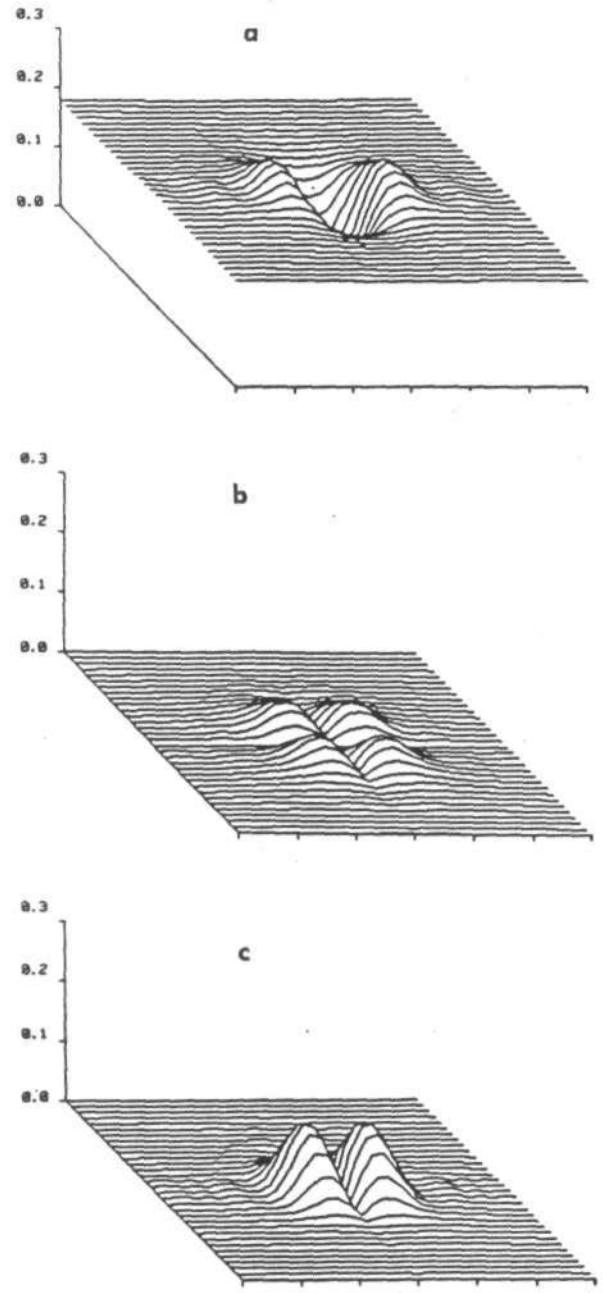


Figure 11. Amplitudes of the electric field components at Z=0 for the model in Figure 7, a) Ex, b) Ey and c) Ez.

mismatch in the boundary conditions is more pronounced in the vicinity of maximum curvature in the subsurface interface. Also Figures 12 and 13 show plots of the profiles of the x-component of the electric field and the y-component of the magnetic field with increase in scattering orders. From these Figures, it is evident that increasing the scattering order improves the solution. Note also that the oscillations in the fields die out as the scattering order is increased. This model has a maximum slope of 25 degrees and the total number of scattering orders needed for an adequate solution is 13. This model has a 3 percent RMS error for both the magnetic and electric field components.

One would like to increase the total number of scattering orders further, but the time required for the inversion of the resulting matrix is excessive. CPU times for CDC 6600 for the solution of the problem for different scattering orders considered and the sizes of the matrices inverted are shown in Table 1 and Figure 14. Note that matrix inversion is the major component of CPU time usage. A faster routine for matrix inversion would significantly reduce the total amount of computation time.

A second model shown in Figure 15 was used to determine the effect of interface slope on the solution reliability. Figure 15 shows plots of the non-planar interface for the model and the derivatives along x and y axes. The depth to the top of the inhomogeneity, its

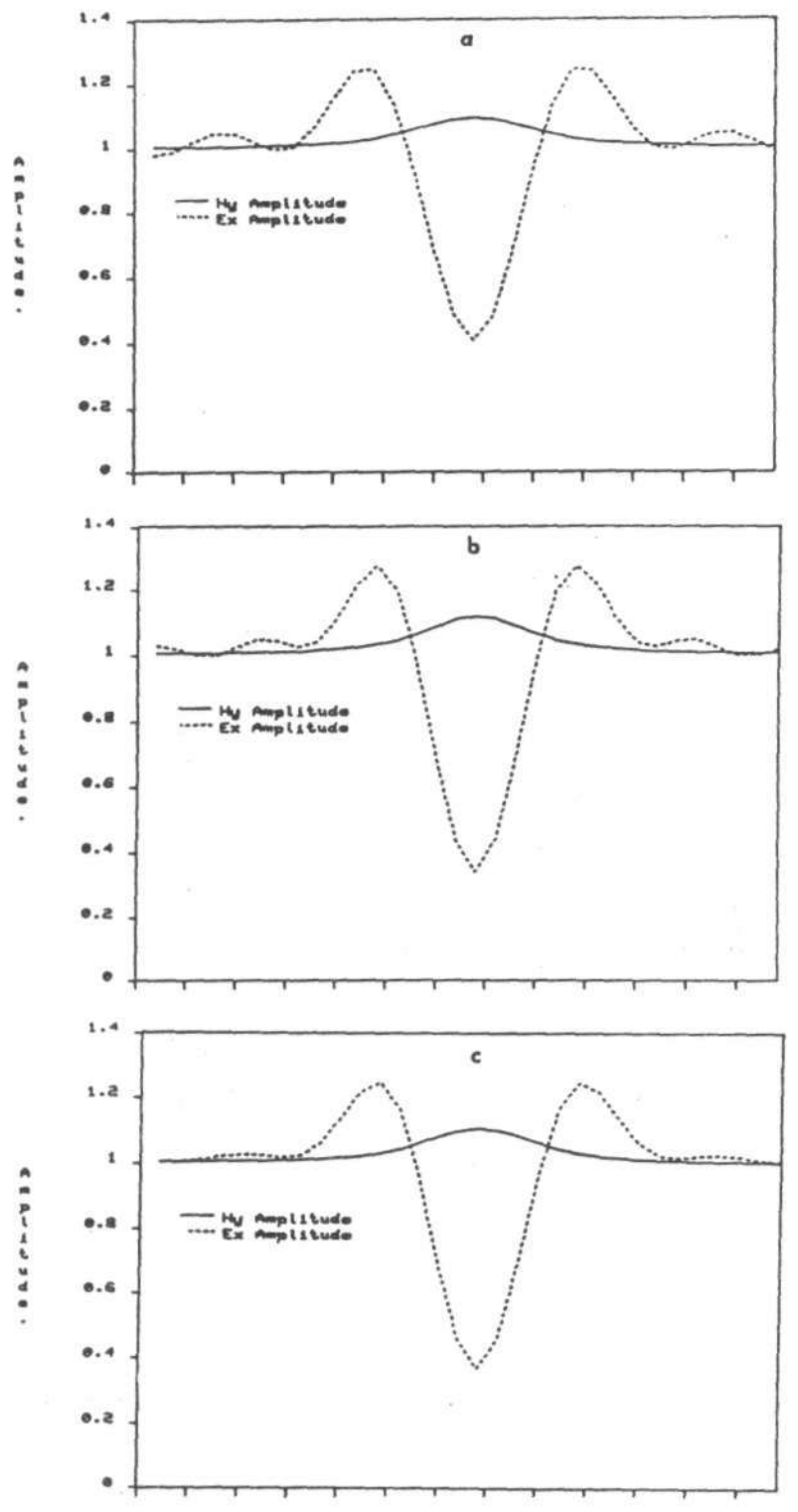


Figure 12. Profiles of the normalized amplitudes of Ex and Hy at Z=0 along the x-axis for scattering orders of a) 9, b) 11 and c) 13.

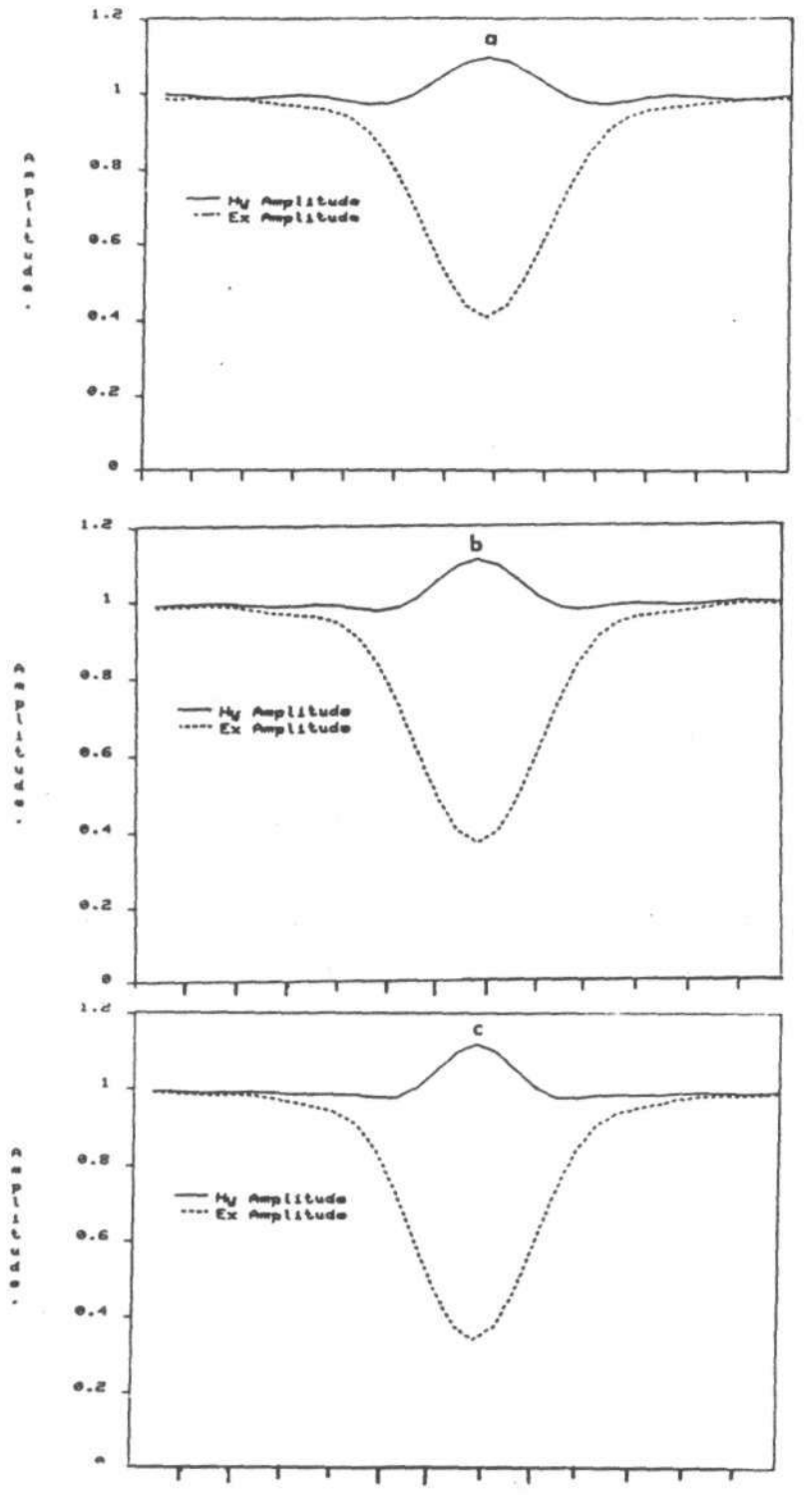


Figure 13. Profiles of the normalized amplitudes of Ex and Hy at Z=0 along the y-axis for scattering orders of a) 9, b) 11 and c) 13.

TABLE 1

THE RELATIONSHIP BETWEEN TOTAL NUMBER OF SCATTERING ORDERS AND COMPUTATION TIME

TOTAL SCATTERING ORDERS (M+1)	MATRIX SIZE 4(2M+1)	CPU TIME MATRIX INVERSION (secs)	CPU TIME FFT (secs)	TOTAL CPU TIME (secs)
5	100	11	142	153
7	196	69	278	347
9	324	294	458	752
11	484	947	620	1567
13	676	2529	871	3400
15	900	5957	1158	7115

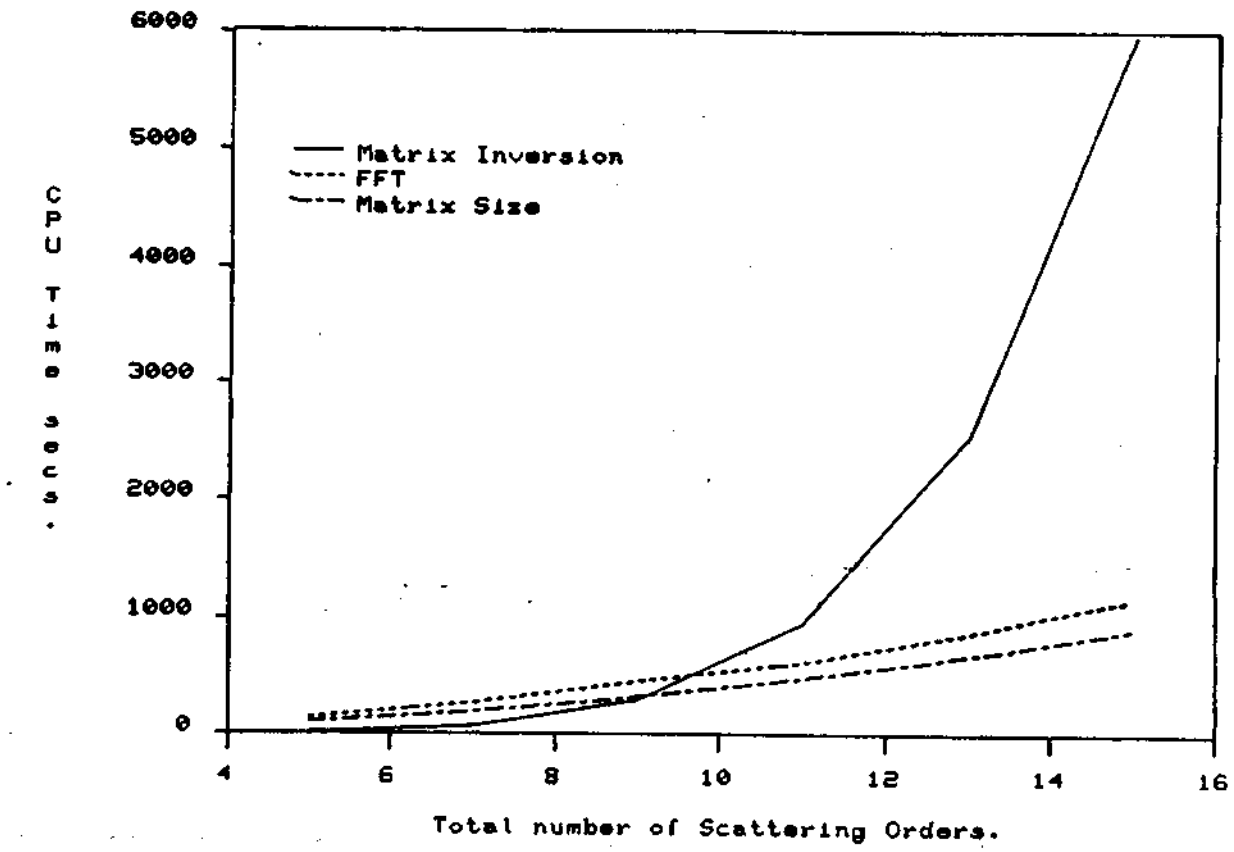


Figure 14. Total scattering orders versus CPU times for matrix inversion and FFT and matrix size.

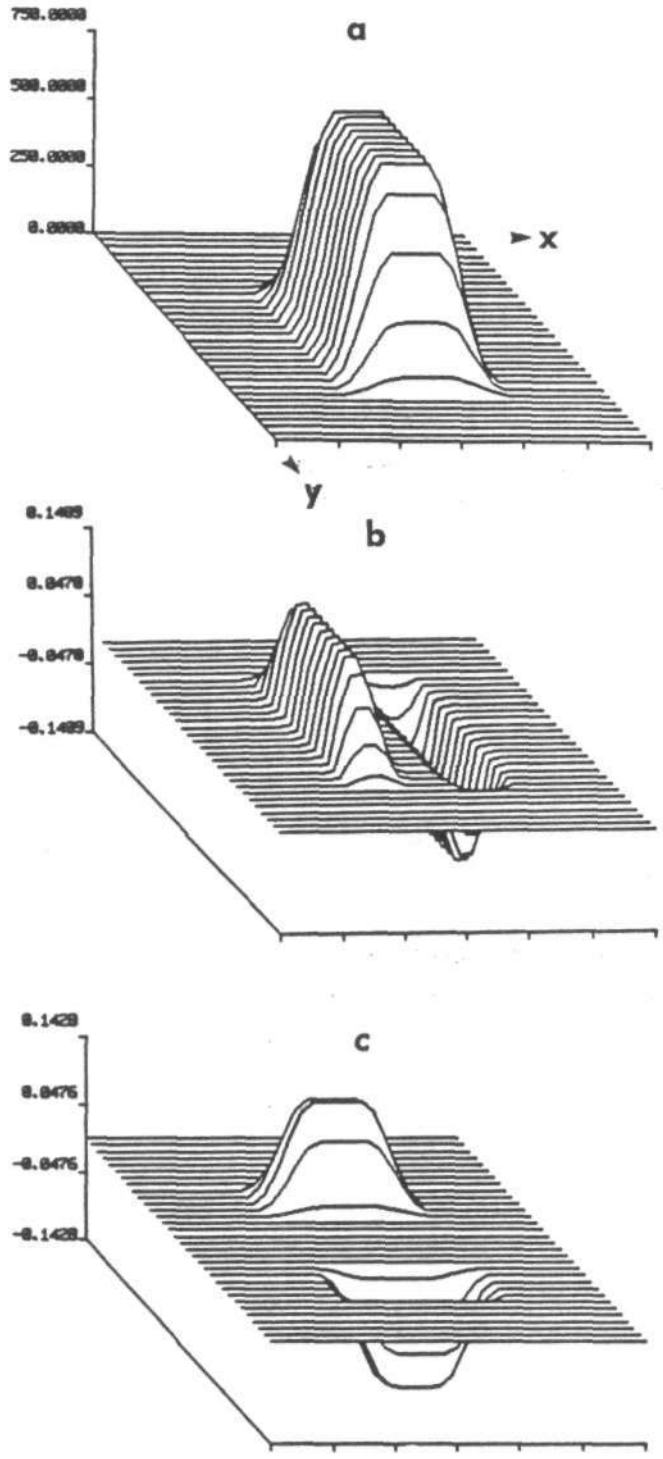


Figure 15. a) Topography of the non-planar interface for model E (vertical scale is in meters and the horizontal dimension is 50 by 50 Km).
b) Derivative of the interface along x-axis.
c) Derivative of the interface along y-axis.

height and its aspect ratio is kept constant, while the slopes of the sides are varied. The resistivity of the inhomogeneity is 50 Ohm-m, and that of the half-space is 1000 Ohm-m, and the frequency of the incident waves is 1 Hz. Table 2 and Figure 16 show the maximum interface slope along the x and y dirtections versus the percentage RMS errors determined from the mismatch of the boundary conditions at the non-planar interface for the x-component of the electric field and the y-component of the magnetic field. Figure 17 shows plots of the normalized residuals at the non-planar interface of the x-component of the electric field and y-component of the magnetic field for different values of the maximum slope of the interface as well. It is evident from the Tableand Figures that the higher the slope for a given scattering order (in this case 13), the less reliable the solution.

The accracy of the solution for this technique depends on maximum slope (or minimum radius of curvature) of the interface and the total number of scattering orders included in the solution. The total number of scattering orders can be calculated from equation 23. From this equation, it can be seen that the angles of scattering depend on the conductivity of the medium, the frequency of the incident waves, the scattering order and repitition distance. To obtain accurate solution, the scattering order has to be such that all the angles of scattering up to 90 degrees are included in the solution and usually a

TABLE 2

THE RELATIONSHIP BETWEEN INTERFACE SLOPE AND PERCENTAGE ROOT MEAN SQUARE ERRORS

MAXIMUM SLOPE (degrees)	RMSEEx (percent)	RMSEHy (percent)
8	1.0	2.1
18	7.0	4.3
27	17.5	7.3
42	59.1	18.5

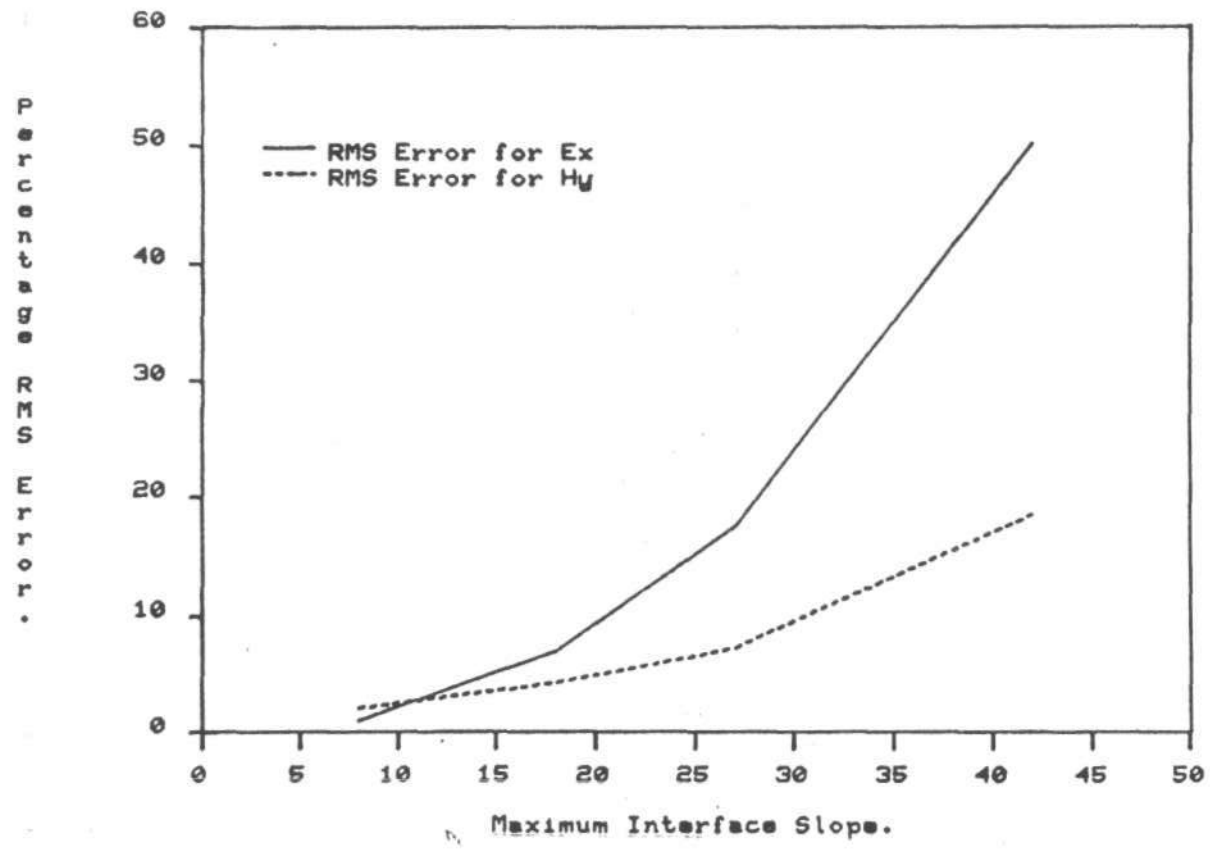
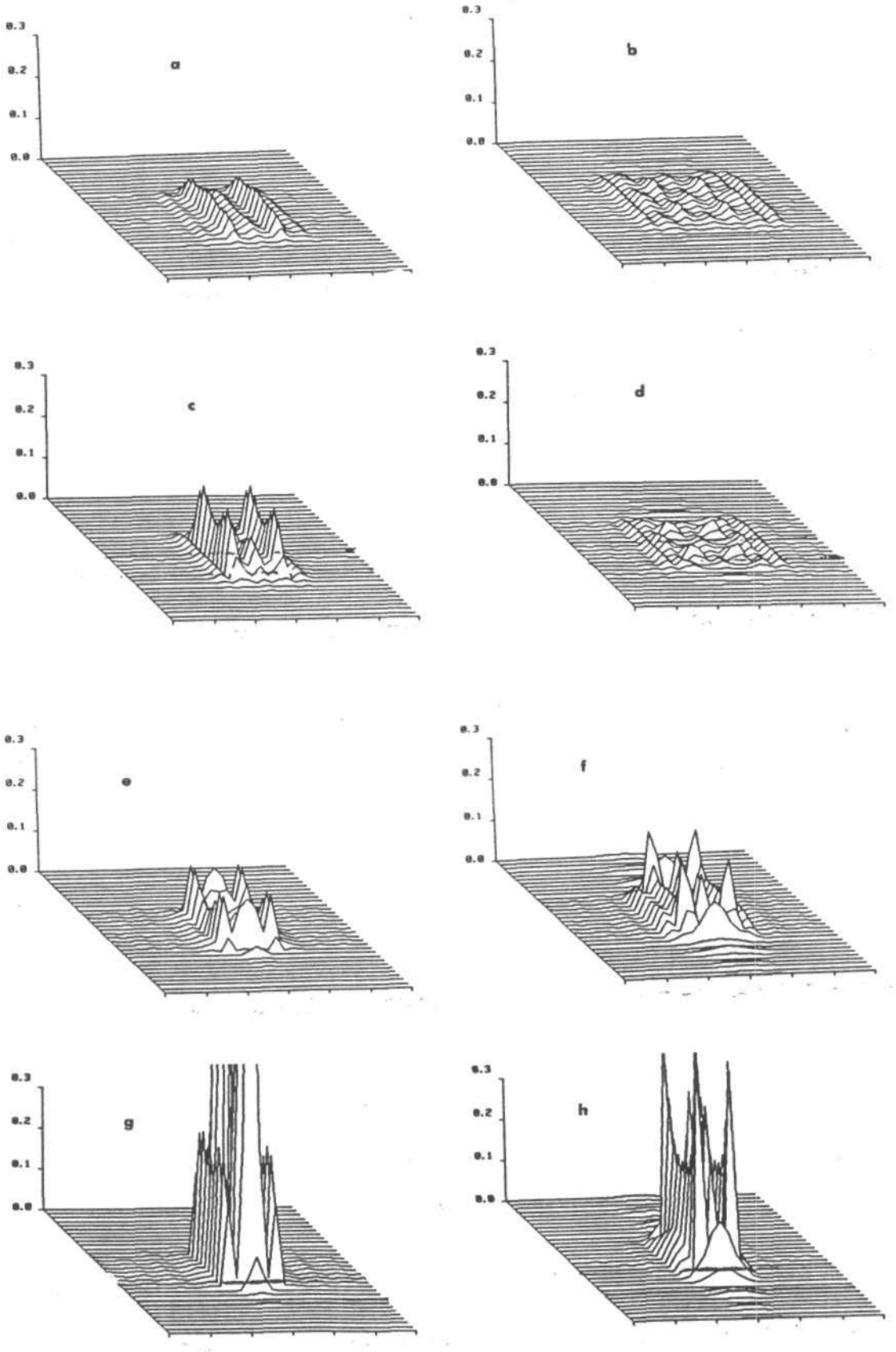


Figure 16. Maximum interface slope versus percentage RMS errors for Ex and Hy.

Figure 17. Normalized residuals for the x-component of the electric field (NREx) and y-component of the magnetic field (NRHy) at the non-planar interface for different values of maximum slopes of the interface.

a) NREx with maximum slope of 8 degrees.
b) NRHy with maximum slope of 8 degrees.
c) NREx with maximum slope of 18 degrees.
d) NRHy with maximum slope of 18 degrees.
e) NREx with maximum slope of 27 degrees.
f) NRHy with maximum slope of 27 degrees.
g) NREx with maximum slope of 42 degrees.
h) NRHy with maximum slope of 42 degrees.


0.3
0.2
0.1
0.0
a
b
c
d
e
f
g
h

few more.

Additional experiments were carried out with two other models. In the first case, the inhomogeneity has a resistivity of 5 Ohm-m, and in the second one it has a resistivity of 10 Ohm-m. For the two cases, the inhomogeneities are buried 0.5 Km below the model surface in a homogeneous half-space of 100 Ohm-m resistivity. Percentage RMS errors for the y-component of the magnetic field were calculated for two interface slopes of 15 and 28 degrees for the two models. Figure 18 shows plots of the scattering order versus percentage RMS error for the two cases. For the two cases, both higher resistivities and more gentle slopes give lower errors for the same scattering order. The total number of scattering orders needed to include all the scattering angles up to 90 degrees for the 5 Ohm-m body with repetition distance of 20 Km and incident waves of frequency of 1 Hz is 9. Note that the decrease in the RMS errors for this inhomogeneity (with slope of 28 degrees) between scattering orders of 5 to 9 is about 5 percent, and the change in RMS error for an increase in scattering orders of 9 to 15 is about 1.5 percent (Figure 18). The computation time increases about 9 times for a solution using 9 as oppossed to 15 scattering orders (Figure 14).

Since the total number of scattering orders and the slope of the interface both affect the reliability of the solutions, and since increase in scattering orders

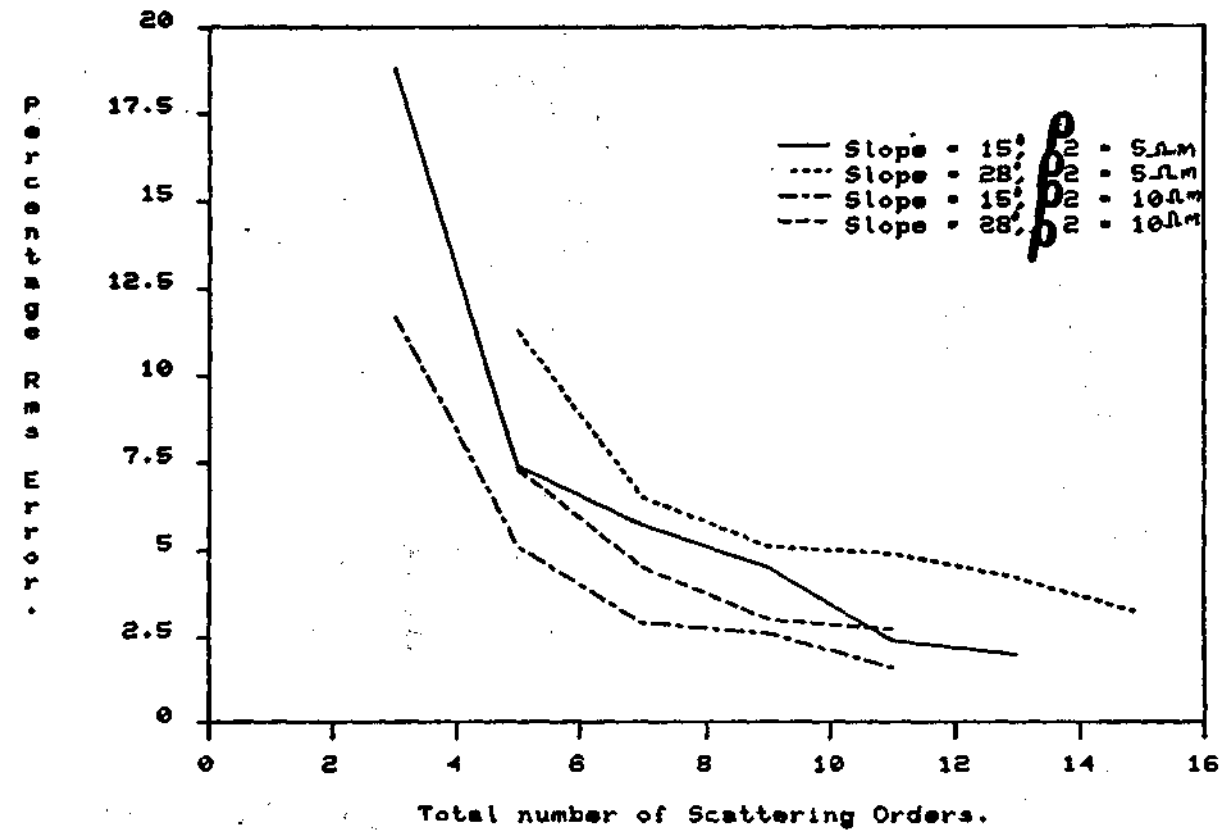


Figure 18. Total number of scattering orders versus percentage RMS errors for inhomogeneities of resistivities of 5 and 10 Ohm-m and slopes of 15 and 28 degrees in a 100 Ohm-m half-space.

increases computation time, a reasonable trade off of the two has to be sought for the problem being solved. The gentler the slope, the more accurate the solution for a given scattering order, although a similarly reliable solution could be obtained with higher scattering orders for a steeper slope if the computer time needed for the computation is available.

CHAPTER 4

MAGNETOTELLURIC RESPONSE FOR CONDUCTIVE AND RESISTIVE 3D INHOMOGENEITIES

MT response for 3D inhomogeneities were computed using different types of earth models. The models were chosen to facilitate comparison with previous studies in the literature. As the solution technique developed in this study can accomodate gently varying interfaces, a combination of planar and non-planar interfaces are used in order to construct the desired inhomogeneity. (Note that previously published models cannot be exactly duplicated by Rayleigh-FFT technique, since this technique can best handle only gently varying interfaces, so the comparisons were done in a gross sense).

In this chapter, the models are described. The resultant fields, impedances, apparent resistivities, skew, tipper magnitude and azimuth are presented.

4.1 3D Models.

The models used consist of two planar and one non-planar interfaces (Figure 5). The non-planar interface is:

$$f(x,y) = H(1 + \cos\pi((x-d1x)/d2x))(1 + \cos\pi((y-d1y)/d2y))$$

$$\text{for} \quad -(d1x+d2x) < x < (d1x+d2x) \text{ and}$$
$$-(d1y+d2y) < y < (d1y+d2y)$$

$$f(x,y) = 0$$

$$\text{for} \quad x > |(d1x+d2x)| \text{ and}$$
$$y > |(d1y+d2y)| .$$

Figure 19 is a cross section of the model. Values of d2x and d2y can be varied to change the slopes of the edges of the inhomogeneity. To reproduce a 3D inhomogeneity in a homogeneous half-space, the mean depths to the first and second subsurface interfaces are chosen to be equal (i.e. A = HD, Figure 19), and the values of resistivities in regions 1 and 3 are also the same.

4.2 Model A.

Model A, a buried conductor, is similar to the Ting and Hohmann (1981) model. It comprises of an inhomogeneity buried in a more resistive half-space, the resistivity of the regions 1 and 3 is 100 Ohm-m, and the inhomogeneity, is 5 Ohm-m. The depth to the first and second interfaces is 0.75 Km, the height of the inhomogeneity, H, is 0.5 Km, 2d1x is 1 Km, 2d1y is 2 Km and d2x = d2y is 1.5 Km.

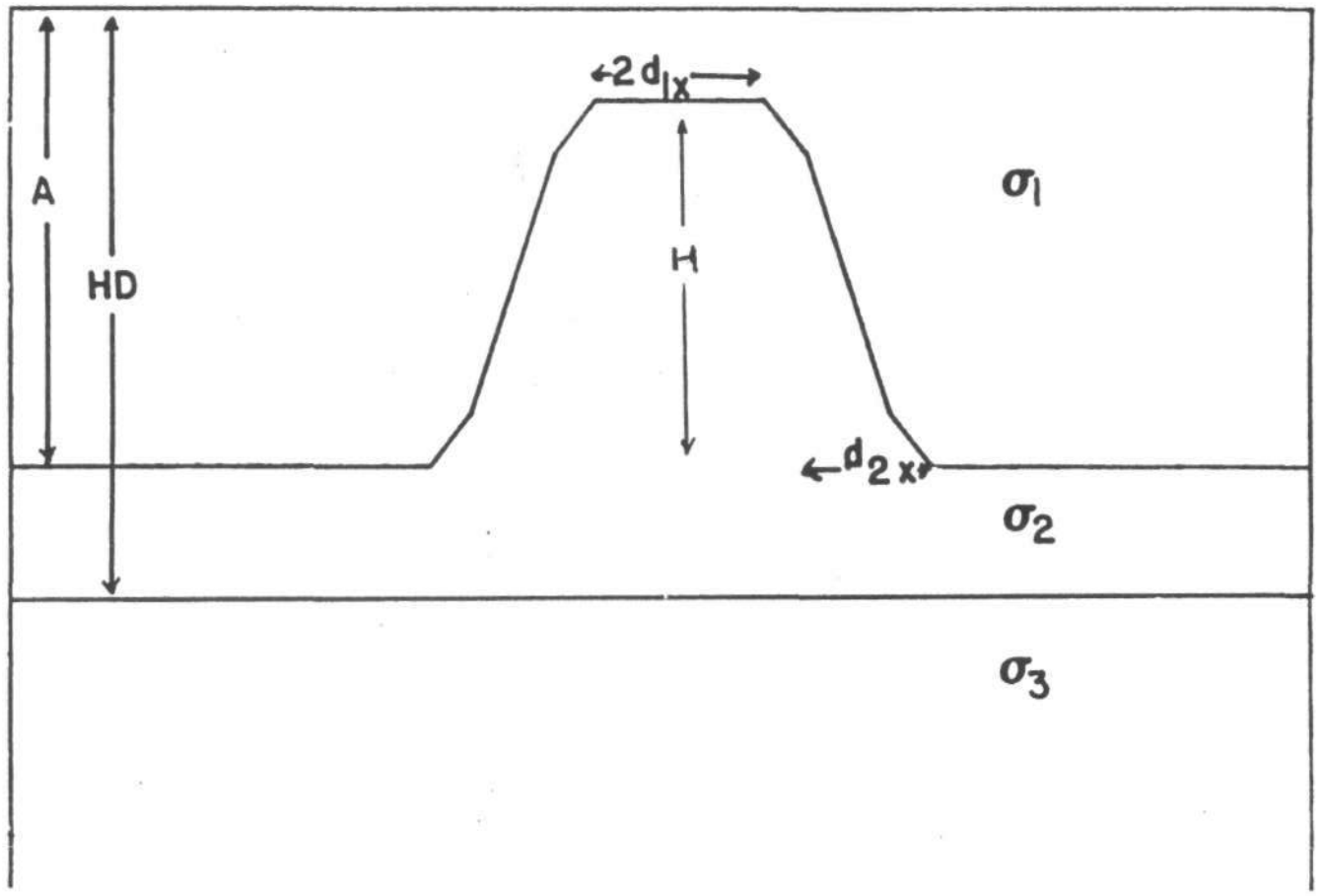


Figure 19. A cross-section of the subsurface model (x-z plane), used for forming 3D inhomogeneity.

Frequency of the incident waves is 1 Hz and the repetition distance in both x and y directions (Lx and Ly) is 20 Km. Figure 20a is a plot of the first subsurface interface and Figure 20b is a cross section of the inhomogeneous zone.

4.2.1 Field Components for Model A.

The magnetic and electric field components for model A at Z = 0 (with the magnetic field component of the incident waves polarized in the y-direction) are shown in Figures 21 and 22. These field components were computed using a total scattering order of 13. The root mean square errors (RMSE) for the y-component of the magnetic field and x-component of the electric field are computed at the non-planar interface (chapter 3) are 4.2 and 5.8 percent respectively. As expected, the x-component of the electric field and the y-component of the magnetic field have lower and higher values respectively above the zone of the inhomogeneity than that of the half-space, as shown in chapter 2. This reflects the fact that the inhomogeneity is more conductive than the half-space. Figures 23a and b show plots of two perpendicular profiles of the normalized amplitudes of x-component of the electric field and y-component of the magnetic field and their phases. The plots are similar to those of Stodt et al. (1981) for a similar model (Figure 3).

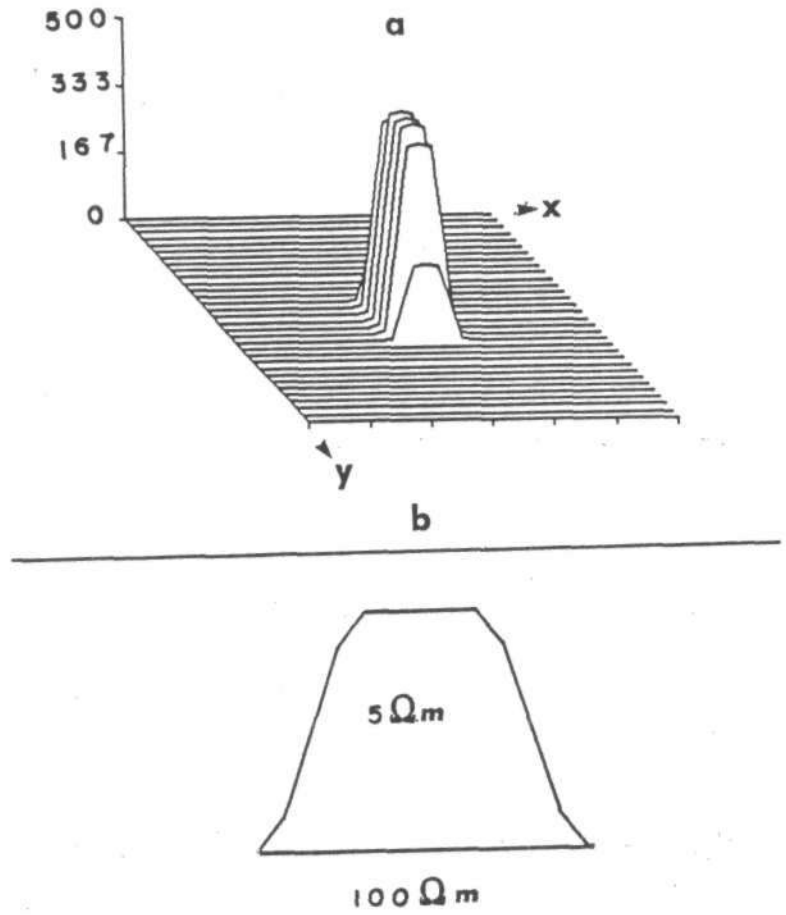


Figure 20. a) Topography of the non-planar interface for model A (vertical scale is in meters and horizontal dimesion is 20 by 20 Km).
b) A cross-section of the model along x-axis (not to scale).

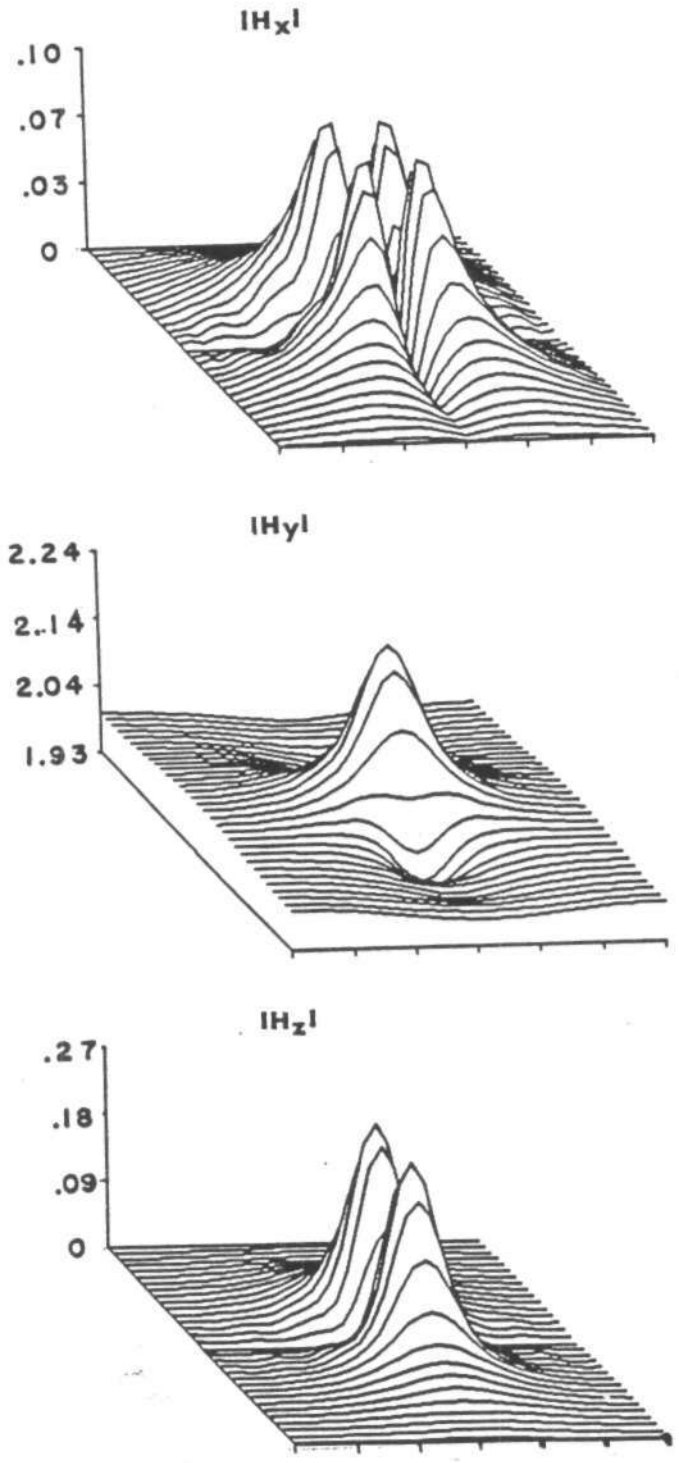


Figure 21. Amplitudes of the magnetic field components at z=0 for model A.

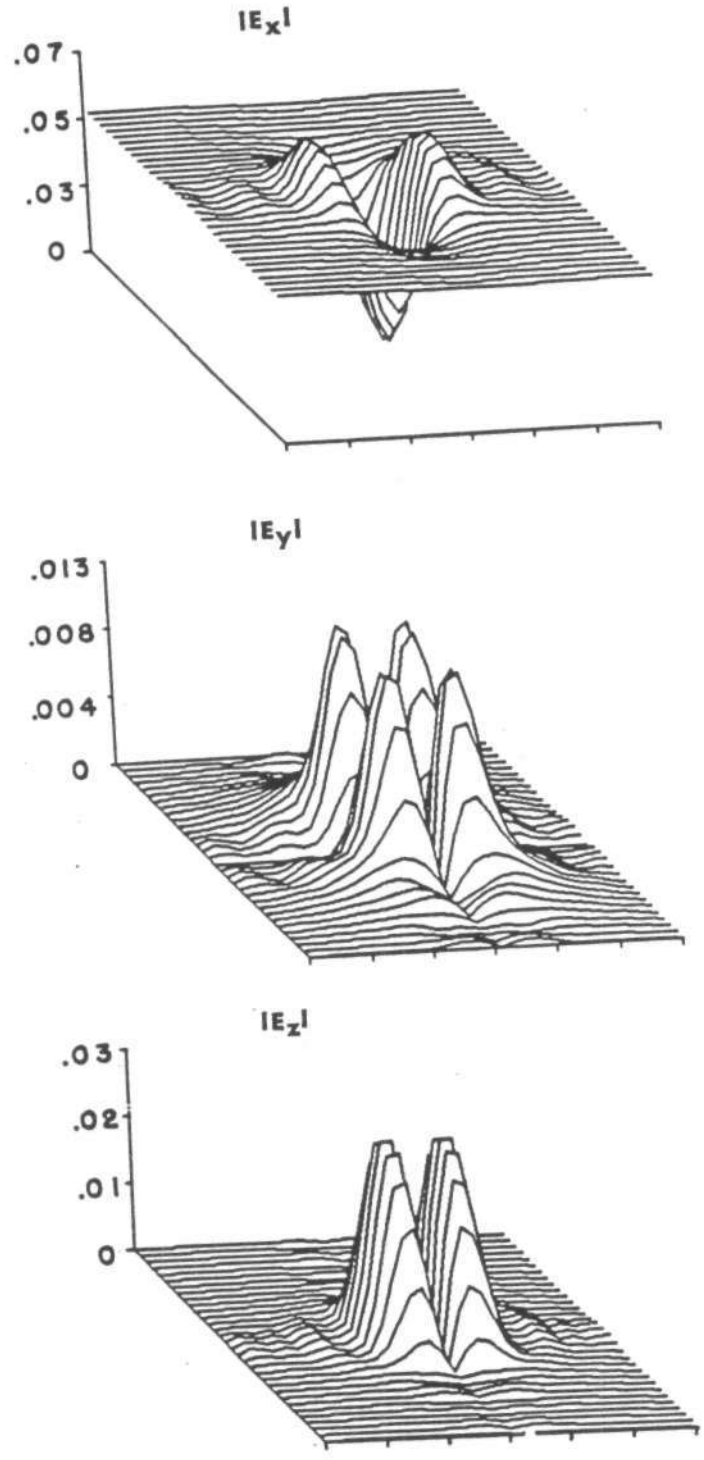


Figure 22. Amplitudes of the electric field components at z=0 for model A.

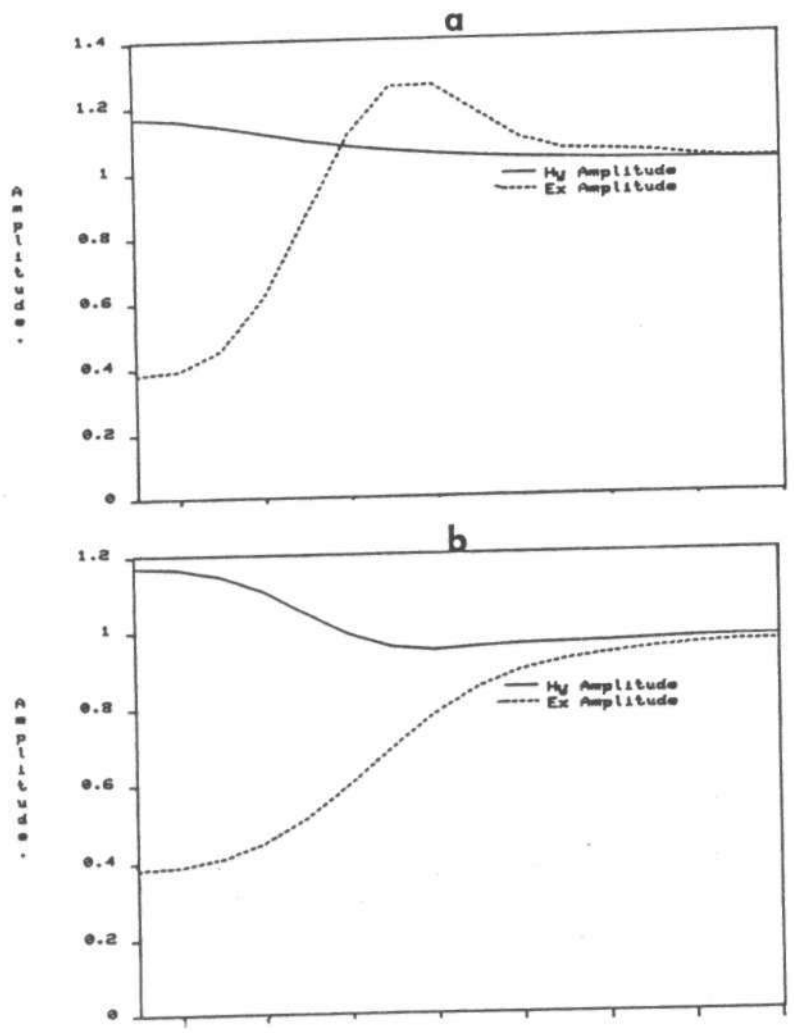


Figure 23. Profiles of the normalized amplitudes of the x-component of the electric field and y-component of the magnetic field through the center of the inhomogeneity at Z=0 along a) x-axis and b) y-axis (for interface slope of 15 degrees).

4.2.2 Apparent Resistivities and other Parameters for Model A.

The total electromagnetic field observed at the earth's surface along arbitrary directions x and y changes with time. This can be attributed to the fact that the location of the source changes with time and several sources may simultaneously contribute to the same field. The changes in the total electromagnetic field result in the variations of the calculated apparent resistivity values determined from the values of the apparent scalar impedances Zxy = Ex/Hy and Zyx = Ey/Hx (Kaufman and Keller, 1981). These impedances usually depend on a) electrical characteristics of the medium, b) the direction of the sensor axis and c) the orientation of the arrival of the primary field. The last factor makes it almost impossible to interpret results based on the apparent impedance values since the direction of polarization of the source field is unknown. In the late 1950's, researchers devised the impedance tensor method which uses parameters that are not subject to the effects of elliptical polarization of the field (Kaufman and Keller, 1981). The following is a brief discussion of how the elements of the impedance tensor are obtained.

Elements of the impedance tensor were obtained by using the field components from two different source polarizations. The relationships for the elements of the

impedance tensor as given by Vozoff (1972) are in Appendix D. Field components were obtained for two orthogonal source polarizations. The components of the fields in one direction are primed, and unprimed in the second direction. The impedance tensor elements obtained from the fields due to the two source polarizations are;

$$Zxx(\omega) = \frac{Ex1(\omega).Hx'(\omega) + Ey'(\omega).Hy1(\omega)}{Hx1(\omega).Hx'(\omega) + Hy'(\omega).Hy1(\omega)}$$

$$Zyy(\omega) = \frac{Ey1(\omega).Hy'(\omega) + Ex'(\omega).Hx1(\omega)}{Hy'(\omega).Hy1(\omega) + Hx'(\omega).Hx1(\omega)}$$

$$Zxy(\omega) = \frac{-Ey'(\omega).Hx1(\omega) + Hy'(\omega).Ex1(\omega)}{Hx'(\omega).Hx1(\omega) + Hy'(\omega).Hx1(\omega)}$$

$$Zyx(\omega) = \frac{Ex'(\omega).Hy1(\omega) - Hx'(\omega).Ey1(\omega)}{-Hy'(\omega).Hy1(\omega) - Hx'(\omega).Hx1(\omega)}$$

Using the impedance tensor elements the values of apparent resistivities; ρxx, ρyy, ρxy and ρyx were calculated. Details of the impedance tensor elements, apparent resistivities, skew, tipper and other parameters are given in Appendix D. Figure 24 shows the different apparent resistivities at Z = 0. Figures 25a, b and c show plots of the skew, tipper magnitude and tipper azimuth (in a quadrant) respectively. These values compare well in a

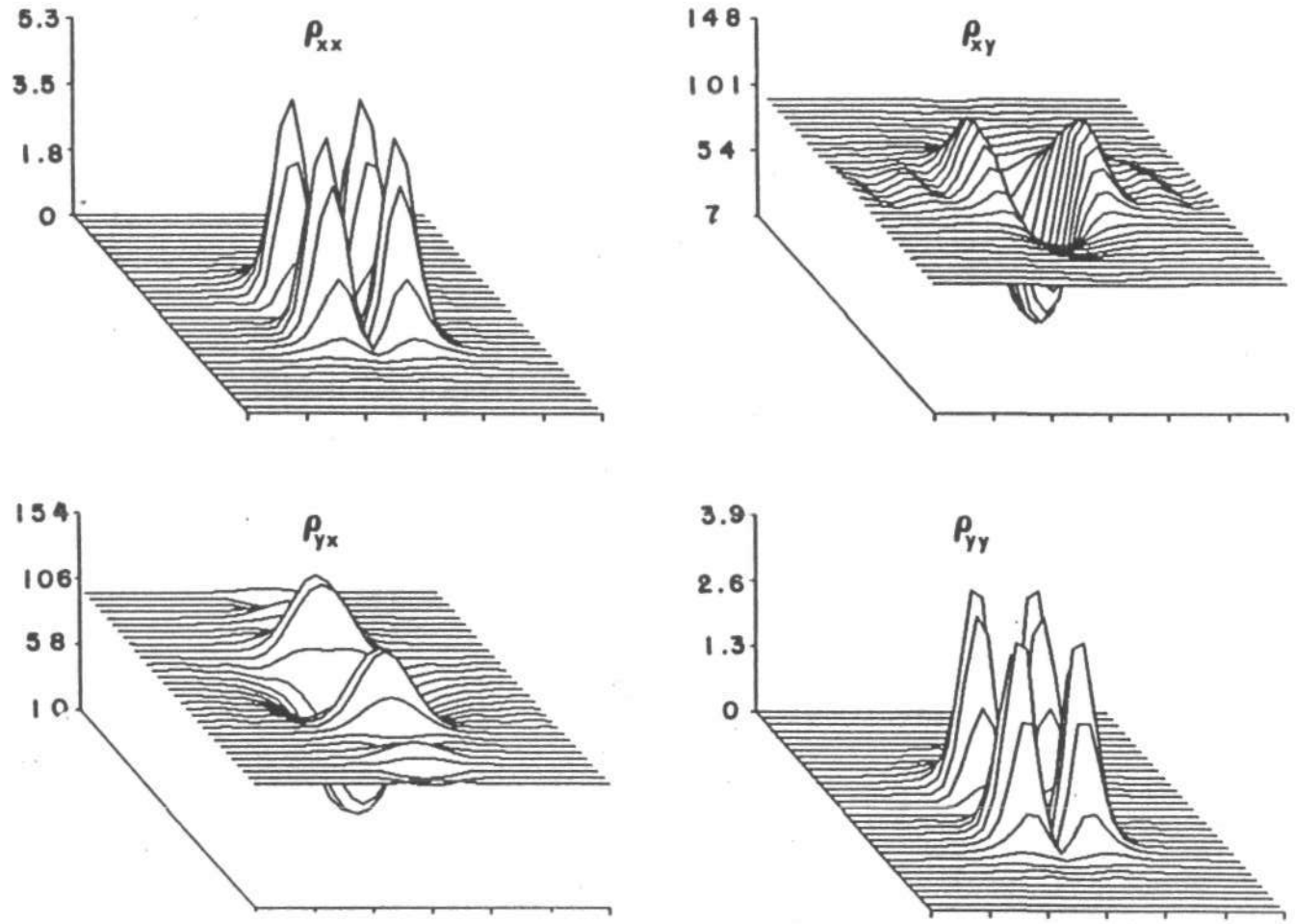


Figure 24. Apparent resistivities for model A at 1.0 Hz.

gross sense with those of Ting and Hohmann (1981) for a similar model (Figures 26a, b andc). The tipper azimuth points away from the conductive inhomogeneity as expected, and the magnitude of skew is greater than zero near the corners of the inhomogeneity, and the magnitudes of tipper is greater than zero in the zone of the inhomogeneity.

4.3 Model B.

Model B is similar to the island structure modeled by Hibbs and Jones (1977). The height of the island above the half-space basement, H, the depth of the sea water, A, and the depth to the half-space, HD, are all equal to 2 Km (Figure 19). Resistivity of sea water is 0.25 Ohm-m and that of the island and the half-space, $\rho 2$ and $\rho 3$, is 1000 Ohm-m. The dimensions of the island are; 2d1x is 6 Km, 2d1y is 8 Km, and d2x and d2y are both equal to 8 Km. Repetition distances in both x and y directions are 90 Km. The incident plane wave with the magnetic field components polarized in the y direction has a frequency of 0.001 Hz. Figure 27a is a plot of the island structure, and Figure 21b is the cross-section.

4.3.1 Field Components for Model B.

The magnetic and electric field components at z=0 for model B are calculated. Figures 28 and 29 show plots of

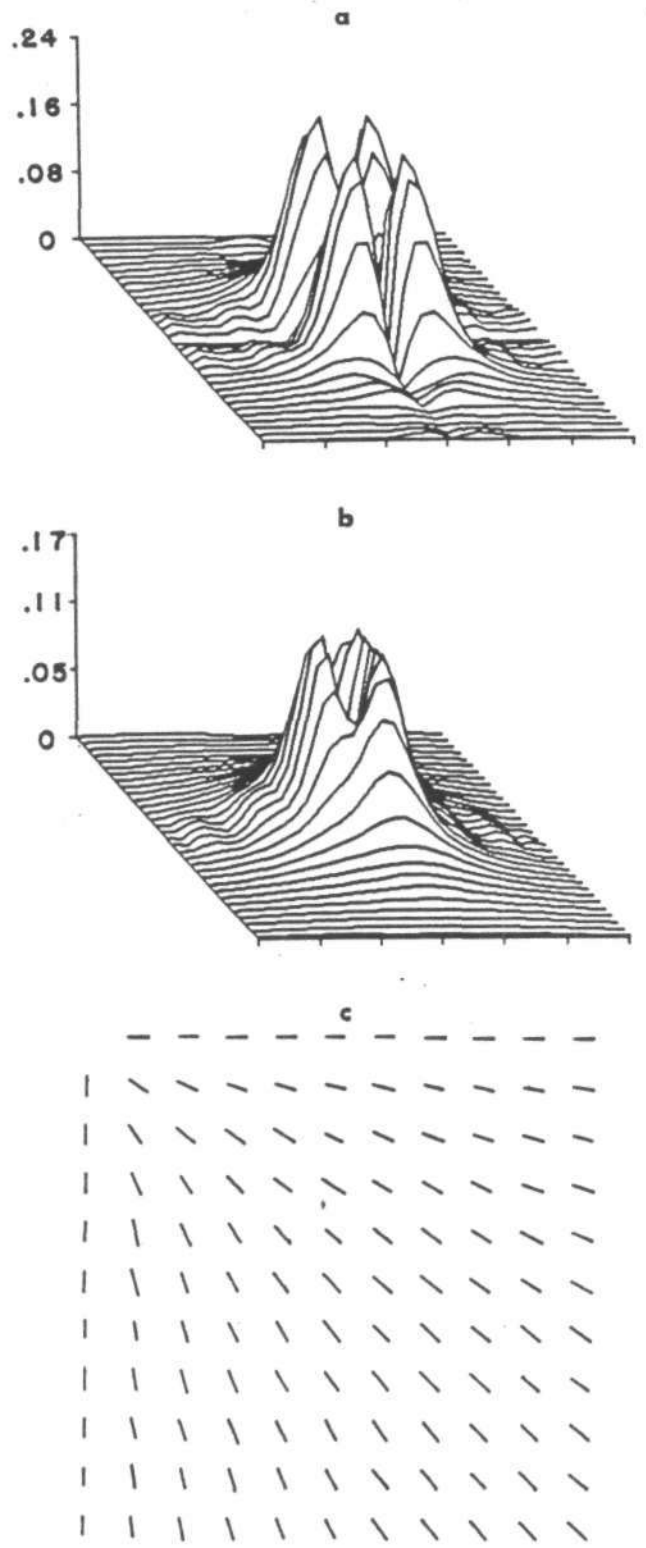


Figure 25. a) Skew, b) Tipper magnitude and c) Tipper azimuth in the 4th quadrant for model A at 1.0 Hz.

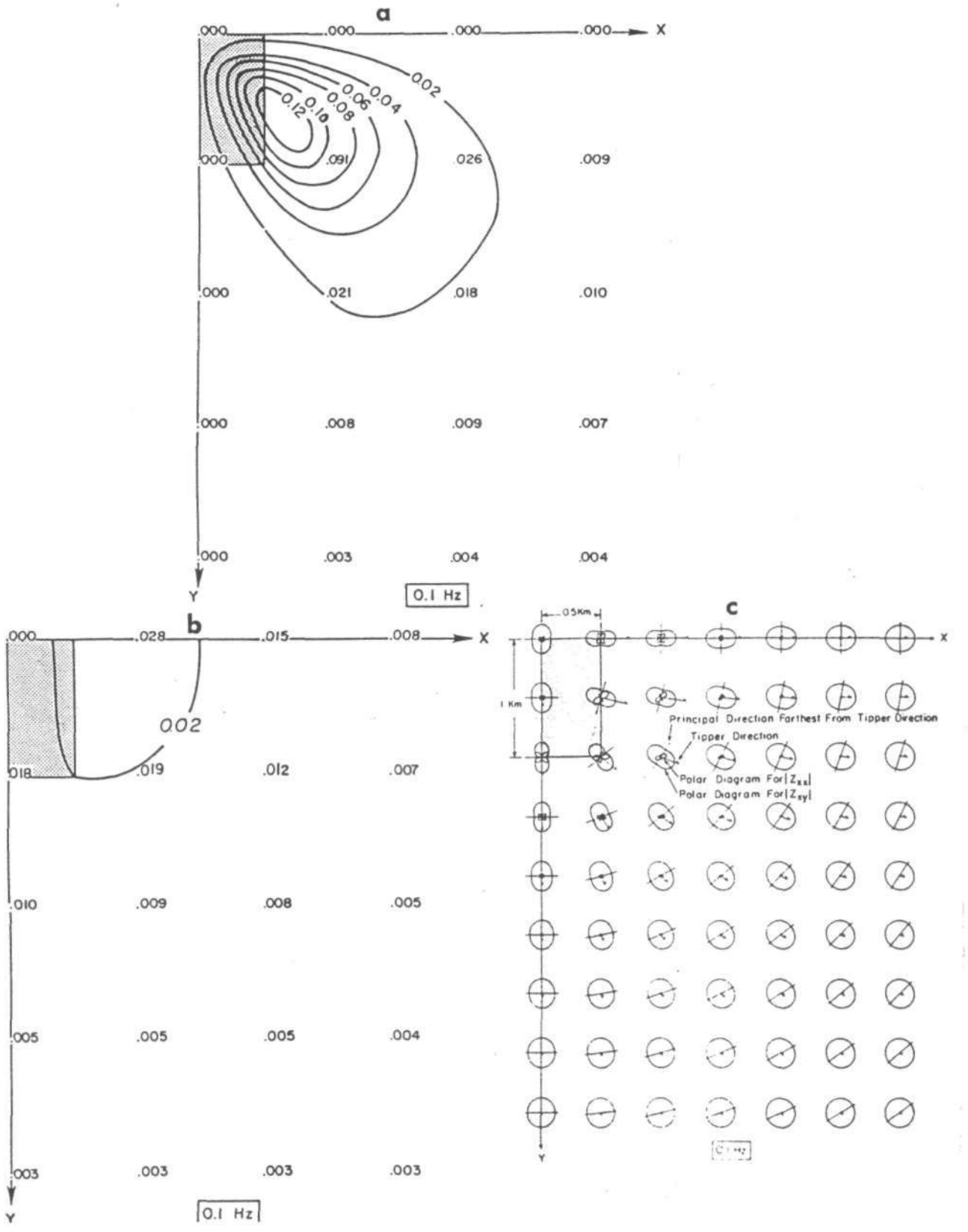


Figure 26. a)Skew, b) Tipper magnitude and c) Tipper azimuth in a quadrant from Ting and Hohmann (1981).

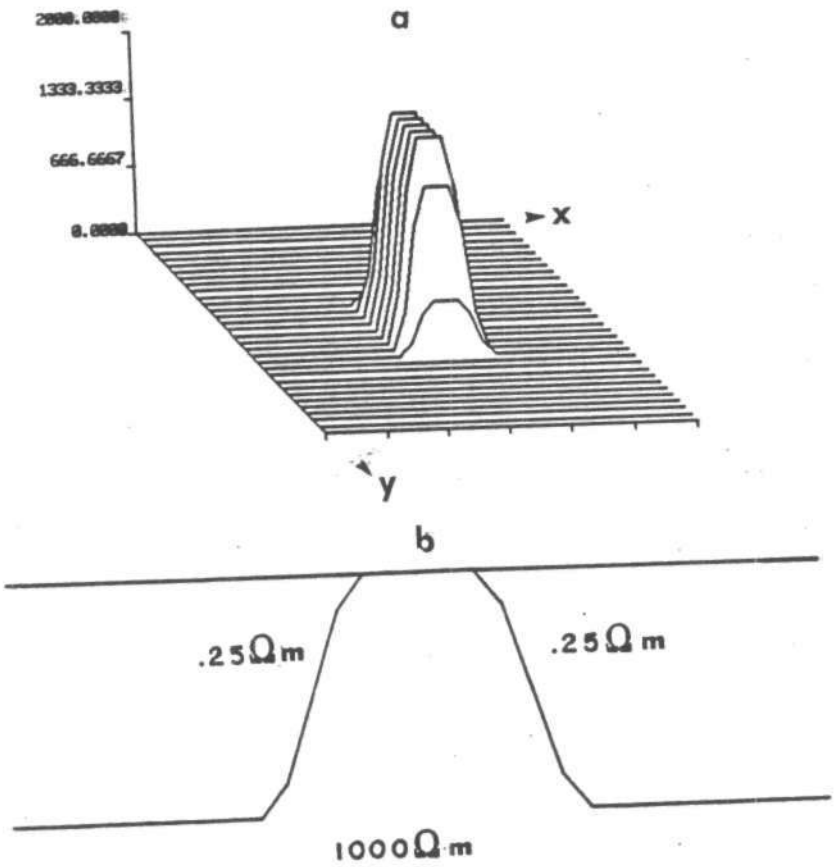


Figure 27. a) Topography of the non-planar interface for model B (vertical scale is in meters and the horizontal dimension is 90 by 90 Km).
b) A cross-section of the model along x-axis.

the components of the electric and magnetic fields. All components of the magnetic and electric fields show a three dimensionality effect. In Figure 30 the profiles of the normalized amplitudes of the y-component of the magnetic field and the x-component of the electric field through the center of the inhomogeneity parallel to y-axis are plotted. The amplitudes are normalized by the values at the extreme corner of the observation plane. These profiles compare reasonably with those of Hibbs and Jones (1977) for a similar model (Figure 31). (Note that Hibbs and Jones, 1977 model is 6 Km wide whereas the model considered here is 22 Km along the y-axis). For both the z-components of the magnetic and electric fields, there is 180 degrees phase change as one goes across the inhomogeneity (Figures 31 and 32). The profile of the z-component of the magnetic field is along the y-axis and that of the electric field is along the x-axis through the center of the inhomogeneity.

4.3.2 Apparent Resistivities and other Parameters for Model B.

The apparent resistivities at Z = 0, skew, tipper magnitude and tipper azimuth are computed for model B as explained for model A above. Although Lines and Jones (1973a and b), and Hibbs and Jones (1977) used a very similar model to calculate the the magnetic and electric fields at the model sea surface, they did not calculate the

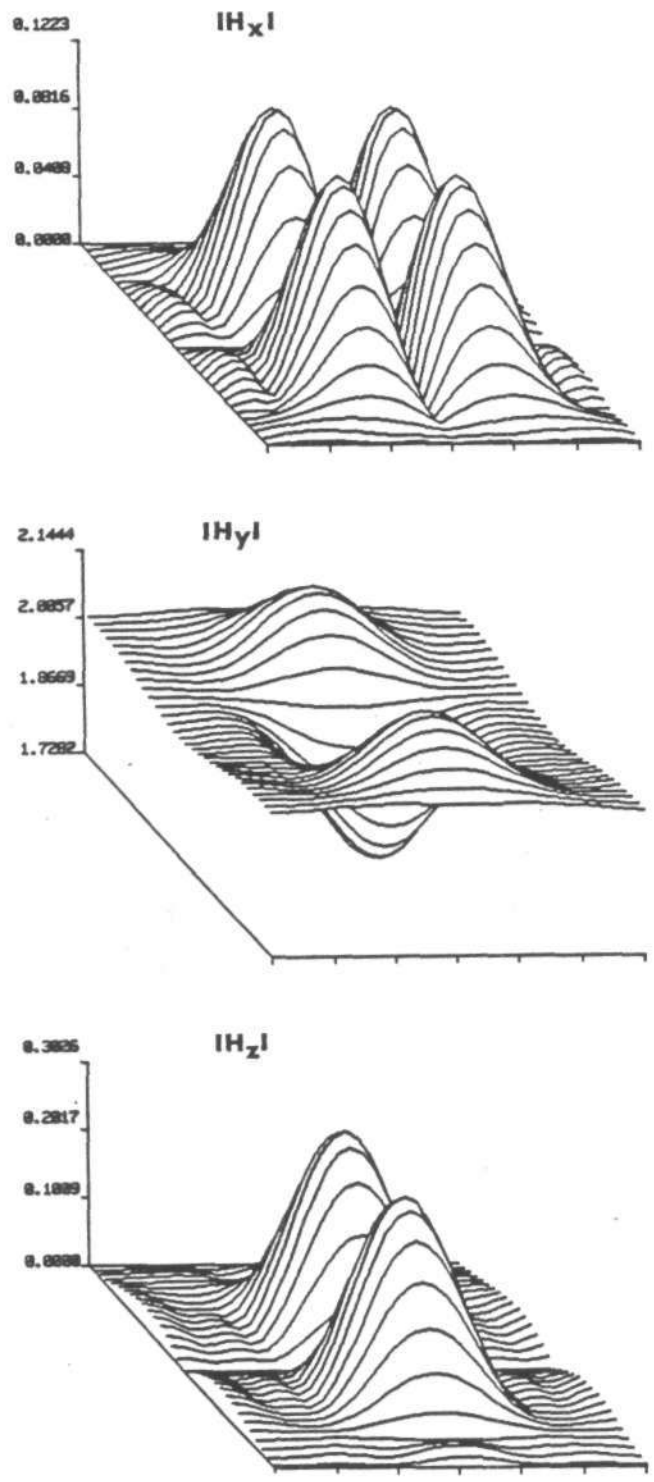


Figure 28. Amplitudes of the magnetic field components at Z=0 for model B.

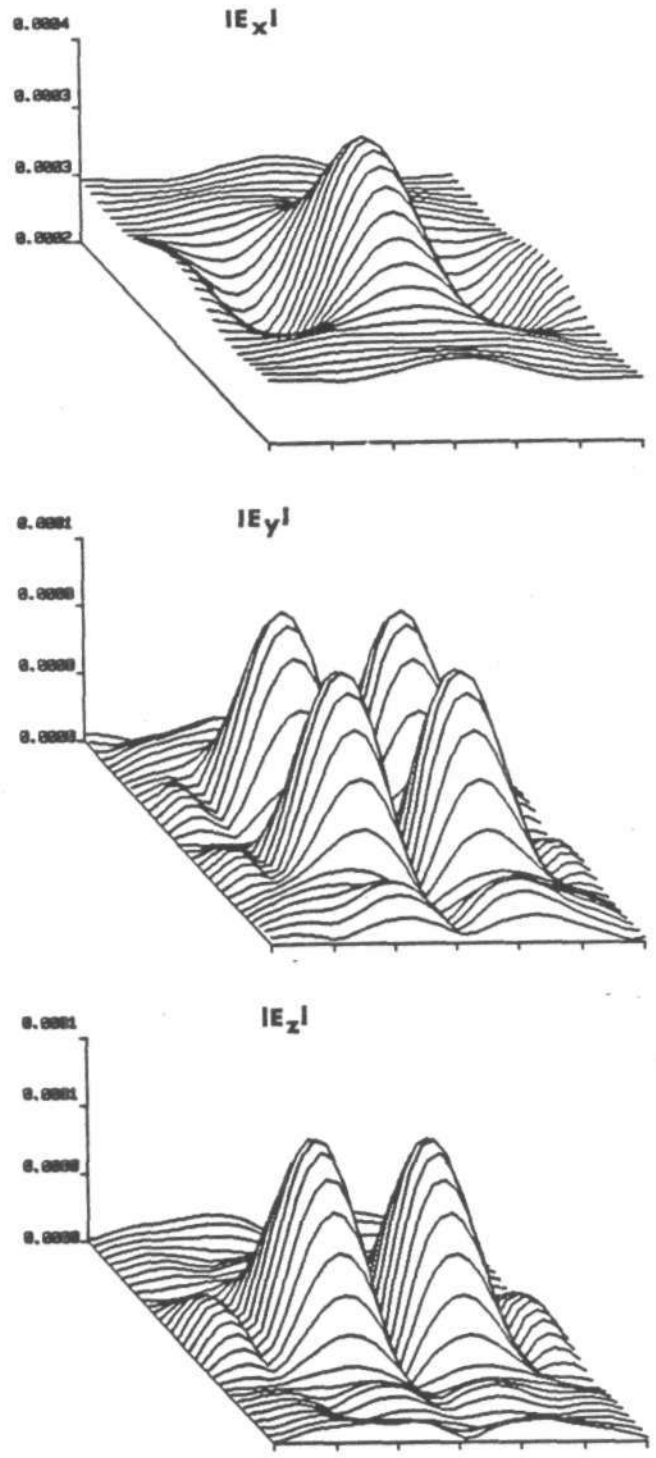


Figure 29. Amplitudes of the electric field components at Z=0 for model B.

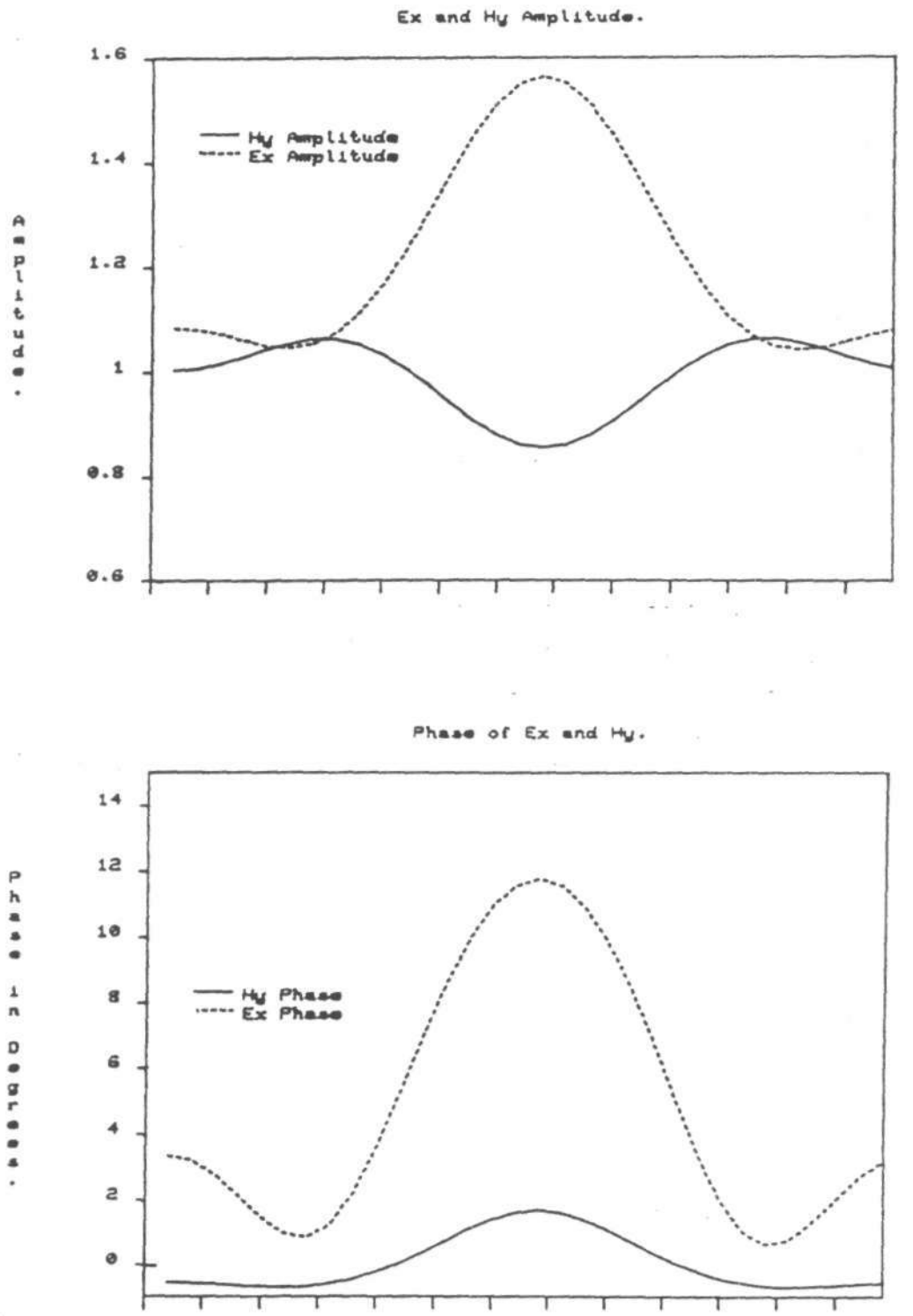


Figure 30. Profiles of the normalized amplitudes and phase angles of the x-component of the electric field and y-component of the magnetic field at Z=0 along y-axis through the center of the inhomogeneity.

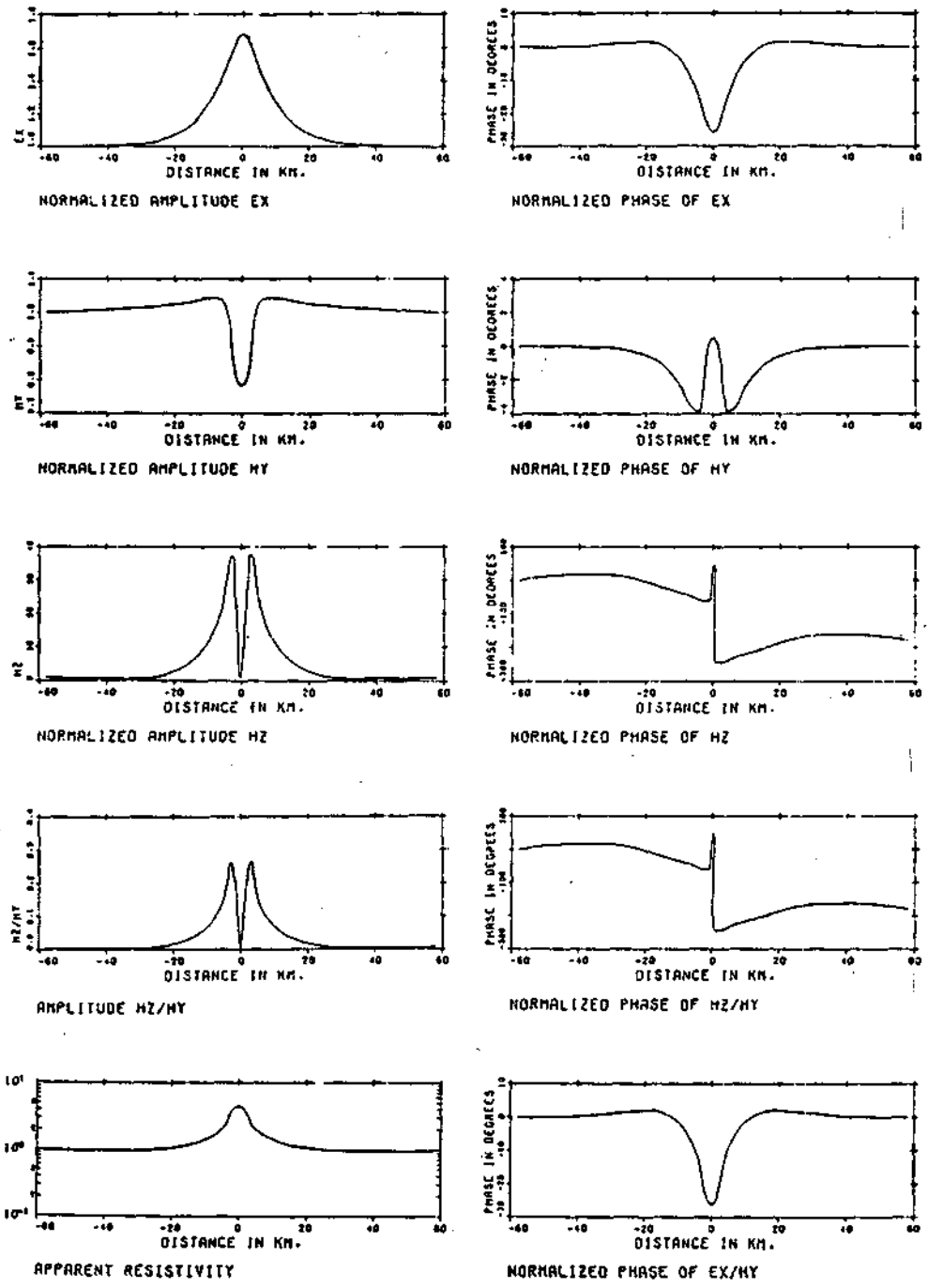


Figure 31. Amplitudes of Ex, Hy, Hz, Hz Hy and a profiles with normalized phases through the center of the inhomogeneity, from Hibbs and Jones, 1977.

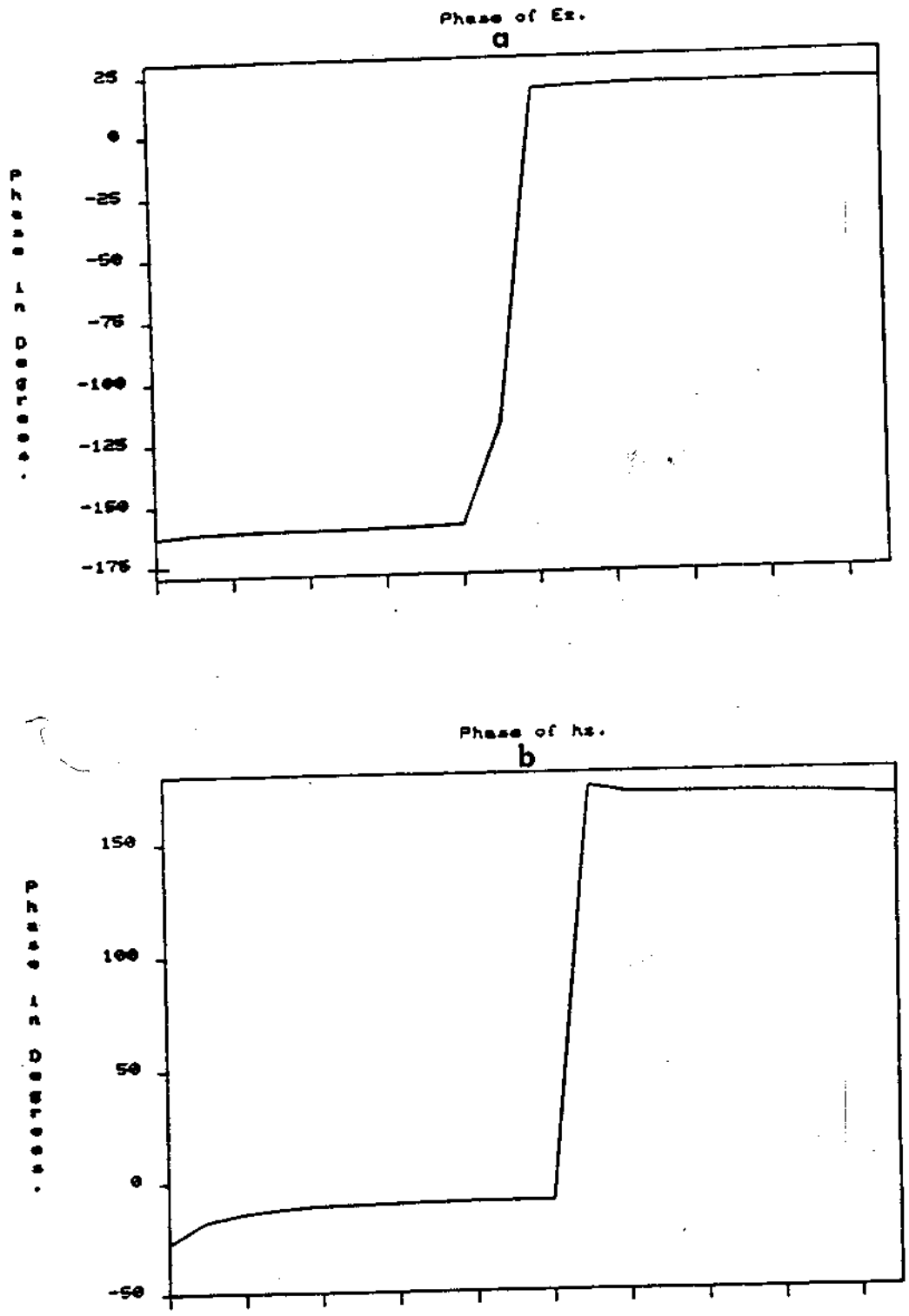


Figure 32. a) Phase angle of the z-component of the electric field along x-axis
b) Phase angle of the z-component of the magnetic field along y-axis.

apparent resistivities. A profile of the apparent resistivity calculated by Hibbs and Jones for their model compares reasonably with a profile through the center of the ρxy plot along y-axis.

Figures 33 and 34 show the plots for the apparent resistivities, skew, tipper magnitude and tipper azimuth. The tipper magnitude is higher than zero just above the inhomogeneity and the tipper azimuth does not show two-dimensionality. Although the results from other numerical techniques cannot be directly duplicated by the Rayleigh-FFT technique, due to the fact that it cannot adequately model sharp corners, the results obtained from using this technique compare well in a gross sense with those from integral equation and finite difference techniques. In the following chapter, Rayleigh-FFT technique will be used for studying an interpretational approach of MT responses in the vicinity of 3D inhomogeneities.

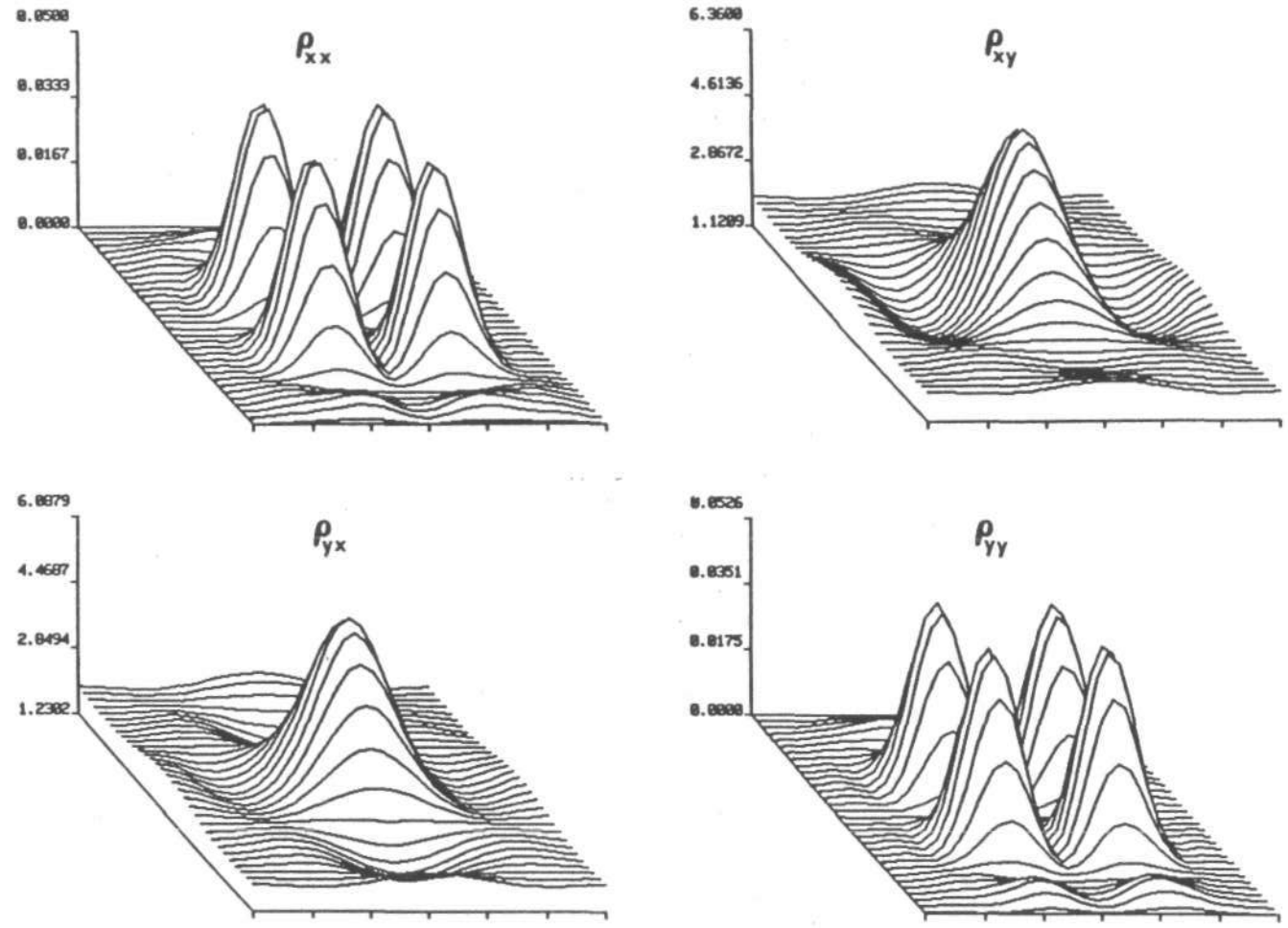


Figure 33. Apparent resistivities for model B at 0.001 Hz.

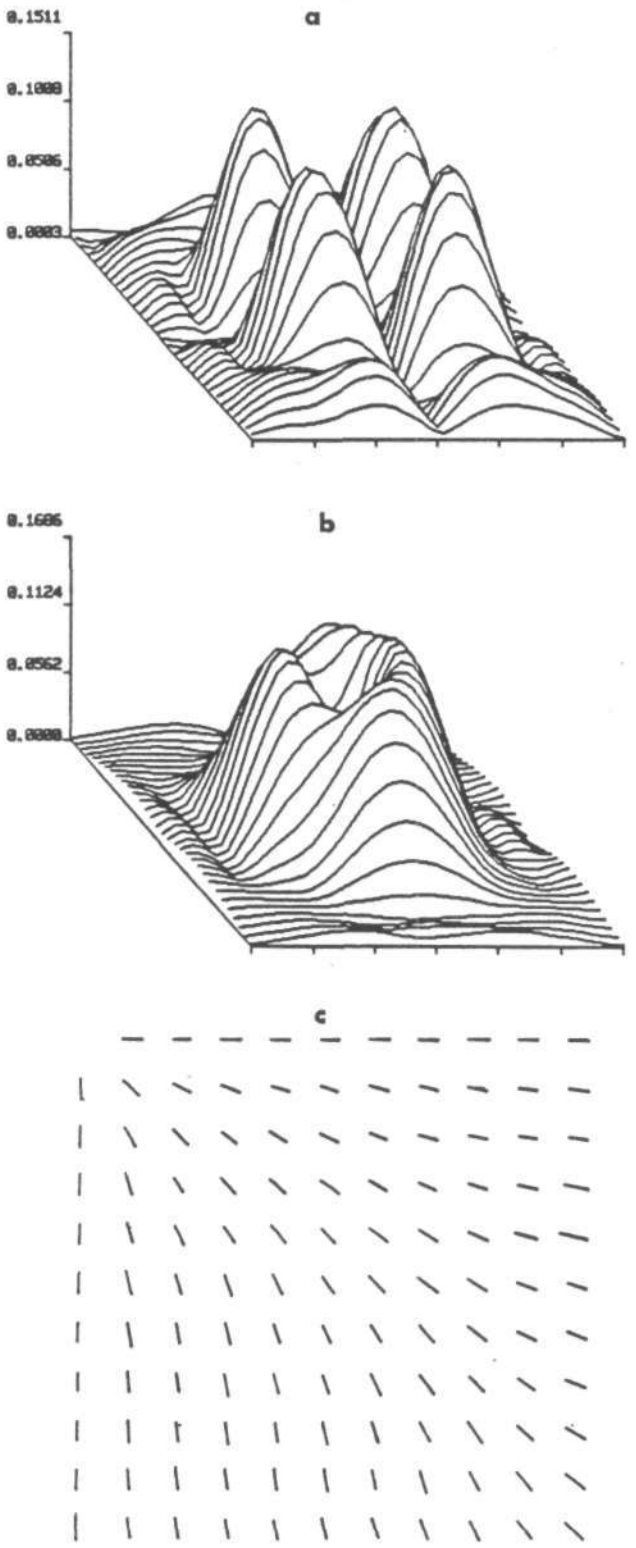


Figure 34. a) Skew, b) Tipper magnitude, and c) Tipper azimuth in the 4th quadrant for model B at 0.001 Hz.

CHAPTER 5

INTERPRETATION OF MAGNETOTELLURIC RESPONSES

In geophysical interpretation, the observed fields are analysed to obtain physical parameters which characterise subsurface features. In the case of MT, the magnetic and electric field components measured at the earth's surface are processed to obtain values of apparent resistivity, skew, tipper and so on. The common practice is to deduce at one dimensional geoelectric cross-sections for each station point, which subsequently grouped to from a two dimensional cross-section (Vozoff, 1972; Stanley et al.,1977; Jiracek et al.,1979; Hermance and Pedersen, 1980; and many others). More rarely, two dimensional TE and TM interpretations are made (e.g. Sandberg and Hohmann, 1982). Wannamaker et al., 1982 showed that although the 2D TM interpretation may approximate that of a 3D inhomogeneity for some frequencies, most 1D and 2D interpretations can be erroneous in the presence of 3D inhomogeneities. This is due to distortions of the apparent resistivity near 3D inhomogeneities due to current gathering (distortions in current flow patterns figure 2). It is important to have an MT interpretation method that is

not "biased to give erroneously shallow depths to layer interfaces and erroneously low (or high) values of layer resistivities" (Wannamaker et al.,1982) due to the effect of current gathering. As a first attempt towards understanding MT responses from 3D inhomogeneities, some models relevant to current field problems in exploration geophysics have been investigated.

The first study calculates the MT response for a buried 3D conductive inhomogeneity at different frequencies. The model is composed of a 5 Ohm-m inhomogeneity buried 2 Km in a homogeneous half-space of 100 Ohm-m. The four apparent resistivity values, skew and tipper magnitudes were calculated for frequencies of 10.0, 1.0, 0.1 and 0.01 Hz (Figures 35 and 36). Since ρxx and ρyy, and ρxy and ρyx are similar, because the inhomogeneity is symmetric, only ρxx and ρxy plots are shown (note the changes in scales). In the case of the incident waves of frequency of 10 Hz, the values of ρxx, skew and tipper are very small. At this frequency, the inhomogeneity is buried more than one skin depth (1.6 Km) away, so its effect is weakly registered. Instead of observing low resistivity values directly above the inhomogeneity for ρxy, we have high values (a situation similar to the layered earth case for high frequencies). As the frequency is lowered, the values of ρxx and skew become more pronounced, and the overshoot over the ends of the body for ρxy increases. In the case of tipper magnitude, for the frequency of 10 Hz,

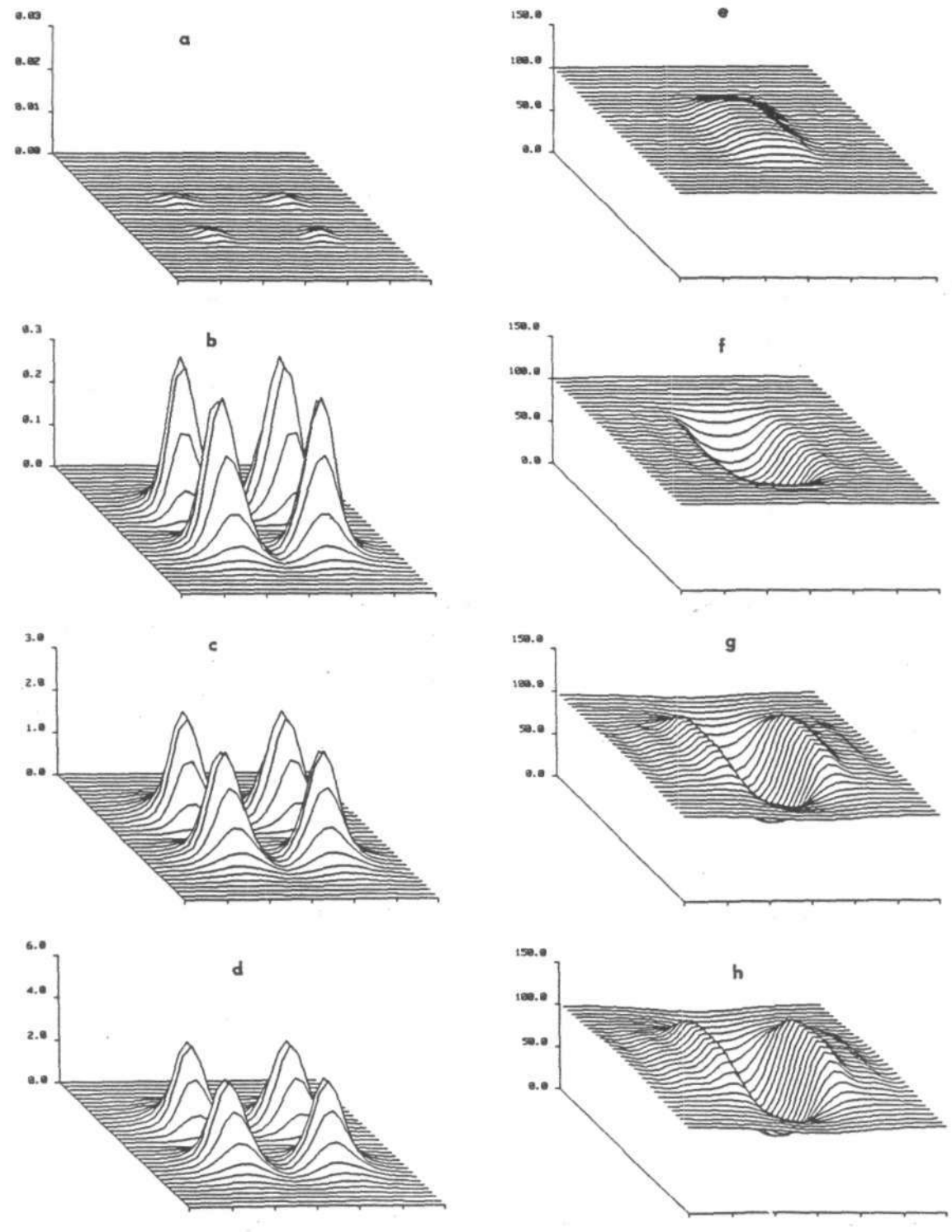


Figure 35. Apparent resistivities for a 5 Ohm-m inhomogeneity buried at a 2Km depth 100 Ohm-m half-space. ρxx at a) 10, b) 1.0, c) 0.1 and d) 0.01 Hz. ρxy at e) 10, f) 1.0, g) 0.1 and h) 0.01 Hz. (Note the change in scale for oxx).

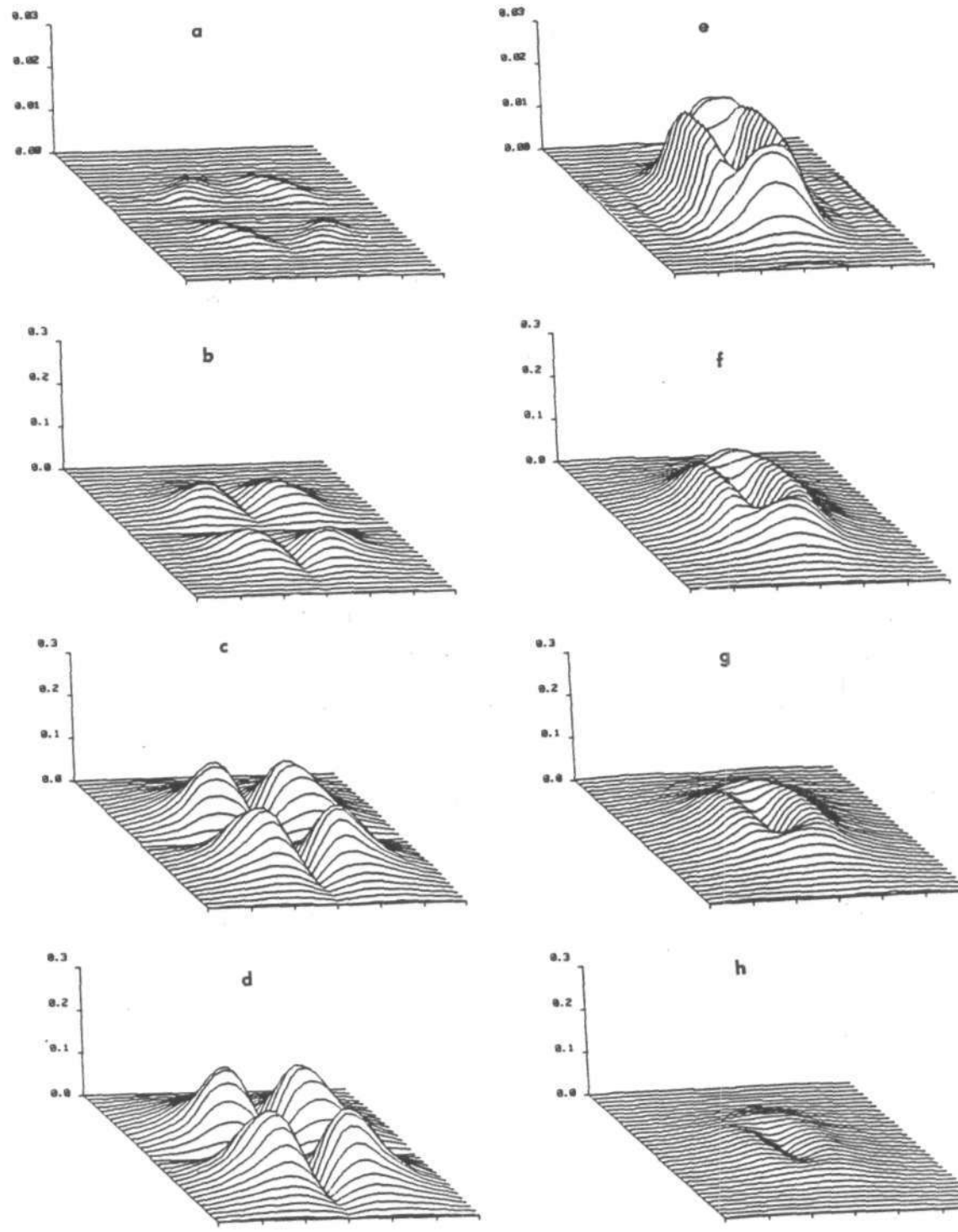


Figure 36. Skew and Tipper magnitude for a 5 Ohm-m inhomogeneity buried at 2 Km depth in 100 Ohm-m half-space.
Skew at a) 10., b) 1.0, c) 0.1 and d) 0.01 Hz.
Tipper magnitude at e) 10, f) 1.0, g) .1 and h) .01 Hz.

the values are very low (barely over 0.02) as the frequency is decreased to 1 Hz (target depth to skin depth ratio is 0.4), the values reach their maximum of about 0.15 and they become progressively smaller as the frequency of the incident waves decrease. Difference between maximum and minimum values of ρxy also increase with decreasing frequency (18 to 110 Ohm-m) for the frequencies of 10 to 0.01 Hz. From this type of 3D 'depth sounding', and analysis, estimates can be made of the resistivity of the inhomogeneity relative to the host rock, its lateral extent and its approximate depth. A combined study of skew, ρxy, ρxx and tipper magnitudes at different frequencies will help in identifying the nature of the inhomogeneity.

Another useful 3D model is a magma chamber. Interpretation of MT results from geothermal areas are difficult. Low resistivity values in the crust up to depths of 30 Km could be due to: a) increased ionic mobility with increased temperature, b) electronic or mineral conduction, c) partial melting, or d) alteration (Stanley et al., 1977). Assuming a magma chamber which is a low resistive body, due to partial melt at a depth of 8 Km, the resistivity of the model inhomogeneity was set at 1.0 Ohm-m, and its shape and the resistivity of the half-space was varied. The first case consists of a body 1 Km thick and 20Km by 20 Km with the sides gently sloping (Figure 37a) in a 100 Ohm-m resistive half-space. Apparent resistivity values, skew and tipper were computed (Figure

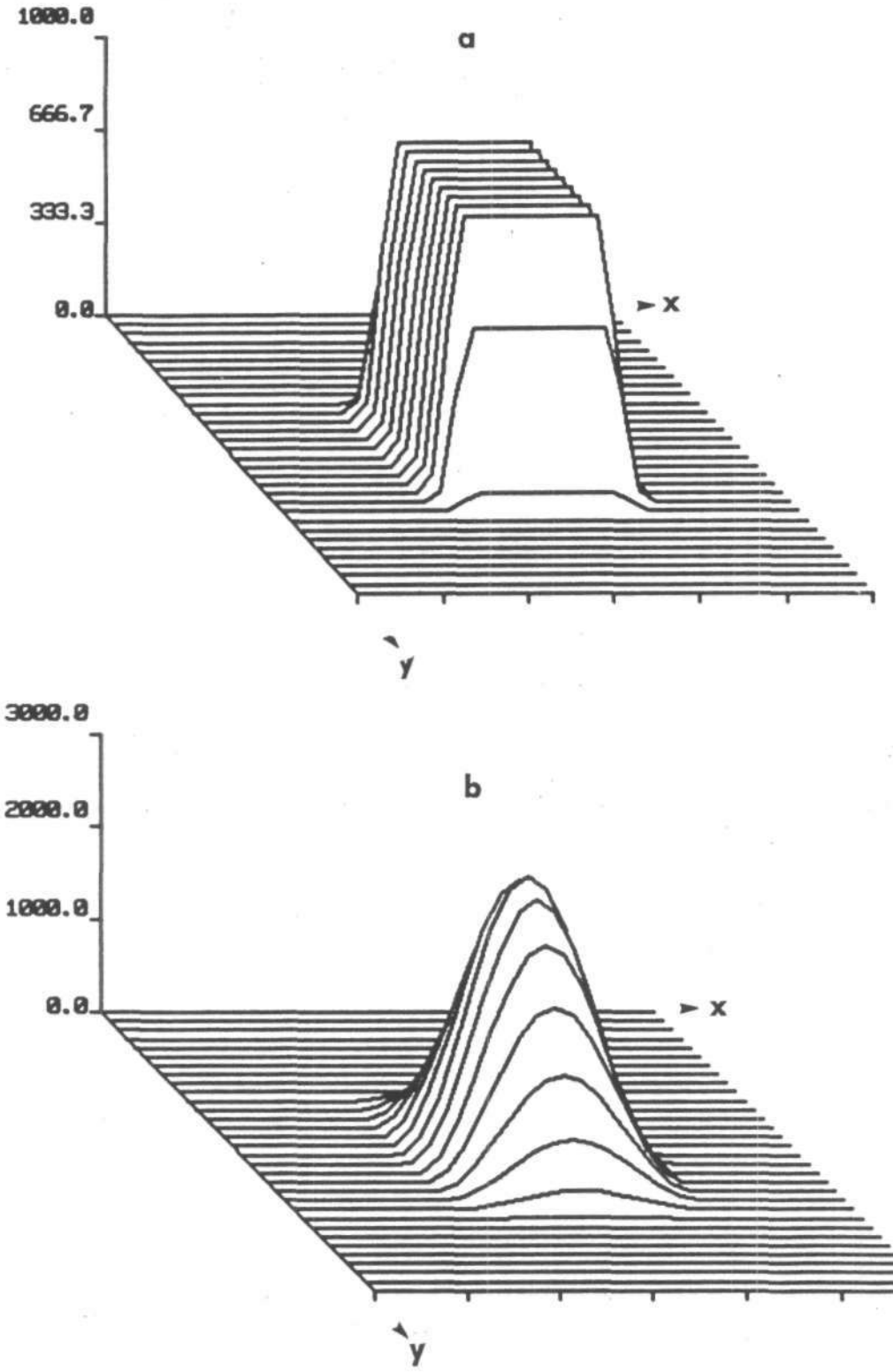


Figure 37. a) Topography of 'flat' magma.
b) Topography of dome shaped magma. (vertical scale is in meters and the horizontal dimension is 80 by 80 Km).

38) for frequencies of 0.01 and 0.001 Hz. with repitition distances of 80 Km (this model will be refered to as magma 1). The other models investigated consist of a 1 Ohm-m dome, 3 Km high and 18 Km wide at the base with its top 8 Km below the model earth's surface (Figure 37b). The apparent resistivities, skew and tipper magnitudes for two frequencies (0.01 and 0.001 Hz) for the body buried in 100 Ohm-m (magma 2) and 1000 Ohm-m (magma 3) half-space, with a 20 Ohm-m layer above the inhomogeneity and 100 Ohm-m half-space below it (magma 4) were computed (Figures 38, 39, 40 and 41). (Magma 4 was chosen to simulate the case when there is an itermediate resistivity layer above a magma chamber). For the four cases, skew increased with decreasing frequency, tipper magnitudes decreased, and the apparent resistivity values increased. The anomalies produced by the inhomogeneity buried in different resistive half-spaces remain very similar, although the skew and tipper values are higher for the more resistive half-space.

The difference between the maximum and minimum values of ρxy for magma 1 is greater than that of magma 2 for the same frequency (140 Ohm-m for magma 1 and 60 Ohm-m for magma 2 for the 0.001 Hz frequency) and also the maximum values of ρxx and skew are higher for magma 1. This might be due to the fact that magma 1 has more lateral extent than magma 2 at the same depth. For the overshoot in the values of ρxy at the sides of the inhomogeneity to be clearly observed, the measurements have to be obtained up

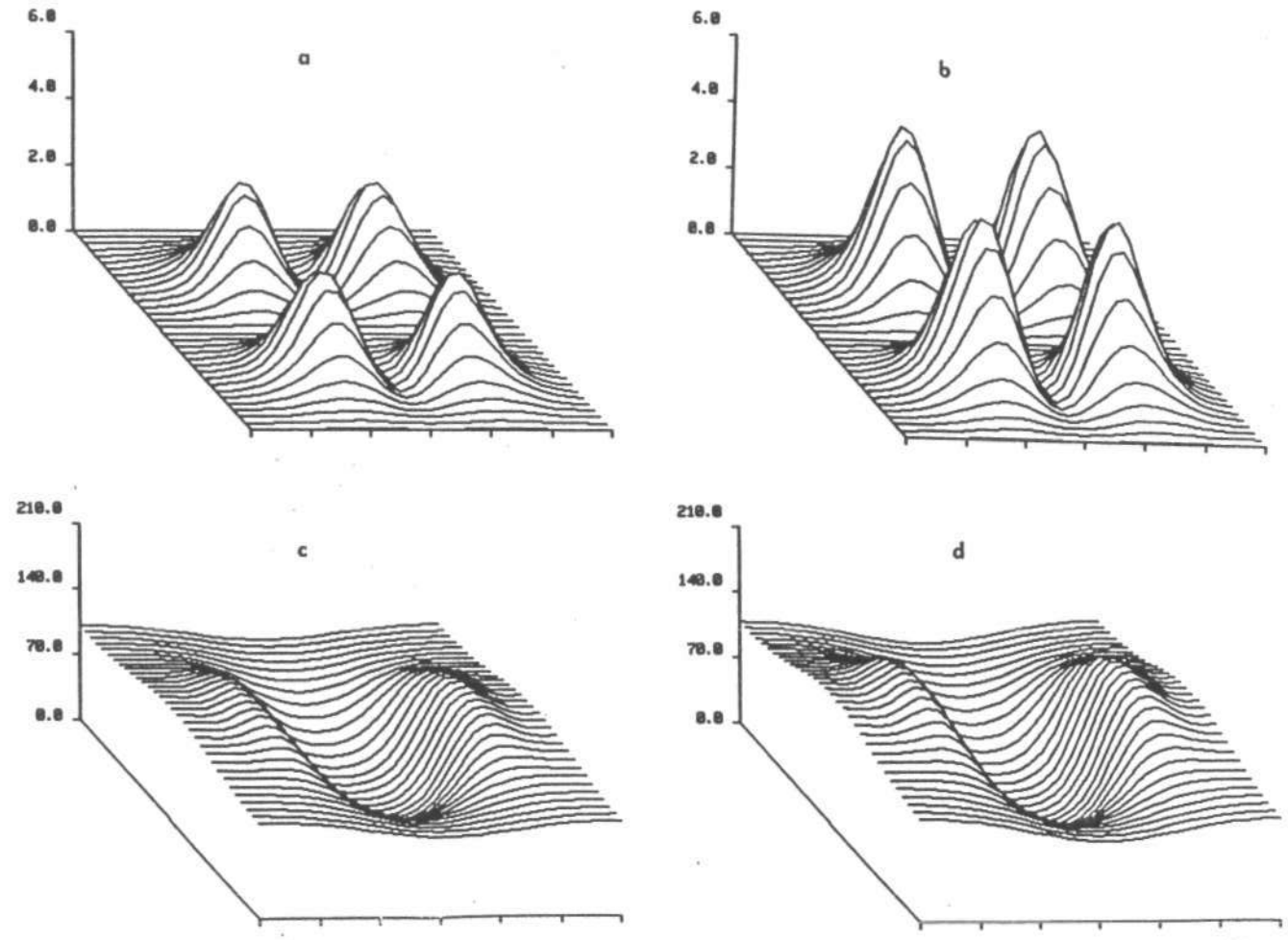


Figure 38. ρxx for magma 1 at a) 0.01 and b) 0.001 Hz.
ρxy for magma 1 at c) 0.01 and d) 0.001 Hz.

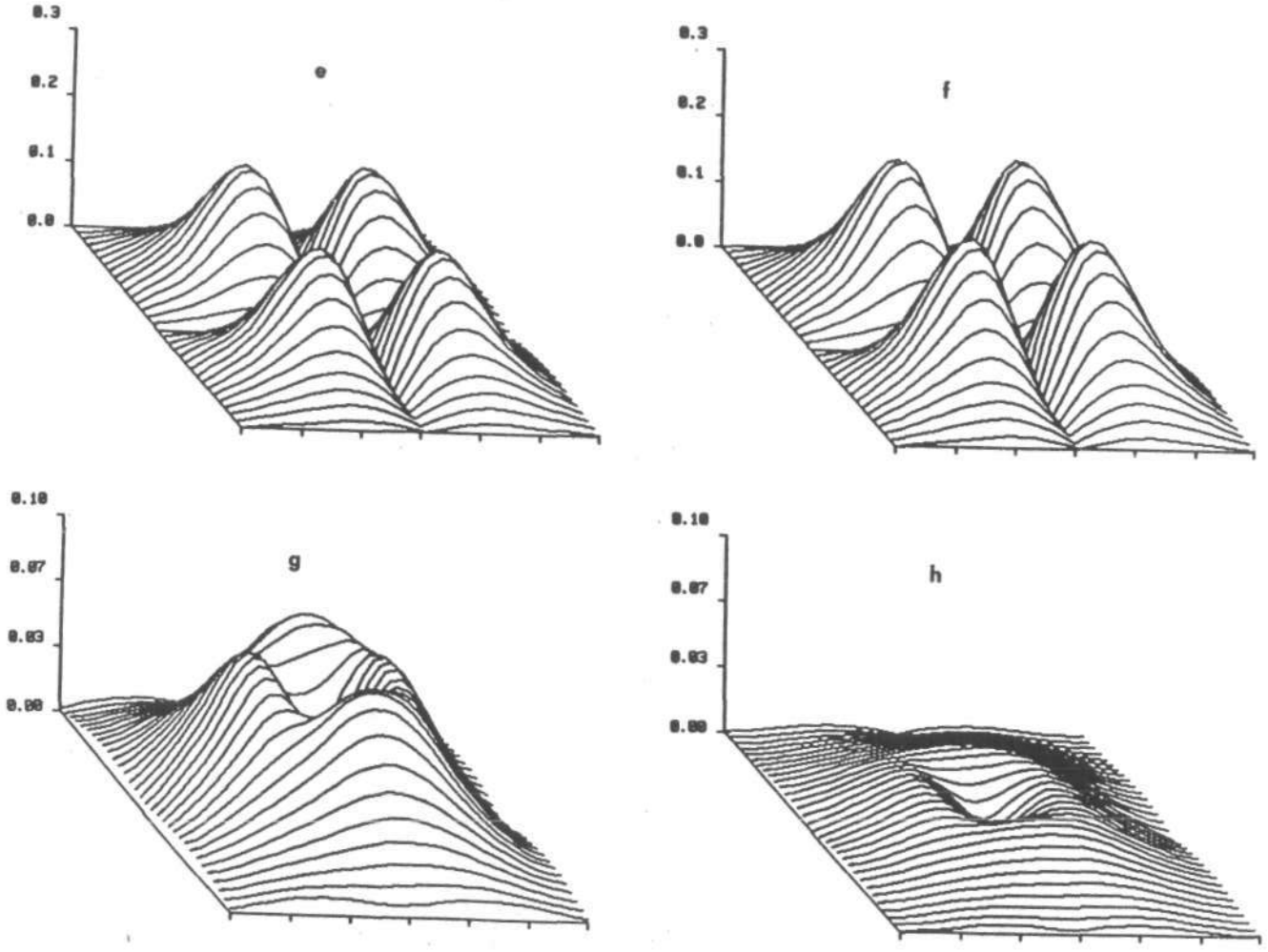


Figure 38. Skew for magma 1 at e) .01 and f) .001Hz.
Tipper for magma 1 at g) .01 and h) .001 Hz.

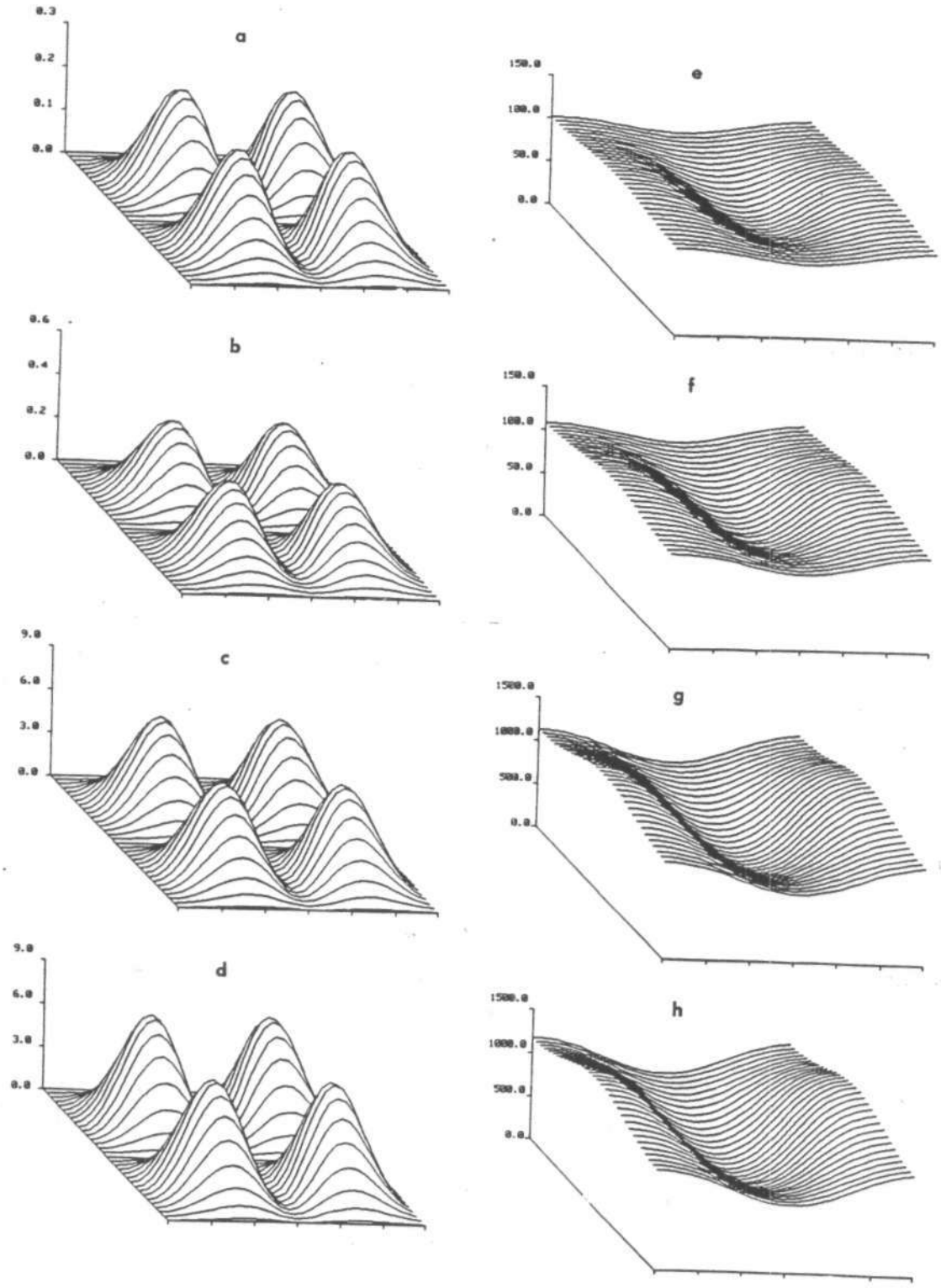


Figure 39. ρxx for magma 2 at a) 0.01 and b) 0.001 Hz.
ρxx for magma 3 at c) 0.01 and d) 0.001 Hz.
ρxy for magma 2 at e) 0.01 and f) 0.001 Hz.
ρxy for magma 3 at g) 0.01 and h) 0.001 Hz.

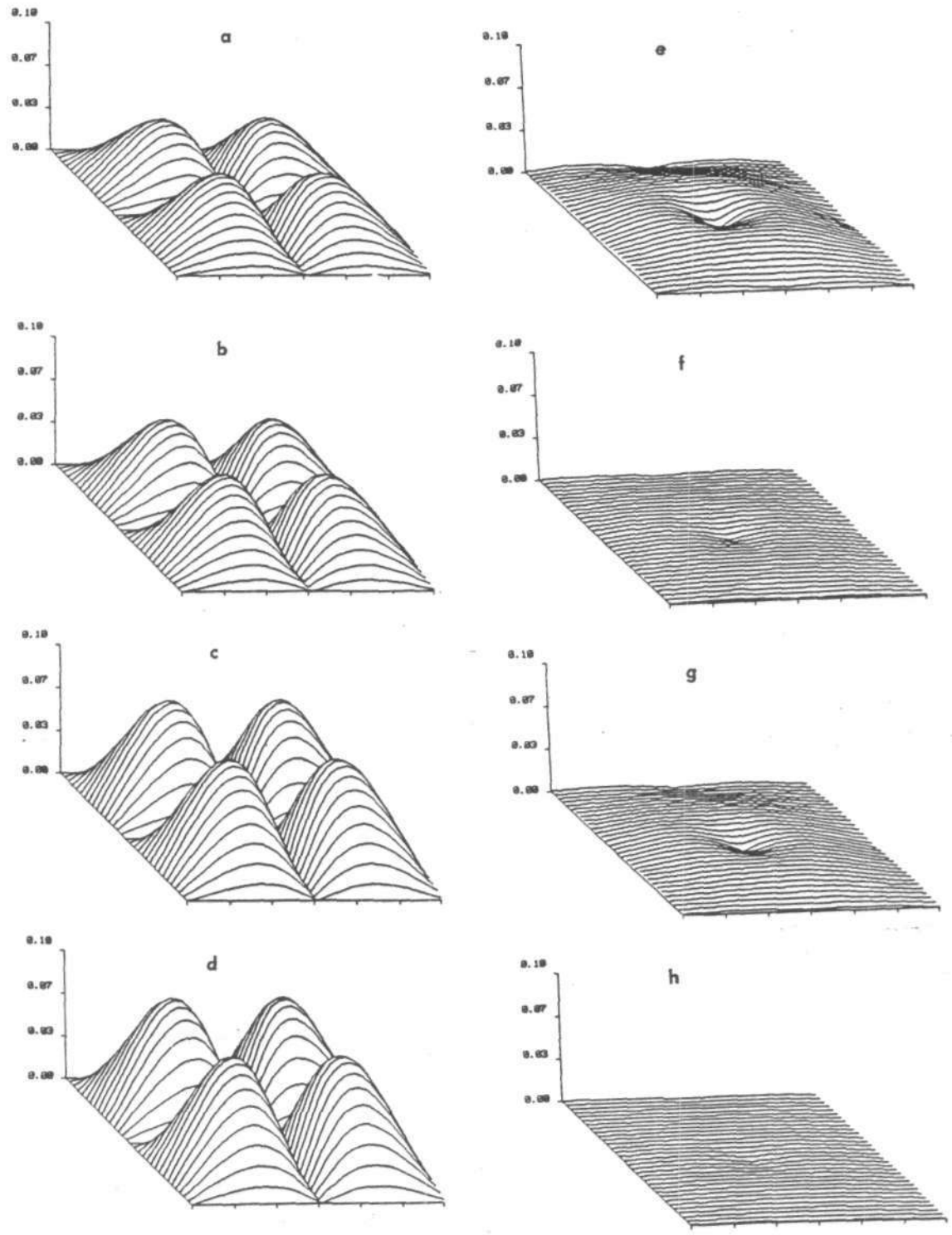


Figure 40. Skew for magma 2 at a) 0.01 and b) 0.001 Hz.
Skew for magma 3 at c) 0.01 and d) 0.001 Hz.
Tipper for magma 2 at e) .01 and f) .001 Hz.
Tipper for magma 3 at g) .01 and h) .001 Hz.

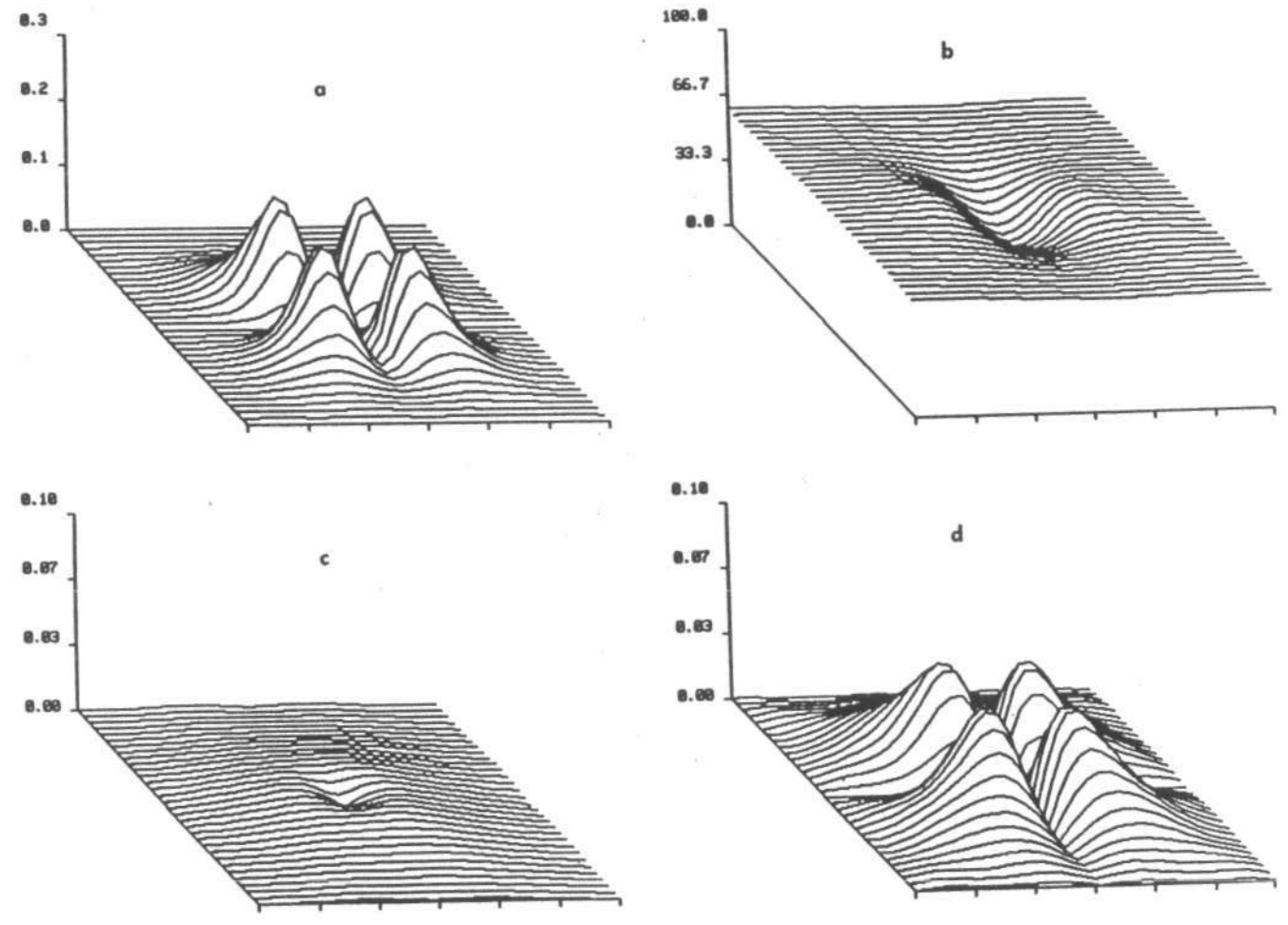


Figure 41. a) ρxx, b) ρxy, c) Tipper and d) Skew for magma 4 at 0.001 Hz.

to about one skin depth from the sides of the inhomogeneity.

As with any other conductive inhomogeneity buried in a more resistive media, a magma chamber would characteristically give lower values for the ρxy and ρyx above it, with slight overshoots by the sides of the innhomgeneity. The shape of the inhomogeneity (for the cases considered) does affect the ease of its detectability. At the frequency of 0.001 Hz, the maximum skew for magma 1 and magma 2 are 0.23 and 0.06 respectively, and the maximum values of tipper are 0.03 and 0.008. From these relatively higher values in ρxx, skew, and tipper and difference maximum and minimum ρxy for magma 1, it is easier to detect magma bodies that are flat (of the form shown in Figure 37a) than those in the form shown in Figure 37b.

For magma 4, the difference batween the maximum and minimum values of ρxy is lower (25 Ohm-m) than that of magma 2 (60 Ohm-m) for the the frequency of 0.001 Hz. The resistivity of the half-space in which the inhomogeneity is buried affects its detectability. The higher the resistivity contrast, the easier it is for the body to be detected. Usually, magma chambers have an associated low resistive zone due to raised temperature, water and alteration effects. In this case, since the resistivity contrast between the magma chamber and its immediate vicinity will be low, it will be more difficult to detect.

From the above discussion, some guide lines for 3D MT interpretation can be given. Skew, usually considered to be an effective three-dimensionality indicator, has low values (approximately 0.1) for bodies buried at depths of about half a skin depth. Skew values of 0.1 should not be ignored as is usually the practice. Although expensive, to fully understand the subsurface geology better through MT, data at different frequencies on a grid pattern must be collected. Apparent resistivities at different frequencies should be computed plus skew and tipper magnitudes. A rough estimate of the lateral extents of the inhomogeneity could be determined from the offshoots (or undershoots) in the values of ρxy and ρyx. 3D coverage will help to eliminate interpreting inhomogeneities to the sides of profiles as if they were directly below the surface. When skin depth is greater than the depth of burial for a conductive inhomogeneity, there is a depression in the values of ρxy and ρyx compared to that of the half-space over the body, and there are overshoots to the sides of the body. The reverse is true for a resistive inhomogeneity in a more conductive half-space (Chapter 4).

The approach to MT iterpretation has to be changed in view of the fact that 3D inhomogeneities affect the apparent resistivity values. As the frequency is reduced, it is usually assumed that the response observed is due to deeper buried inhomogeneity, but as has been shown in this study, and that of Wannamaker et al., 1982, the values of

ρxy and ρyx near a 3D inhomogeneity are enhanced for the frequencies investigated.

Another problem investigated was to determine the circumstances under which a 3D model could be approximated by a 2D model. In this case, a resistive slab of 1000 Ohm-m and 1 Km in height just outcrops in a 0.25 Ohm-m homogeneous half-space. The upper surface of the inhomogeneity coincides with that of the half-space. The frequency of the incident waves is 0.001 Hz. Two cases were considered: in the first case, the ratio of the length to breadth of the inhomogeneity (aspect ratio) is 10, and in second case it is 2. Apparent resistivity, tipper magnitude and azimuth for the aspect ratio of 10 (model D) and 2 (model E) were computed. Figures 42 through 47 show plots of the apparent resistivities, tipper magnitude and azimuth for the two cases. All the plots show values of ρxx, and ρyy higher than zero near the corners of the inhomogeneities. The tipper magnitude and the undershoot in the values of ρxy and ρyx are more pronounced near the edges. In the case of the tipper azimuth, the directions did not change as rapidly near the center of the inhomogeneity for an aspect ratio of 10 as it does when the ratio is 2.

Since the pattern of the fields and consequently the apparent resistivity values that are observed depend on the current flow pattern in the vicinity of an inhomogeneity, and since the current flow patterns are most distorted near

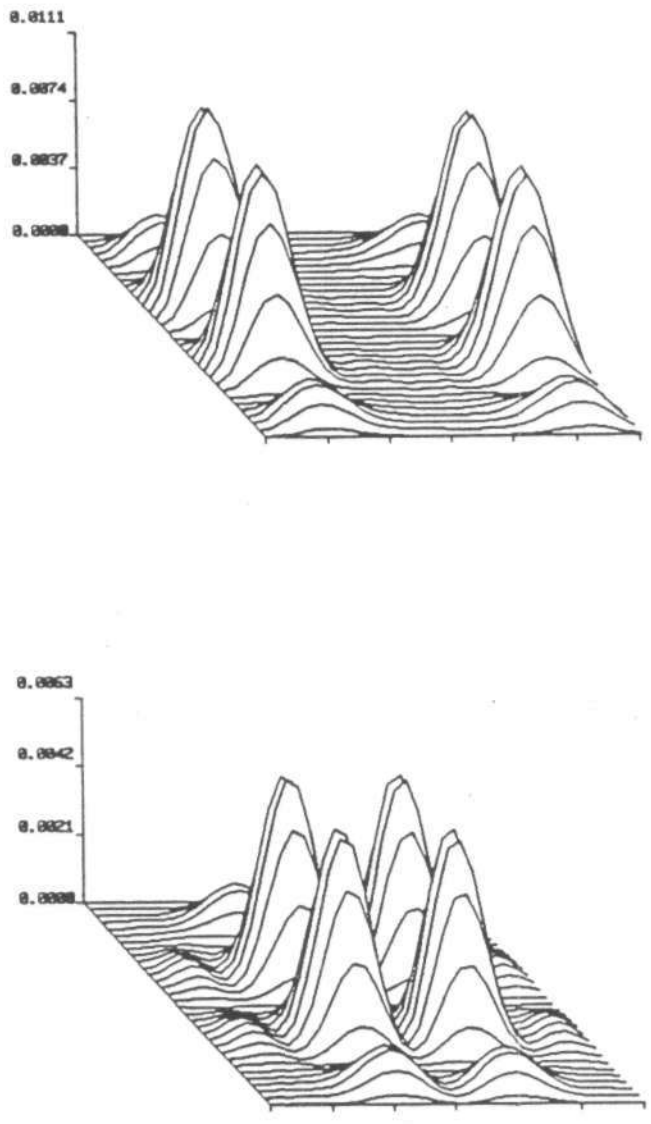
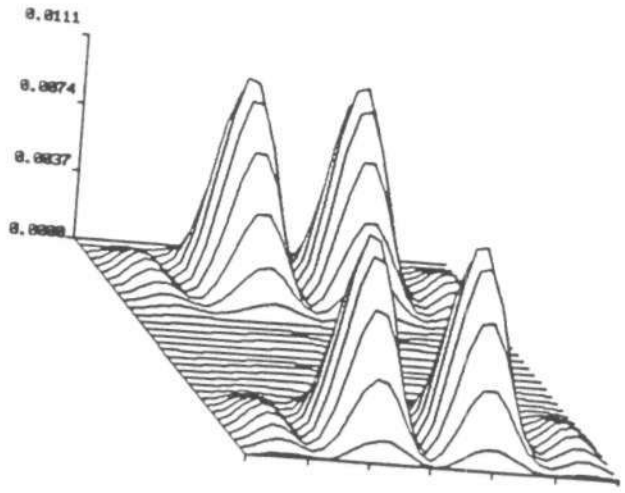


Figure 42. Apparent resistivity (ρxx) for models D and E.



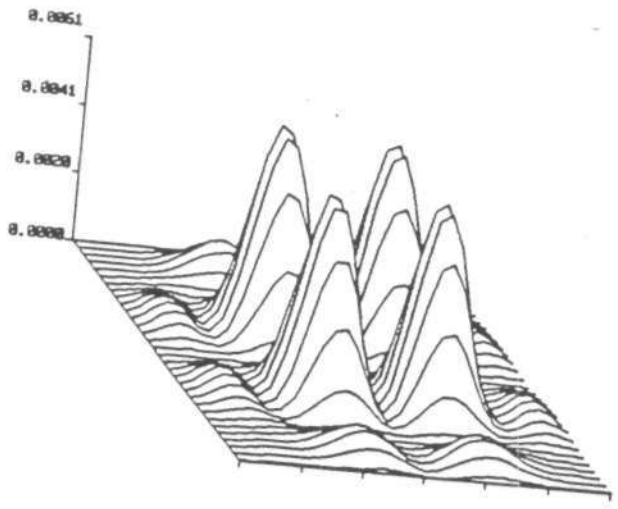


Figure 43. Apparent resistivity (ρ_{yy}) for models D and E.

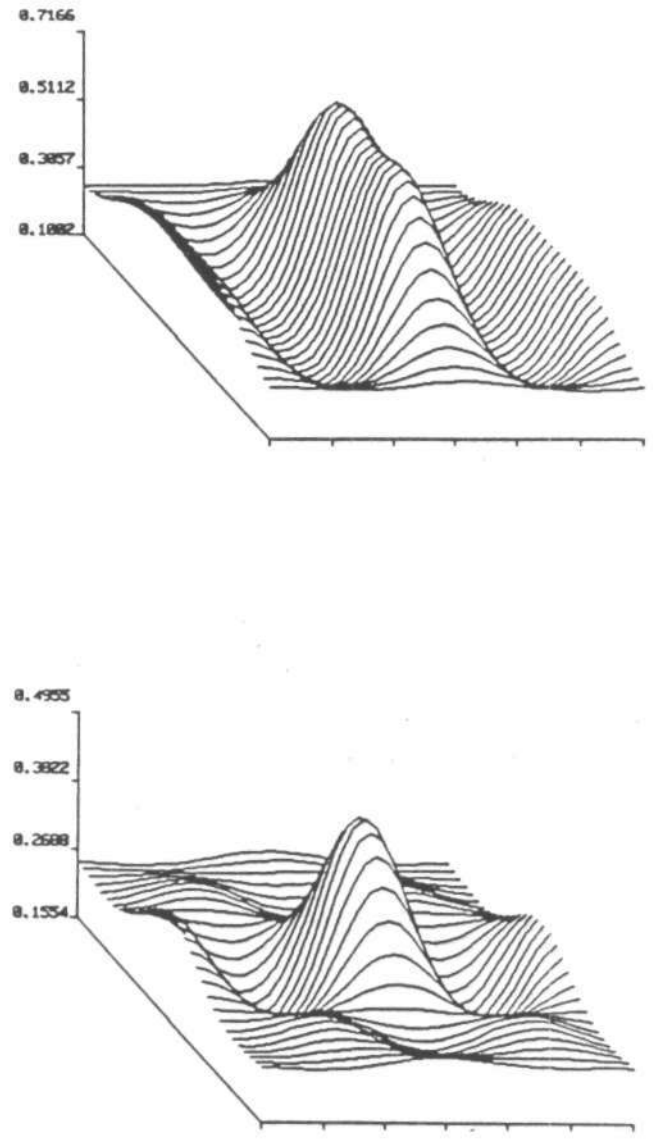


Figure 44. Apparent resistivity (ρxy) for models D and E.

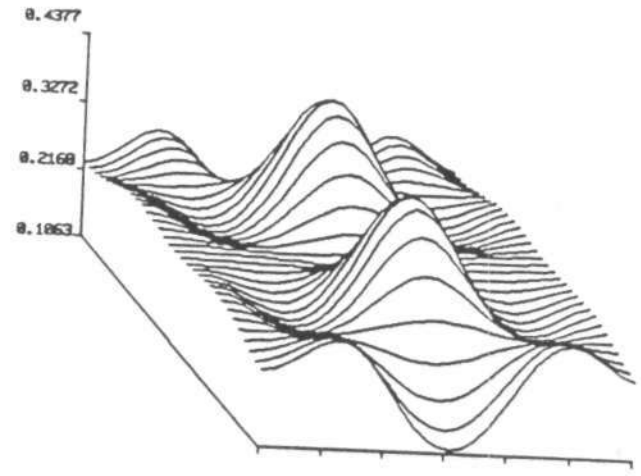
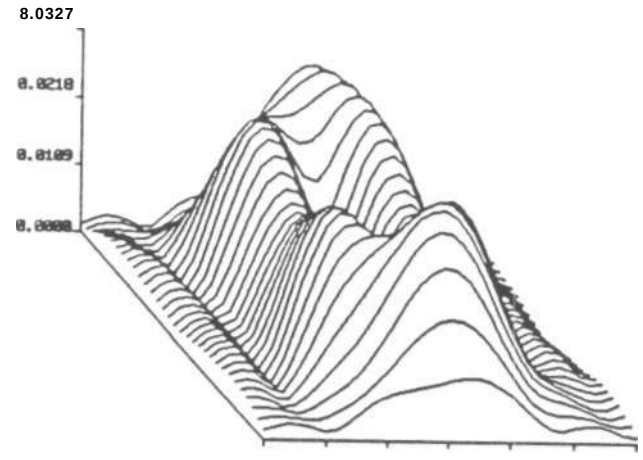


Figure 45. Apparent resistivity (ρ_{yx}) for models D and E.



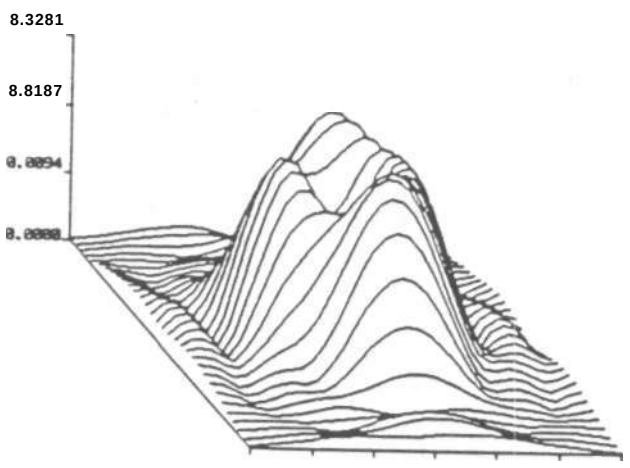


Figure 46. Tipper magnitude for models D and E,

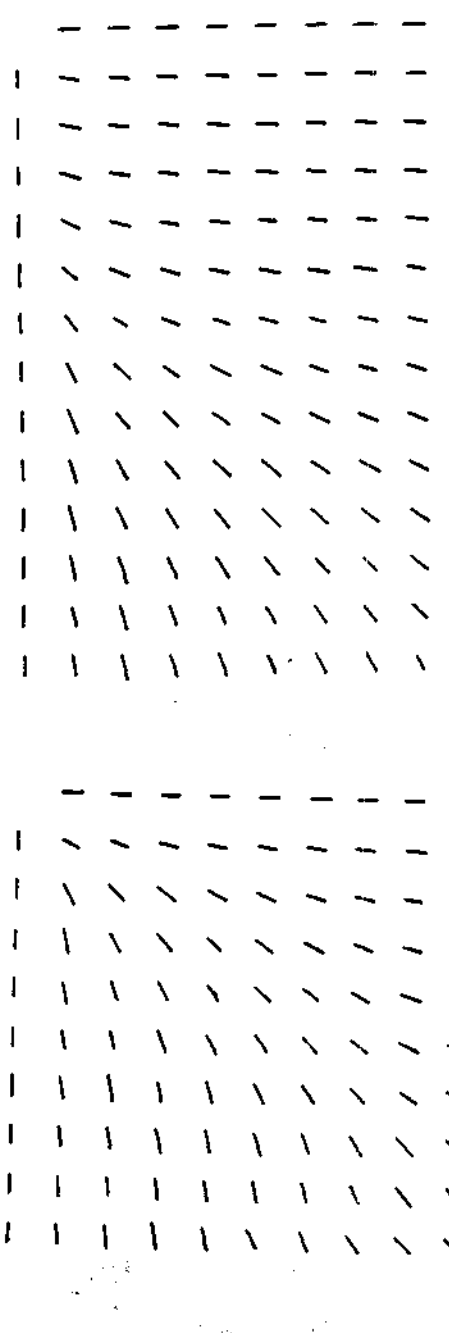


Figure 47. Tipper azimuth for models D and E.

the corners and edges of the inhomogeneity, for a 3D body to be approximated by 2D, the corners have to be reasonably far apart. How far apart the corners have to be will depend on the skin depths of the half space and the inhomogeneity at the frequencies of interest. This relationship is yet to be thoroughly investigated.

CHAPTER 6

DISCUSSIONS AND CONCLUSIONS

The MT method is being extensively applied to determine the electrical characteristics of the earth. Several groups utilise MT for oil exploration to analyse the geometry of sedimentary basins and for geothermal exploration. In a recent review paper on the progress of electrical, electromagnetic and magnetotelluric methods, Ward (1980) noted that "while the tensor MT method recognises anisotropy and or two-dimensionality in earth structure, its routine application have been in terms of 1D, i.e., plane, horizontally layered earths. That this approach is erroneous in general application has been clearly demonstrated by Wannamaker, in fact, he establishes that even a 2D model is inadequate and that a 3D model is usually required". This problem has been recognised and several attempts to formulate efficient numerical techniques for 3D modeling have been published by (Lines and Jones, 1973; Reddy et al., 1977; Jones and Vozoff, 1978; Ting and Hohmann, 1981.

Current numerical techniques (finite difference, Lines and Jones, 1973; finite element, Reddy et al., 1977; and

integral equation, Ting and Hohmann, 1981) have the disadvantages of requiring gridding and numerical differentiation. When a model has a complex geometrical shape, a large number of grid points are required. This in turn requires the solution of a large number of equations with the consequent problems of computer memory limitations and long computation times. The large grid size in practice limits current modeling techniques to 3D inhomogeneities in form of parallelipipeds buried in a homogeneous half-space. So far the models investigated have had simple geometric shapes, even then, the computer memory requirements and computation time are high. For example, it took 156 minutes to obtain the electric field components on a Univac 1108 for the Reddy et al. (1977) 3D finite element modeling technique. Other techniques have even taken longer times, for example, the integral equation technique by Wannamaker et al., 1982, took about 20 hours on a Prime 400 for an inhomogeneity buried in layered half-space. Note that they applied syymetry conditions to reduce computational effort. The other problem with the present techniques is the difficulty associated with numerical differentiation (Lee et al., 1981). When the electric (or magnetic) field has been computed, the magnetic (or electric) field must be obtained by numerical differentiation, usually based on a finite difference scheme. The reliability of the solutions is sometimes based on convergence tests. Ting and Hohmann (1981) noted

that "because convergence is affected by so many factors, we are not able to quantify accurately any general criteria among those factors to assure a certain accuracy in our results". This may also be said of other numerical techniques that rely either only on convergence or comparison of the response far away from the inhomogeneity with that of a half-space (or whatever the body might be buried in). In short, previous 3D modeling techniques lack quantifiable self consistency tests. In addition Ting and Hohmann (1981) had problems of convergence for models with shallow bodies and also high resistivity contrasts.

The Rayleigh-FFT technique was used for the 3D MT modeling in this study. Although Jiracek (1973) derived equations for 3D MT response from two dimensionally varying interfaces, he obtained solutions for a one dimensionally varying interfaces only, in a way similar to Aki and Larner (1970). In this study, the expressions for the electric and the magnetic field components were derived directly from Maxwell's equations by applying Fourier transforms. Spectral amplitudes of the field components were obtained by solving the system of equations that result after the application of boundary condition. The equations were Fast Fourier Transformed in order to simplify their solution. The calculated field components were used to compute the apparent resistivities, skew, tipper magnitude, and azimuth. Truncation of the infinite summations affects the reliability of the solution. The

higher the number of scatteringg orders included, the more reliable the solution (Table 1). Also the gentler the slope, for a given scattering order, the more reliable the solution. The reliability of the solutions were determined by checking how well the boundary conditions are satisfied at the non-planar interface and the convergence of the fields determined at the model surface. The maximum slope of the non-planar interface and the number of scattering orders used are determined by the electrical characteristics of the medium and the frequency of the incident waves.

The presentation of the magnetic and electric field components are of little use in interpretation of MT data (Reddy et al., 1977). Usually the geoelectric structure is neither 1D isotropic or 2D isotropic and the source parameters are unknown. In this study, the field components show some three dimensionality features. The x-component of the magnetic field and the y-component of the electric field have their maximum values diagonally off the corners of the inhomogeneity. The apparent resistivities, especially the ρxx and ρyy show the three dimensionality of the inhomogeneities for both the resistive and conductive cases. The high magnitudes for these apparent resistivities are also diagonally off the corners of the inhomogeneities. The apparent resistivities ρxy and ρyx which are the normal ones investigated, show high values off the edges of the inhomogeneity and low values above for

a conductive inhomogeneity the reverse is true for the resistive case. In the conductive inhomogeneity case, Ex has high magnitude near the edges of the inhomogeneity due to high current density component in this direction. The magnitudes of the skew computed at the model surface have values greater than zero diagonally off the corners of the inhomogeneity. Some MT workers have considered that only skew values greater than 0.2 do indicate a significant 3D geoelectric structure (Reddy et al., 1977). From the models considered here, and also from the work of Ting and Hohmann (1981) it is clear that skew values less than 0.2 also indicate significant 3D effects. If the skew value is greater than zero, then three dimensionality might be suspected.

The Rayleigh-FFT method is an efficient computational technique for modeling structures with gently varying interfaces. Although the models used in this study are simple geometrical ones, this technique can handle more complicated models as long as the zone containing the inhomogeneity can be treated as repetitive. Other advantages of this technique is that models with both high and low resistivity contrast could be modeled (model A has a resistivity contrast of 20 and that of model B is 4000). Also both shallow and deeply buried inhomogeneities in a homogeneous or layered half-space could be modeled. This modeling technique has the advantage that after a set of field components has been obtained, no numerical

differentiation is needed to obtain the other set. The reliability of the solutions obtained can be quantified. The computation time for obtaining both the electric and magnetic field components for an interface of maximum slope of 18 degrees and solution with less than 5 percent RMS error on CDC 6600 was about 30 minutes (Table 2). About half of this time is spent on matrix inversion. If a computer with a larger memory had been available for this study, the matrix inversion could have been accomplished by Gaussian elimination rather than the technique outlined in Appendix C. This would have resulted in significant time savings. Comparisons of computational times for different techniques run on different computers are difficult. However it can be concluded that the Rayleigh-FFT technique is very efficient in handling 3D problems with gentle slopes.

The major disadvantage of this technique is the fact that for large interface slopes (greater than 20 degrees for most models) the reliability of the solution is decreased. The reliability could be improved if more scattering orders are used, but this unfortunately increases the computer memory requirement and computation time. So for large slopes, the long computation time requirement, which is true of all 3D modeling techniques is still a problem.

The numerical technique outlined in this study can be used hand in hand with the other numerical techniques such

as: finite element, integral equation and finite difference, since this technique can handle inhomogeneities with gentle slopes and the others can handle parallelipipeds.

An extension of this work could include: the study of multiple non-planar interfaces which could used in the study of the effects of multiple 3D inhomogeneities (for example, a magma chamber below a sedimentary basin); further studies on the approximation of 3D inhomogeneities by 2D; and an improvement on the matrix inversion routine. Since this numerical technique does not require too much computer time, it will be easy to use for studying MT responses from 3D inhomogeneities, thereby increasing our understanding and subsequently improving the interpretation of MT results.

APPENDIX A

SOLUTION TO THE PARTIAL DIFFERENTIAL EQUATIONS

Since it is difficult to solve the necessary partial differential equations (equations 11) analytically for a general model, the equations will be solved via Fourier transform techniques. After the application of the Fourier transform to the partial differential equations, they will be reduced to ordinary differential equations which can be solved in a straightforward manner.

We define the two-dimensional Fourier transform as:

$$\hat{\psi}(\xi,\eta,z) = \int_{-\infty}^{\infty}\int \psi(x,y,z)\exp(-i\xi x - i\eta y)dx\ dy = \zeta\{\psi\} \qquad A1$$

and the inverse as:

$$\psi(x,y,z) = \frac{1}{4\pi^2}\int_{-\infty}^{\infty}\int \hat{\psi}(\xi,\eta,z)\exp(i\xi x + i\eta y)d\xi\ d\eta = \zeta^{-1}\{\hat{\psi}\}. \qquad A2$$

Differentiating equation A2 with respect to x yields:

$$\frac{\partial\psi}{\partial x}(x,y,z) = \frac{1}{4\pi^2}\int_{-\infty}^{\infty}\int i\xi\hat{\psi}(\xi,\eta,z)\exp(i\xi x + i\eta y)d\xi\ d\eta = \zeta^{-1}\{i\xi\hat{\psi}\}. \qquad A3$$

Using the above to Fourier transform equations (11) along x and y axes and rearranging:

$$\frac{d^2\hat{R}x}{dz^2} - i\xi\frac{d\hat{R}x}{dz} - (\eta^2+\hat{z}\hat{y})\hat{R}x + \xi\eta\hat{R}y = 0 \qquad A4$$

$$\frac{d^2\hat{R}y}{dz^2} - i\eta\frac{d\hat{R}y}{dz} - (\xi^2+\hat{z}\hat{y})\hat{R}y + \xi\eta\hat{R}x = 0 \qquad A5$$

$$-i\xi\frac{d\hat{R}x}{dz} - i\eta\frac{d\hat{R}y}{dz} - (\xi^2+\eta^2+\hat{z}\hat{y})\hat{R}z = 0. \qquad A6$$

Differentiating equation (A6) with respect to z and substituting the value of $\frac{d\hat{R}z}{dz}$ into (A4) and (A5), and solving the resultant equations, we obtain:

$$\hat{R}x = a\exp(\alpha z) + b\exp(-\alpha z) \qquad A7$$

$$\hat{R}y = c\exp(\alpha z) + d\exp(-\alpha z) \qquad A8$$

$$\hat{R}z = -\frac{i}{\alpha}[p\exp(\alpha z) - q\exp(-\alpha z)], \qquad A9$$

where $p = \xi a + \eta c$, $q = \xi b + \eta d$, and $\alpha = \{\xi^2 + \eta^2 + \hat{z}\hat{y}\}^{\frac{1}{2}} = \{\xi^2 + \eta^2 + i\omega\mu(\sigma + i\omega\varepsilon)\}^{\frac{1}{2}}$. Taking the inverse Fourier transform of equations (A7) through (A9), we obtain:

$$Rx(x,y,z) = \frac{1}{4\pi^2}\int_{-\infty}^{\infty}\int [A(\xi,\eta)\exp(\alpha z)+B(\xi,\eta)\exp(-\alpha z)]\exp(i\xi x+i\eta y)d\xi\ d\eta \qquad A10$$

$$Ry(x,y,z) = \frac{1}{4\pi^2}\int_{-\infty}^{\infty}\int [C(\xi,\eta)\exp(\alpha z)+D(\xi,\eta)\exp(-\alpha z)]\exp(i\xi x+i\eta y)d\xi\ d\eta \qquad A11$$

$$Rz(x,y,z) = \frac{-i}{4\pi^2}\int_{-\infty}^{\infty}\int \frac{1}{\alpha}[P(\xi,\eta)\exp(\alpha z)-Q(\xi,\eta)\exp(-\alpha z)]\exp(i\xi x+i\eta y)d\xi\ d\eta \qquad A12$$

The above equations are true for any electrically linear, isotropic and homogeneous medium.

Thus the magnetic field components for different regions (see Figure 5) for a magnetic incident plane wave polarized in the y-direction are:

$$H_{0x} = \frac{1}{4\pi^2}\int_{-\infty}^{\infty}\int A_0\exp(\alpha_0 z)dE \qquad A13.a$$

$$H_{0y} = \frac{1}{4\pi^2}\int_{-\infty}^{\infty}\int C_0\exp(\alpha_0 z)dE + \exp(-\alpha_0 z) \qquad A13.b$$

$$H_{0z} = \frac{-i}{4\pi^2}\int_{-\infty}^{\infty}\int \frac{P_0}{\alpha_0}\exp(\alpha_0 z)dE \qquad A13.c$$

$$H_{1x} = \frac{1}{4\pi^2}\int_{-\infty}^{\infty}\int [A_1\exp(\alpha_1 z) + B_1\exp(-\alpha_1 z)]\,dE \qquad \text{A14.a}$$

$$H_{1y} = \frac{1}{4\pi^2}\int_{-\infty}^{\infty}\int [C_1\exp(\alpha_1 z) + D_1\exp(-\alpha_1 z)]\,dE \qquad \text{A14.b}$$

$$H_{1z} = \frac{-i}{4\pi^2}\int_{-\infty}^{\infty}\int \frac{1}{\alpha_1}[P_1\exp(\alpha_1 z) - Q_1\exp(-\alpha_1 z)]\,dE \qquad \text{A14.c}$$

$$H_{2x} = \frac{1}{4\pi^2}\int_{-\infty}^{\infty}\int [A_2\exp(\alpha_2 z) + B_2\exp(-\alpha_2 z)]\,dE \qquad \text{A15.a}$$

$$H_{2y} = \frac{1}{4\pi^2}\int_{-\infty}^{\infty}\int [C_2\exp(\alpha_2 z) + D_2\exp(-\alpha_2 z)]\,dE \qquad \text{A15.b}$$

$$H_{2z} = \frac{-i}{4\pi^2}\int_{-\infty}^{\infty}\int \frac{1}{\alpha_2}[P_2\exp(\alpha_2 z) - Q_2\exp(-\alpha_2 z)]\,dE \qquad \text{A15.c}$$

$$H_{3x} = \frac{1}{4\pi^2}\int_{-\infty}^{\infty}\int B_3\exp(-\alpha_3 z)\,dE \qquad \text{A16.a}$$

$$H_{3y} = \frac{1}{4\pi^2}\int_{-\infty}^{\infty}\int D_3\exp(-\alpha_3 z)\,dE \qquad \text{A16.b}$$

$$H_{3z} = \frac{i}{4\pi^2}\int_{-\infty}^{\infty}\int \frac{Q_3}{\alpha_3}\exp(-\alpha_3 z)\,dE \qquad \text{A16.c}$$

Using Faraday's law of induction to obtain the electric field, the electric field components in the different regions are:

$$E_{0x} = \frac{1}{4\pi^2 i\omega\varepsilon}\left[\int_{-\infty}^{\infty}\int (\frac{\eta}{\alpha_0}P_0 - \alpha_0 C_0)\exp(\alpha_0 z)\,dE + 4\pi^2\alpha_0\exp(-\alpha_0 z)\right] \qquad \text{A17.a}$$

$$E_{0y} = \frac{1}{4\pi^2 i\omega\varepsilon}\int_{-\infty}^{\infty}\int (\alpha_0 A_0 - \frac{\xi}{\alpha_0}P_0)\exp(\alpha_0 z)\,dE \qquad \text{A17.b}$$

$$E_{0z} = \frac{1}{4\pi^2\omega\varepsilon}\int_{-\infty}^{\infty}\int (\xi C_0 - \eta A_0)\exp(\alpha_0 z)\,dE \qquad \text{A17.c}$$

$$E_{1x} = \frac{1}{4\pi^2\sigma_1}\int_{-\infty}^{\infty}\int \{\frac{\eta}{\alpha_1}[P_1\exp(\alpha_1 z) - Q_1\exp(-\alpha_1 z)] - \alpha_1[C_1\exp(\alpha_1 z) - D_1\exp(-\alpha_1 z)]\}dE \qquad \text{A18.a}$$

$$E_{1y} = \frac{1}{4\pi^2\sigma_1}\int_{-\infty}^{\infty}\int \{\alpha_1[A_1\exp(\alpha_1 z) - B_1\exp(-\alpha_1 z)] - \frac{\xi}{\alpha_1}[P_1\exp(\alpha_1 z) - Q_1\exp(-\alpha_1 z)]\} \qquad \text{A18.b}$$

$$E_{1z} = \frac{i}{4\pi^2\sigma_1} \int_{-\infty}^{\infty}\int \{\xi[C_1\exp(\alpha_1 z)+D_1\exp(-\alpha_1 z)]-\eta[A_1\exp(\alpha_1 z)+B_1\exp(-\alpha_1 z)]\}dE \qquad \text{A18.c}$$

$$E_{2x} = \frac{1}{4\pi^2\sigma_2} \int_{-\infty}^{\infty}\int \{\frac{\eta}{\alpha_2}[P_2\exp(\alpha_2 z)-Q_2\exp(-\alpha_2 z)]-\alpha_2[C_2\exp(\alpha_2 z)-D_2\exp(-\alpha_2 z)]\}dE \qquad \text{A19.a}$$

$$E_{2y} = \frac{1}{4\pi^2\sigma_2} \int_{-\infty}^{\infty}\int \{\alpha_2[A_2\exp(\alpha_2 z)-B_2\exp(-\alpha_2 z)]-\frac{\xi}{\alpha_2}[P_2\exp(\alpha_2 z)-Q_2\exp(-\alpha_2 z)]\}dE \qquad \text{A19.b}$$

$$E_{2z} = \frac{i}{4\pi^2\sigma_2} \int_{-\infty}^{\infty}\int \{\xi[C_2\exp(\alpha_2 z)+D_2\exp(-\alpha_2 z)]-\eta[A_2\exp(\alpha_2 z)+B_2\exp(-\alpha_2 z)]\}dE \qquad \text{A19.c}$$

$$E_{3x} = \frac{-1}{4\pi^2\sigma_3} \int_{-\infty}^{\infty}\int (\frac{\eta}{\alpha_3} Q_3-\alpha_3 D_3)\exp(-\alpha_3 z)dE \qquad \text{A20.a}$$

$$E_{3y} = \frac{-1}{4\pi^2\sigma_3} \int_{-\infty}^{\infty}\int (\alpha_3 B_3-\frac{\xi}{\alpha_3} Q_3)\exp(-\alpha_3 z)dE \qquad \text{A20.b}$$

$$E_{3z} = \frac{i}{4\pi^2\sigma_3} \int_{-\infty}^{\infty}\int (\zeta D_3-\eta B_3)\exp(-\alpha_3 z)dE \qquad \text{A20.c}$$

where $\alpha_0 = \{\xi^2 + \eta^2 - \omega^2\mu\varepsilon\}^{\frac{1}{2}}$,

$\alpha_\ell = \{\xi^2 + \eta^2 + i\omega\mu\sigma_\ell\}^{\frac{1}{2}}$,

$A_\ell = A_\ell(\xi,\eta)$, and

$dE = \exp(i\xi x + i\eta y)d\xi\, d\eta$.

The expressions for the electric field components in regions 1 through 3 are obtained with the assumption that $|\sigma_\ell| >> |i\omega\varepsilon|$.

APPENDIX B

APPLICATION OF THE ELECTROMAGNETIC BOUNDARY CONDITIONS TO A PLANAR AND NON-PLANAR INTERFACE

The boundary conditions at the planar and non-planar interfaces (equations 20 through 22) are applied to obtain algebraic relationships between the spectral amplitudes. These conditions are applied to the model described in figure 5. The expressions for the magnetic and electric field components for the different regions of the model are derived in Appendix A (equations A13 through A20).

At the earth-air interface, the tangential component of the magnetic and electric fields are continuous across the interface (equations 20).

Therefore:

$$H_{0x} = H_{1x}$$
$$H_{0y} = H_{1y}$$

Tangential magnetic field components

$$E_{0x} = E_{1x}$$
$$E_{0y} = E_{1y}$$

Tangential electric field components

Substituting equations A13.a and b, A14.a and b, A17.a and b, and A18.a and b into the above system of equations, evaluated at Z = 0, we obtain:

$$\frac{1}{4\pi^2}\int_{-\infty}^{\infty}\int A_0 dE = \frac{1}{4\pi^2}\int_{-\infty}^{\infty}\int (A_1+B_1)dE \qquad \text{B1.a}$$

$$\frac{1}{4\pi^2}\int_{-\infty}^{\infty}\int C_0 dE + 1 = \frac{1}{4\pi^2}\int_{-\infty}^{\infty}\int (C_1+D_1)dE \qquad \text{B1.b}$$

$$\frac{1}{4\pi^2 i\omega\varepsilon}\left[\int_{-\infty}^{\infty}\int\left(\frac{\eta}{\alpha_0}P_0-\alpha_0 C_0\right)dE+4\pi^2\alpha_0\right]=\frac{1}{4\pi^2\sigma_1}\int_{-\infty}^{\infty}\int\left[\frac{\eta}{\alpha_1}\left(P_1-Q_1\right)-\alpha_1\left(C_1-D_1\right)\right]dE \qquad \text{B1.c}$$

$$\frac{1}{4\pi^2 i\omega\varepsilon}\left[\int_{-\infty}^{\infty}\int\left(\alpha_0 A_0-\frac{\xi}{\alpha_0}P_0\right)dE\right]=\frac{1}{4\pi^2\sigma_1}\int_{-\infty}^{\infty}\int\left[\alpha_1\left(A_1-B_1\right)-\frac{\xi}{\alpha_1}\left(P_1-Q_1\right)\right]dE \qquad \text{B1.d}$$

Taking the Fourier transform of equations B1.a through B1.d and rearranging, we obtain:

$$A_0 = A_1 + B_1 \qquad \text{B2.a}$$

$$C_0 = C_1 + D_1 - 4\pi^2 \qquad \text{B2.b}$$

$$\begin{aligned}&[(\sigma_1\xi\eta/i\omega\varepsilon\alpha_0)-(\xi\eta/\alpha_1)]A_1+[(\sigma_1\xi\eta/i\omega\varepsilon\alpha_0)+(\xi\eta/\alpha_1)]B_1\\&+[(\sigma_1\eta^2/i\omega\varepsilon\alpha_0)-(\sigma_1\alpha_0/i\omega\varepsilon)-(\eta^2/\alpha_1)+\alpha_1]C_1\\&+[(\sigma_1\eta^2/i\omega\varepsilon\alpha_0)-(\sigma_1\alpha_0/i\omega\varepsilon)+(\eta^2/\alpha_1)-\alpha_1]D_1\\&=-4\pi^2(2\alpha_0\sigma_1/i\omega\varepsilon)\delta(\xi)\delta(\eta)\end{aligned} \qquad \text{B2.c}$$

$$\begin{aligned}&[(\sigma_1\alpha_0/i\omega\varepsilon)-(\xi^2\sigma_1/i\omega\varepsilon\alpha_0)-\alpha_1+(\xi^2/\alpha_1)]A_1\\&+[(\sigma_1\alpha_0/i\omega\varepsilon)-(\xi^2\sigma_1/i\omega\varepsilon\alpha_0)+\alpha_1-(\xi^2/\alpha_1)]B_1\\&-[(\sigma_1\xi\eta/i\omega\varepsilon\alpha_0)-(\xi\eta/\alpha_1)]C_1-[(\sigma_1\xi\eta/i\omega\varepsilon\alpha_0)+(\xi\eta/\alpha_1)]D_1=0\end{aligned} \qquad \text{B2.d}$$

$$\text{where}\int_a^b\delta(\xi)=\begin{cases}1 & a\le 0\le b\\ 0 & 0\notin[a,b]\end{cases}$$

At the non-planar interface, $Z = A + f(x,y) = F$, equations (22) describe the appropriate boundary conditions. (Tangential components of magnetic and electric fields are continuous across the boundary.)

Equation 22a,

$$\gamma_y H_{1z} - H_{1y} = \gamma H_{2z} - H_{2y} \quad \text{(y-component of magnetic field)}$$

becomes:

$$i\gamma_y \int_{-\infty}^{\infty} \frac{1}{\alpha_1} [P_1 \exp(\alpha_1 F) - Q_1 \exp(-\alpha_1 F)] dE$$

$$+ \int_{-\infty}^{\infty} [C_1 \exp(\alpha_1 F) + D_1 \exp(\alpha_1 F)]$$

$$= i\gamma_y \int_{-\infty}^{\infty} (1/\alpha_2) [P_2 \exp(\alpha_2 F) - Q_2 \exp(-\alpha_2 F)] dE$$

$$+ \int_{-\infty}^{\infty} [C_2 \exp(\alpha_2 F) + D_2 \exp(-\alpha_2 F)] dE \qquad \text{B3.a}$$

Equation 22b,

$$H_{1x} - \gamma_x H_{1z} = H_{2x} - \gamma_x H_{2z} \quad \text{(x-component of magnetic field)}$$

becomes:

$$\int_{-\infty}^{\infty} [A_1 \exp(\alpha_1 F) + B_1 \exp(-\alpha_1 F)] dE$$

$$+ i\gamma_x \int_{-\infty}^{\infty} (1/\alpha_1) [P_1 \exp(\alpha_1 F) - Q_1 \exp(-\alpha_1 F)] dE$$

$$= \int_{-\infty}^{\infty} [A_2 \exp(\alpha_2 F) + B_2 \exp(-\alpha_2 F)] dE$$

$$+ i\gamma_x \int_{-\infty}^{\infty} (1/\alpha_2) [P_2 \exp(\alpha_2 F) - Q_2 \exp(-\alpha_2 F)] dE \qquad \text{B3.b}$$

Equation 22c,

$$\gamma_y E_{1z} - E_{1y} = \gamma_y E_{2z} - E_{2y} \quad \text{(y-component of electric field)}$$

becomes:

$$(i\gamma_y/\sigma_1)\int_{-\infty}^{\infty}\{\xi[C_1\exp(\alpha_1 F) + D_1\exp(-\alpha_1 F)]$$

$$- \eta[A_1\exp(\alpha_1 F) + B_1\exp(-\alpha_1 F)]\}dE$$

$$- (1/\sigma_1)\int_{-\infty}^{\infty}\{\alpha_1[A_1\exp(\alpha_1 F) - B_1\exp(-\alpha_1 F)]$$

$$- (\xi/\alpha_1)[P_1\exp(\alpha_1 F) - Q_1\exp(-\alpha_1 F)]\}dE$$

$$= (i\gamma_y/\sigma_2)\int_{-\infty}^{\infty}\{\xi[C_2\exp(\alpha_2 F) + D_2\exp(-\alpha_2 F)]$$

$$- \eta[A_2\exp(\alpha_2 F) + B_2\exp(-\alpha_2 F)]\}dE$$

$$- (1/\sigma_2)\int_{-\infty}^{\infty}\{\alpha_2[A_2\exp(\alpha_2 F) - B_2\exp(-\alpha_2 F)]$$

$$- (\xi/\alpha_2)[P_2\exp(\alpha_2 F) - Q_2\exp(-\alpha_2 F)]\}dE \qquad \text{B3.c}$$

and Equation 22d,

$E_{1x} - \gamma_x E_{1z} = E_{2x} - \gamma_x E_{2z}$ (x-component of electric field)

becomes:

$$(1/\sigma_1)\int_{-\infty}^{\infty}\{(\eta/\alpha_1)[P_1\exp(\alpha_1 F) - Q_1\exp(-\alpha_1 F)]$$

$$- \alpha_1[C_1\exp(\alpha_1 F) - D_1\exp(-\alpha_1 F)]\}dE$$

$$- (i\gamma_x/\sigma_1)\int_{-\infty}^{\infty}\{\xi[C_1\exp(\alpha_1 F) + D_1\exp(-\alpha_1 F)]$$

$$- \eta[A_1\exp(\alpha_1 F) + B_1\exp(-\alpha_1 F)]\}dE$$

$$= (1/\sigma_2)\int_{-\infty}^{\infty}\{(\eta/\alpha_2)[P_2\exp(\alpha_2 F) - Q_2\exp(-\alpha_2 F)]$$

$$- \alpha_2[C_2\exp(\alpha_2 F) - D_2\exp(-\alpha_2 F)]\}dE$$

$$- (i\gamma_x/\sigma_2)\int_{-\infty}^{\infty}\{\xi[C_2\exp(\alpha_2 F) + D_2\exp(-\alpha_2 F)]$$

$$- \eta[A_2\exp(\alpha_2 F) + B_2\exp(-\alpha_2 F)]\}dE \qquad \text{B3.d}$$

Substituting the values of P_ℓ and Q_ℓ into equations $B_{3.a}$ through $B_{3.d}$ and rearranging yields the following four equations:

$$\int_{-\infty}^{\infty}\int \{(i\xi\gamma_y/\alpha_1)A_1\exp(\alpha_1 F) - (i\xi\gamma_y/\alpha_1)B_1\exp(-\alpha_1 F)$$

$$+ [1 + (i\eta\gamma_y/\alpha_1)]C_1\exp(\alpha_1 F)$$

$$+ [1 - (i\eta\gamma_y/\alpha_1)]D_1\exp(-\alpha_1 F) - (i\xi\gamma_y/\alpha_2)A_2\exp(\alpha_2 F)$$

$$+ (i\xi\gamma_y/\alpha_2)B_2\exp(-\alpha_2 F) - [1 + (i\eta\gamma_y/\alpha_2)]C_2\exp(\alpha_2 F)$$

$$- [1 - (i\eta\gamma_y/\alpha_2)]D_2\exp(-\alpha_2 F)\}dE = 0 \qquad B4.$$

$$\int_{-\infty}^{\infty}\int \{[1 + (i\xi\gamma_x/\alpha_1)]A_1\exp(\alpha_1 F) + [1 - (i\xi\gamma_x/\alpha_1)]B_1\exp(-\alpha_1 F)$$

$$+ (i\eta\gamma_x/\alpha_1)C_1\exp(\alpha_1 F) - (i\eta\gamma_x/\alpha_1)D_1\exp(-\alpha_1 F)$$

$$- [1 + (i\xi\gamma_x/\alpha_2)]A_2\exp(\alpha_2 F) - [1 - (i\xi\gamma_x/\alpha_2)]B_2\exp(-\alpha_2 F)$$

$$- (i\eta\gamma_x/\alpha_2)C_2\exp(\alpha_2 F) + (i\eta\gamma_x/\alpha_2)D_2\exp(-\alpha_2 F)\}dE = 0 \qquad B4.$$

$$\int_{-\infty}^{\infty}\int \{(\sigma_2/\sigma_1)[(\xi^2/\alpha_1) - \alpha_1 - i\eta\gamma_y]A_1\exp(\alpha_1 F)$$

$$+ (\sigma_2/\sigma_1)[-(\xi^2/\alpha_1) + \alpha_1 - i\eta\gamma_y]B_1\exp(-\alpha_1 F)$$

$$+ (\sigma_2/\sigma_1)[i\xi\gamma_y + (\xi\eta/\alpha_1)]C_1\exp(\alpha_1 F) + (\sigma_2/\sigma_1)[i\xi\gamma_y - (\xi\eta/\alpha_1)]D_1\exp(-\alpha_1 F$$

$$+ [i\eta\gamma_y + \alpha_2 - (\xi^2/\alpha_2)]A_2\exp(\alpha_2 F) + [i\eta\gamma_y - \alpha_2 + (\xi^2/\alpha_2)]B_2\exp(-\alpha_2 F)$$

$$- [i\xi\gamma_y + (\xi\eta/\alpha_2)]C_2\exp(\alpha_2 F) - [i\xi\gamma_y - (\xi\eta/\alpha_2)]D_2\exp(-\alpha_2 F)\}dE = 0$$

B4.

$$\int_{-\infty}^{\infty}\int \{(\sigma_2/\sigma_1)[(\xi\eta/\alpha_1) + i\eta\gamma_x]A_1\exp(\alpha_1 F)$$

$$+ (\sigma_2/\sigma_1)[-(\xi\eta/\alpha_1) + i\eta\gamma_x]B_1\exp(-\alpha_1 F)$$

$$+ (\sigma_2/\sigma_1([(\eta^2/\alpha_1) - \alpha_1 - i\xi\gamma_x]C_1\exp(\alpha_1 F)$$

$$+ (\sigma_2/\sigma_1)[-(\eta^2/\alpha_1) + \alpha_1 - i\xi\gamma_x)]D_1\exp(-\alpha_1 F)$$

$$- [(\xi\eta/\alpha_2) + i\eta\gamma_x]A_2\exp(\alpha_2 F) + [(\xi\eta/\alpha_2) - i\eta\gamma_x]B_2\exp(-\alpha_2 F)$$

$$+ [-(\eta^2/\alpha_2) + \alpha_2 + i\xi\gamma_x]C_2\exp(\alpha_2 F)$$

$$+ [(\eta^2/\alpha_2) - \alpha_2 + i\xi\gamma_x]D_2\exp(-\alpha_2 F)\}dE = 0 \qquad \text{B4.d}$$

Considering the boundary conditions at the third interface, where Z = H, (equation 21) and using equations A15.a, A15.b, A16.a, A16.b, A19.a, A19.b, A20.a, and A20.b, we have:

Equation 21a,

$H_{2x} = H_{3x}$ (x-component of the magnetic field)

becomes:

$$(1/4\pi^2)\int_{-\infty}^{\infty}\int [A_2\exp(\alpha_2 H) + B_2\exp(-\alpha_2 H)]dE$$

$$= (1/4\pi^2)\int_{-\infty}^{\infty}\int B_3\exp(-\alpha_3 H)dE \qquad \text{B5.a}$$

Equation 21b,

$H_{2y} = H_{3y}$ (y-component of the magnetic field)

becomes:

$$(1/4\pi^2)\int_{-\infty}^{\infty}\int [C_2\exp(\alpha_2 H) + D_2\exp(-\alpha_2 H)]dE$$

$$= (1/4\pi^2)\int_{-\infty}^{\infty}\int D_3\exp(-\alpha_3 H)dE \qquad \text{B5.b}$$

Equation 21c,

$E_{2x} = E_{3x}$ (x-component of the electric field)

becomes:

$$(1/4\pi^2\sigma_2)\int_{-\infty}^{\infty}\int \{(\eta/\alpha_2)[P_2\exp(\alpha_2 H) - Q_2\exp(-\alpha_2 H)]$$

$$- \alpha_2[C_2\exp(\alpha_2 H) - D_2\exp(-\alpha_2 H)]\}dE$$

$$= -(1/4\pi^2\sigma_3)\int_{-\infty}^{\infty}\int [(\eta/\alpha_3)Q_3 - \alpha_3 D_3]\exp(-\alpha_3 H)dE \qquad \text{B5.c}$$

and Equation 21d,

$E_{2y} = E_{3y}$ (y-component of the electric field)

becomes:

$$(1/4\pi^2\sigma_2)\int_{-\infty}^{\infty}\int \{\alpha_2[A_2\exp(\alpha_2 H) - B_2\exp(-\alpha_2 H)]$$

$$- (\xi/\alpha_2)[P_2\exp(\alpha_2 H) - Q_2\exp(-\alpha_2 H)]\}dE$$

$$= (1/4\pi^2\sigma_3)\int_{-\infty}^{\infty}\int [\alpha_3 B_3 - (\xi/\alpha_3)Q_3]\exp(-\alpha_2 H)dE \qquad \text{B5.d}$$

Taking the Fourier transform of equations B5.a through B5.d and rearranging as was done for the earth-air interface;

$$B_3 = [A_2\exp(\alpha_2 H) + B_2\exp(-\alpha_2 H)]\exp(\alpha_3 H) \qquad \text{B6.a}$$

$$D_3 = [C_2\exp(\alpha_2 H) + D_2\exp(-\alpha_2 H)]\exp(\alpha_3 H) \qquad \text{B6.b}$$

$$\xi\eta[(\sigma_3/\sigma_2\alpha_2) + (1/\alpha_3)]A_2\exp(\alpha_2 H)$$

$$+ \xi\eta[-(\sigma_3/\sigma_2\alpha_2) + (1/\alpha_3)]B_2\exp(-\alpha_2 H)$$

$$+ \{(\sigma_3/\sigma_2)[(\eta^2/\alpha_2) - \alpha_2] + (\eta^2/\alpha_3) - \alpha_3\}C_2\exp(\alpha_2 H)$$

$$+ \{(\sigma_3/\sigma_2)[-(\eta^2/\alpha_2) + \alpha_2] + (\eta^2/\alpha_3) - \alpha_3\}D_3\exp(-\alpha_2 H) = 0 \qquad \text{B6.c}$$

$$\{(\sigma_3/\sigma_2)[\alpha_2 - (\xi^2/\alpha_2)] - (\xi^2/\alpha_3) + \alpha_3\}A_2\exp(\alpha_2 H)$$

$$+ \{(\sigma_3/\sigma_2)[-\alpha_2 + (\xi^2/\alpha_2)] - (\xi^2/\alpha_3) + \alpha_3\}B_2\exp(-\alpha_2 H)$$

$$- \xi\eta[(\sigma_3/\sigma_2\alpha_2) + (1/\alpha_3)]C_2\exp(\alpha_2 H)$$

$$+ \xi\eta[(\sigma_3/\sigma_2\alpha_2) - (1/\alpha_3)]D_3\exp(-\alpha_2 H) = 0 \qquad \text{B6.d}$$

The values of A_1 and C_1 from equations B2.c and B2.d, and the values of A_2 and C_2 from equations B6.c and B6.d are substituted into equations B4.a through B4.d giving the following:

Equation B4.a yields:

$$\int_{-\infty}^{\infty}\int (g_1B_1 + g_2D_1 + g_3B_2 + g_4D_2)dE = \int_{-\infty}^{\infty}\int h_1 dE \qquad \text{B7.a}$$

Equation B4.b yields:

$$\int_{-\infty}^{\infty}\int (g_5B_1 + g_6D_1 + g_7B_2 + g_8D_2)dE = \int_{-\infty}^{\infty}\int h_2 dE \qquad \text{B7.b}$$

Equation B4.c yields:

$$\int_{-\infty}^{\infty}\int (g_9B_1 + g_{10}D_1 + g_{11}B_2 + g_{12}D_2)dE = \int_{-\infty}^{\infty}\int h_3 dE \qquad \text{B7.c}$$

Equation B4.d yields:

$$\int_{-\infty}^{\infty}\int (g_{13}B_1 + g_{14}D_1 + g_{15}B_2 + g_{16}D_2)dE = \int_{-\infty}^{\infty}\int h_4 dE \qquad \text{B7.d}$$

where $g_1 = T_1\Gamma_{4p} - \Gamma_{4m} + T_4\Gamma_{5p}$

$g_2 = T_2\Gamma_{4p} + T_5\Gamma_{5p} + \Gamma_{5m}$

$g_3 = \Gamma_{6m} - T_9\Gamma_{7p} + T_7\Gamma_{6p}$

$g_4 = -\Gamma_{7m} - T_{10}\Gamma_{7p} + T_8\Gamma_{6p}$

$g_5 = T_1\Gamma_{8p} + \Gamma_{8m} + T_4\Gamma_{9p}$

$g_6 = T_2\Gamma_{8p} + T_5\Gamma_{9p} - \Gamma_{9m}$

$g_7 = -\Gamma_{10m} - T_7\Gamma_{10p} + T_9\Gamma_{11p}$

$g_8 = \Gamma_{11m} + T_{10}\Gamma_{11p} - T_8\Gamma_{10p}$

$g_9 = T_4\Gamma_{13p} + T_1\Gamma_{12p} + \Gamma_{12m}$

$g_{10} = T_5\Gamma_{13p} + T_2\Gamma_{12P} + \Gamma_{13m}$

$g_{11} = \Gamma_{14m} - T_9\Gamma_{15p} + T_7\Gamma_{14p}$

$g_{12} = -\Gamma_{15m} - T_{10}\Gamma_{15p} + T_8\Gamma_{14p}$

$g_{13} = T_1\Gamma_{16p} + \Gamma_{16m} + T_4\Gamma_{17p}$

$g_{14} = T_2\Gamma_{16p} + T_5\Gamma_{17p} + \Gamma_{17m}$

$g_{15} = \Gamma_{18m} - T_7\Gamma_{18p} + T_9\Gamma_{19p}$

$g_{16} = \Gamma_{19m} - T_8\Gamma_{18p} + T_{10}\Gamma_{19p}$

$h_1 = -T_3\Gamma_{4p} - T_6\Gamma_{5p}$

$h_2 = -T_3\Gamma_{8p} - T_6\Gamma_{9p}$

$$h_3 = -T_3\Gamma_{12p} - T_6\Gamma_{13p} \quad \text{and}$$

$$h_4 = -T_3\Gamma_{16p} - T_6\Gamma_{17p} \quad .$$

From equations B2.c, B2.d, B4.a through B4.d, B6.c and B6.d;

$$\lambda = -(8\pi^2\sigma_1\alpha_0)\delta(\xi)\delta(\eta)/(i\omega\varepsilon)$$

$$\Gamma_{1p} = (\sigma_1\xi\eta/i\omega\varepsilon\alpha_0) - (\xi\eta/\alpha_1), \qquad \Gamma_{1m} = (\sigma_1\xi\eta/i\omega\varepsilon\alpha_0) + (\xi\eta/\alpha_1)$$

$$\Gamma_{2p} = (\sigma_1\eta^2/i\omega\varepsilon\alpha_0) - (\sigma_1\alpha_0/i\omega\varepsilon) - (\eta^2/\alpha_1) + \alpha_1$$

$$\Gamma_{2m} = (\sigma_1\eta^2/i\omega\varepsilon\alpha_0) - (\sigma_1\alpha_0/i\omega\varepsilon) + (\eta^2/\alpha_1) - \alpha_1$$

$$\Gamma_{3p} = (\sigma_1\alpha_0/i\omega\varepsilon) - (\sigma_1\xi^2/i\omega\varepsilon\alpha_0) - \alpha_1 + (\xi^2/\alpha_1)$$

$$\Gamma_{3m} = (\sigma_1\alpha_0/i\omega\varepsilon) - (\sigma_1\xi^2/i\omega\varepsilon\alpha_0) + \alpha_1 - (\xi^2/\alpha_1)$$

$$\Gamma_{4p} = (i\xi\gamma_y/\alpha_1)\exp(\alpha_1 F), \qquad \Gamma_{4m} = (i\xi\gamma_y/\alpha_1)\exp(-\alpha_1 F)$$

$$\Gamma_{5p} = [1 + (i\eta\gamma_y/\alpha_1)]\exp(\alpha_1 F), \qquad \Gamma_{5m} = [1 - (i\eta\gamma_y/\alpha_1)]\exp(-\alpha_1 F)$$

$$\Gamma_{6p} = -(i\xi\gamma_y/\alpha_2)\exp(\alpha_2 F), \qquad \Gamma_{6m} = (i\xi\gamma_y/\alpha_2)\exp(-\alpha_2 F)$$

$$\Gamma_{7p} = [1 + (i\eta\gamma_y/\alpha_2)]\exp(\alpha_2 F), \qquad \Gamma_{7m} = [1 - (i\eta\gamma_y/\alpha_2)]\exp(-\alpha_2 F)$$

$$\Gamma_{8p} = [1 + (i\xi\gamma_x/\alpha_1)]\exp(\alpha_1 F), \qquad \Gamma_{8m} = [1 - (i\xi\gamma_x/\alpha_1)]\exp(-\alpha_1 F)$$

$$\Gamma_{9p} = (i\eta\gamma_x/\alpha_1)\exp(\alpha_1 F), \qquad \Gamma_{9m} = (i\eta\gamma_x/\alpha_1)\exp(-\alpha_1 F)$$

$$\Gamma_{10p} = [1 + (i\xi\gamma_x/\alpha_2)]\exp(\alpha_2 F), \qquad \Gamma_{10m} = [1 - (i\xi\gamma_x/\alpha_2)]\exp(-\alpha_2 F)$$

$$\Gamma_{11p} = -(i\eta\gamma_x/\alpha_2)\exp(\alpha_2 F), \qquad \Gamma_{11m} = (i\eta\gamma_x/\alpha_2)\exp(-\alpha_2 F)$$

$$\Gamma_{12p} = (\sigma_2/\sigma_1)[-i\eta\gamma_y - \alpha_1 + (\xi^2/\alpha_1)]\exp(\alpha_1 F)$$

$$\Gamma_{12m} = (\sigma_2/\sigma_1)[-i\eta\gamma_y + \alpha_1 - (\xi^2/\alpha_1)]\exp(-\alpha_1 F)$$

$$\Gamma_{13p} = (\sigma_2/\sigma_1)[i\xi\gamma_y + (\xi\eta/\alpha_1)]\exp(\alpha_1 F)$$

$$\Gamma_{13m} = (\sigma_2/\sigma_1)[i\xi\gamma_y - (\xi\eta/\alpha_1)]\exp(-\alpha_1 F)$$

$$\Gamma_{14p} = [\alpha_2 + i\eta\gamma_y - (\xi^2/\alpha_2)]\exp(\alpha_2 F)$$

$$\Gamma_{14m} = [-\alpha_2 + i\eta\gamma_y + (\xi^2/\alpha_2)]\exp(-\alpha_2 F)$$

$$\Gamma_{15p} = [i\xi\gamma_y + (\xi\eta/\alpha_2)]\exp(\alpha_2 F)$$

$$\Gamma_{15m} = [i\xi\gamma_y - (\xi\eta/\alpha_2)]\exp(-\alpha_2 F)$$

$$\Gamma_{16p} = [i\eta\gamma_x + (\xi\eta/\alpha_1)](\sigma_2/\sigma_1)\exp(\alpha_1 F)$$

$$\Gamma_{16m} = (\sigma_2/\sigma_1)[i\eta\gamma_x - (\xi\eta/\alpha_1)]\exp(-\alpha_1 F)$$

$$\Gamma_{17p} = (\sigma_2/\sigma_1)[-i\xi\gamma_x - \alpha_1 + (\eta^2/\alpha_1)]\exp(\alpha_1 F)$$

$$\Gamma_{17m} = (\sigma_2/\sigma_1)[-i\xi\gamma_x + \alpha_1 - (\eta^2/\alpha_1)]\exp(-\alpha_1 F)$$

$$\Gamma_{18p} = [(\xi\eta/\alpha_2) + i\eta\gamma_x]\exp(\alpha_2 F), \qquad \Gamma_{18m} = [(\xi\eta/\alpha_2) - i\eta\gamma_x]\exp(-\alpha_2 F)$$

$$\Gamma_{19p} = [i\xi\gamma_x + \alpha_2 - (\eta^2/\alpha_2)]\exp(\alpha_2 F)$$

$$\Gamma_{19m} = [i\xi\gamma_x - \alpha_2 + (\eta^2/\alpha_2)]\exp(-\alpha_2 F)$$

$$\Gamma_{20p} = [(\sigma_3\xi\eta/\sigma_2\alpha_2) + (\xi\eta/\alpha_3)]\exp(\alpha_2 H)$$

$$\Gamma_{20m} = \xi\eta[-(\sigma_3/\sigma_2\alpha_2) + (1/\alpha_3)]\exp(-\alpha_2 H)$$

$$\Gamma_{21p} = \{(\sigma_3/\sigma_2)[-\alpha_2 + (\eta^2/\alpha_2)] - \alpha_3 + (\eta^2/\alpha_3)\}\exp(\alpha_2 H)$$

$$\Gamma_{21m} = \{(\sigma_3/\sigma_2)[\alpha_2 - (\eta^2/\alpha_2)] - \alpha_3 + (\eta^2/\alpha_3)\}\exp(-\alpha_2 H)$$

$$\Gamma_{22p} = \{(\sigma_3/\sigma_2)[\alpha_2 - (\xi^2/\alpha_2)] + \alpha_3 - (\xi^2/\alpha_3)\}\exp(\alpha_2 H)$$

$$\Gamma_{22m} = \{(\sigma_3/\sigma_2)[-\alpha_2 + (\xi^2/\alpha_2)] + \alpha_3 - (\xi^2/\alpha_3)\}\exp(-\alpha_2 H)$$

In solving for A_1, C_1, A_2 and C_2 from equations B2.c, B2.d, B6.c and B6.d, the following equations are used:

$$T_1 = -[(\Gamma_{3m}/\Gamma_{3p}) + (\Gamma_{1p}\beta_3/\Gamma_{3p}\beta_1)]$$

$$T_2 = (\Gamma_{1m}/\Gamma_{3p}) - (\Gamma_{1p}\beta_2/\Gamma_{3p}\beta_1)$$

$$T_3 = \lambda\Gamma_{1p}/\beta_1, \qquad T_4 = -\beta_3/\beta_1, \qquad T_5 = -\beta_2/\beta_1$$

$$T_6 = \lambda\Gamma_{3p}/\beta_1, \qquad T_7 = -\beta_4/\beta_5, \qquad T_8 = -\beta_6/\beta_5$$

$$T_9 = (\Gamma_{20p}\beta_4/\Gamma_{21p}\beta_5) - (\Gamma_{20m}/\Gamma_{21p})$$

$$T_{10} = (\Gamma_{20p}\beta_6/\Gamma_{21p}\beta_5) - (\Gamma_{21m}/\Gamma_{21p})$$

where $\beta_1 = \Gamma_{2p}\Gamma_{3p} + \Gamma_{1p}\Gamma_{1p}$,

$\beta_2 = \Gamma_{3p}\Gamma_{2m} + \Gamma_{1p}\Gamma_{1m}$, $\qquad \beta_3 = \Gamma_{1m}\Gamma_{3p} - \Gamma_{1p}\Gamma_{3m}$,

$\beta_4 = \Gamma_{21p}\Gamma_{22m} + \Gamma_{20m}\Gamma_{20p}$, $\qquad \beta_5 = \Gamma_{21p}\Gamma_{22p} + \Gamma_{20p}\Gamma_{20p}$

and $\beta_6 = \Gamma_{21m}\Gamma_{20p} - \Gamma_{21p}\Gamma_{20m}$.

APPENDIX C

MATRIX INVERSION VIA COLUMN OPERATIONS

From time to time large dense matrices are encountered which do not have useful properties which can be exploited such as being banded or diagonally dominant. Although Gaussian elimination routines are efficient, they usually require that the whole matrix be in the local memory of the computer. In cases where computer memory space available is limited, which is often the case, matrices of dimensions larger than the available storage space present some difficulties. To overcome this problem with lack of core space, a routine that does not require storage of all the matrix in core at the same time has to be used. Iterative techniques satisfy this condition but most of them require that the matrix be diagonally dominant.

In the present problem, the (complex) matrices have dimensions larger than the available core space. The matrices were inverted with the technique described below. The column operations used are those routinely employed in optimization algorithms. (The technique was brought to the attention of the author by Dr. R. Helgason of Operations

Research Department of SMU).

Column operation technique;

The problem is to obtain the solution to the system of linear equations;

$$\underline{\underline{G}}\underline{x} = \underline{b}$$

where the matrix $\underline{\underline{G}}$ is complex, dense and stable.

Store the columns of the matrix $\underline{\underline{G}}$ in Gi and the vector b which is in the local memory is copied onto x. Initialise by filling a vector L with zeroes.

Access the first column of $\underline{\underline{G}}$, Gl

Determine the absolute maximum element of Gl, Gj,1. j is the pivot for column 1, store the column number, 1, in L(j)

Form an identity matrix $\underline{\underline{E}}$ with a column filled with the following elements;

$$-Gi,1/Gj,1 \quad i=1,2,3,\ldots,j-1,j+1,\ldots n$$

and $1/Gj,1$ at $i=j$.

These entries are at the jth column of $\underline{\underline{E}}$.

The identity column matrix $\underline{\underline{E}}$ for column 1 of $\underline{\underline{G}}$ should satisfy the following equations;

$$Ei,k*Gk,1 = \delta ij \qquad k=1,2,3,\ldots..n$$

where $\delta ij = 0, \quad i \neq j$

and $\delta_{ij} = 1, \quad i = j$ j is the pivot.

The column matrix $\underline{E}$ thus formed for column 1 of $\underline{G}$ is stored as a column E1.

The solution vector is updated to

$x_1 = E1*x$

Note that although E1 is stored as a column, it is an identity matrix with full entries in the jth column).

Operation for the kth column of G.

Access column Gk.

Successively multiply Gk by the identity column matrices, Ei (i=1,2,.. k-1), i.e.

$$Ek-1(....(E2(E1(Gk)))...) = G'k$$

Determine the pivot for G'k (L has to be searched for a vacant position).

Then form an identity column matrix for G'k to be stored in Ek, and store k in L(j).

Update the solution vector

$$x_k = Ek*x_{k-1}$$

When the last identity column matrix En is obtained, multiply En by $x_{n-1}$to obtain the solution.

The solution of the system of equations is obtained by sorting x_n and L such that L is in ascending order.

Algorithm.

```
Store Gi (columns of G).
    For i=1 to n do
          L(i)=0
          x(i)=b(i)
    end for

Read G1
     Call procedure Etaj(E1,G,N,L,M)
     Call procedure Emultip(E1,x,N,L,1)
     write E1
     For i=2 to N do
          read Gi
          for m=1 to i-1
              read Em
              Call procedure Emultip(Em,Gi,N,L,M)
          end for
         Call procedure Etaj(Ei,Gi,N,L,i)
         Call procedure Emultip(Ei,x,N,L,i)
         write Ei
     end for

for k=1 to N do
    sol(L(k)) = x(k)
end for
```

(sol contains the solution vector).

```
Procedure Etaj(E,G,N,L,Icol)
complex E(N),G(N)
integer N,L(N),J,Icol

j=0
gmax=cabs(G1)
for i=1 to N do
    if(L(i)=0 and cabs (G(i)).gt.gmax) then
        gmax=cabs(G(i))
        j=i
    else
    end if
end for
L(j)=Icol
for k=1 to N do
    if(k=j) then
      E(k)=1 G(j)
       else
      E(k)=-G(k) G(j)
    end if
end for
```

```
Procedure Emultip(E,A,N,L,Icol)
 complex A(N),E(N)
 integer L(N),N,J,Icol
for k=1 to N do
    if(L(k)=Icol) then
       j=k
       else
    end if
end for

for i=1 to N do
    if(i=j) then
       A(i)=E(i)*A(i)
        else
       A(i)=A(i)+E(i)*A(j)
    end if
end for
```

APPENDIX D

ELECTROMAGNETIC FIELD PARAMETERS

In a magnetotelluric survey, the three components of the magnetic field and the two horizontal components of the electric fields are usually measured at the same station for some length of time. The duration for a particular measurement depends on the locality, the depth to the exploration target and the source spectrum as a function of time. The depth of penetration for electromagnetic waves is determined by the skin depth, ($\delta = (\rho/\pi\mu f)^{\frac{1}{2}}$) of the medium, where ρ is the resistivity, μ is the magnetic permeability for the medium and f is the frequency of the waves. For a shallow body, the time for the measurements is relatively shorter than for a deep one. If the top layer is very conductive, then the measurements have to be over longer periods than if the layer were more resistive.

At the completion of the survey, the data is analysed in various ways. The first phase of data analysis involves manual editing. Each of the five field components are then Fourier transformed, and averaged over a finite band width yielding in-phase and quadrature values for each

component at different frequency bands. The impedance tensor is then calculated from the fields. These values are then substituted into equations (D1) and (D2) below in order to calculate the predicted electric field components. The coherencies between calculated and predicted electric fields are then calculated. Differences between the observed and calculated fields are due to noise either in the magnetic or electric field components. Frequency bands with coherencies of less than 0.95 are considered noisy and should be rejected (Vozoff, 1972). The main concern of an MT interpreter is the estimation of apparent resistivities for the subsurface. In order to accomplish this, it is advantageous if the dimensionality or the general trend of the inhomogeneity is known. This information could be available from knowledge of the geology of the area and/or from other geophysical investigations. In order to determine the dimensionality or the general trend of an inhomogeneity from an MT survey, several parameters are computed from the fields at different frequencies. These parameters include; impedance tensor, principal axes directions , tipper magnitude and azimuth, skew and ellipticity. Computation of these parameters and their characteristics will be discussed later.

Impedance tensor.

The horizontal components of the magnetic and

electric fields for a particular frequency at the surface of earth are related by:

$$Ex(\omega) = Zxx(\omega).Hx(\omega) + Zxy(\omega).Hy(\omega) \quad D1$$

$$Ey(\omega) = Zxy(\omega).Hx(\omega) + Zyy(\omega).Hy(\omega) \quad D2$$

The above relations can be expressed in a concise form as:

$$\underline{E}(\omega) = \underline{\underline{Z}}(\omega)\underline{H}(\omega) \quad D3$$

where $\underline{E}(\omega)$ is the vector $(Ex(\omega), Ey(\omega))$,
$\underline{H}(\omega)$ is the vector $(Hx(\omega), Hy(\omega))$ and
$\underline{\underline{Z}}(\omega)$ is the impedance tensor given by;

$$\underline{\underline{Z}}(\omega) = \begin{pmatrix} Zxx(\omega) & Zxy(\omega) \\ Zyx(\omega) & Zyy(\omega) \end{pmatrix} \quad D4$$

There are four unknowns in the above two equations. In order to solve for the unknowns, two independent source orientations in which the magnetic field source is polarized in 1) the y-direction and 2) the x-direction (Vozoff, 1972) are used. The relationship between the magnetic and electric field components for the two source polarization directions are then;

$$Ex1(\omega) = Zxx(\omega).Hx1(\omega) + Zxy(\omega).Hy1(\omega) \quad D5$$

$$Ex2(\omega) = Zxx(\omega).Hx2(\omega) + Zxy(\omega).Hy2(\omega) \quad D6$$

and

$$Ey1(\omega) = Zyx(\omega).Hx1(\omega) + Zyy(\omega).Hy1(\omega) \quad D7$$

$$Ey2(\omega) = Zyx(\omega).Hx2(\omega) + Zyy(\omega).Hy2(\omega) \quad D8$$

The impedance tensor elements from the above equations are;

$$Zxx(\omega) = \frac{Ex1(\omega).Hy2(\omega) - Ex2(\omega).Hy1(\omega)}{Hx1(\omega).Hy2(\omega) - Hx2(\omega).Hy1(\omega)} \quad D9$$

$$Zyy(\omega) = \frac{Ey1(\omega).Hx2(\omega) - Ey2(\omega).Hx1(\omega)}{Hx2(\omega).Hy1(\omega) - Hy2(\omega).Hx1(\omega)} \quad D10$$

$$Zxy(\omega) = \frac{Ex2(\omega).Hx1(\omega) - Ex1(\omega).Hx2(\omega)}{Hx1(\omega).Hy2(\omega) - Hx2(\omega).Hy1(\omega)} \quad D11$$

$$Zyx(\omega) = \frac{Ey2(\omega).Hy1(\omega) - Ey1(\omega).Hy2(\omega)}{Hx2(\omega).Hy1(\omega) - Hx1(\omega).Hy2(\omega)} \quad D12$$

After the impedance tensor elements have been obtained from the above equations, the values of the apparent resistivity, ρ, and phase changes of the tensor elements of

the tensor are calculated using the following;

$$\rho_{ij} = |Z_{ij}|^2/\mu\omega \qquad \text{D13}$$

and $$\theta_{ij} = \tan^{-1}(\mathrm{Im}(Z_{ij})/\mathrm{Re}(Z_{ij})) \qquad \text{D14}$$

where i,j is either x or y,
Re(Zij) and Im(Zij) are the real and imaginary parts of Zij, and
θ_{ij} is the phase angle.

The magnitudes and phases of the elements of the impedance tensor help in the identification of the dimensionality of the inhomogeneity being encountered. For example, when the geology is <u>one-dimensional</u>, $Z_{xx}(\omega) = Z_{yy}(\omega) = 0$ and $Z_{xy}(\omega) = -Z_{yx}(\omega)$ (Goubau et al., 1978). In the case of a <u>two-dimensional</u> inhomogeneity, according to Vozoff (1972), if neither of the coordinate axes is along the direction of strike, all the elements of the impedance tensor are non-zero and have different values. When the magnetic field is polarized along the strike direction, $Z_{xx}(\omega)$ and $Z_{yy}(\omega)$ are zero and the other two elements are non-zero and unequal. For a 90 degree rotation in the coordinate axes, the situation is unchanged except that the impedance tensor values are interchanged. For <u>three-dimensional</u> structures, Sims and Bostick (1969) arrived at the following relationships;

$Zxx(\omega) + Zyy(\omega)$ = constant, and $Zxy(\omega) - Zyx(\omega)$ = constant.

As shown by Ting and Hohmann (1981), the phases of the impedance tensor elements for 3D inhohmogeneity do not explicitly show three-dimensionality, although the phases θxy and θyx have relatively higher values in the region of the inhomogeneity. In the case of θxx and θyy, the high values were observed near the corners of their model. They also found that the apparent resistivities ρxx and ρyy for a 3D body have zero values along the axes of symmetry and their maximum values are observed near the corners of the body.

Principal axes.

The impedance tensor is usually calculated in a coordinate system (x,y,z). It can be rotated horizontally into any other coordinate system (x´,y´,z) through an angle measured in the clockwise direction (Ting and Hohmann, 1981). The following are the rotated impedance elements for a given frequency;

$$2Z'xx(\theta) = (Zxx + Zyy) + (Zxx - Zyy)\cos 2\theta + (Zxy + Zyx)\sin 2\theta, \qquad D15$$

$$2Z'xy(\theta) = (Zxy - Zyx) + (Zxy + Zyx)\cos 2\theta -$$

$$(Zxx - Zyy)\sin 2\theta, \qquad \text{D16}$$

$$2Z'yx(\theta) = -(Zxy - Zyx) + (Zxy + Zyx)\cos 2\theta - (Zxx - Zyy)\sin 2\theta, \qquad \text{D17}$$

and

$$2Z'yy(\theta) = (Zxx + Zyy) - (Zxx - Zyy)\cos 2\theta - (Zxy + Zyx)\sin 2\theta. \qquad \text{D18}$$

The values of the rotation angle, θ, at which Z'xy is a maximum and Z'yx is a minimun defines the principal axes of Z (Vozoff, 1972). Ting and Hohmann (1981), also defined the principal axes as derived from the impedance tensor as the angle which maximizes $|Z'xy|^2 + |Z'yx|^2$ minimize $|Z'xx| + |Z'yy|$, maximize $|Z'xy|$ or $|Z'yx|$, minimize $|Z'xx|$ or $|Z'yy|$, maximize $|Z'xy + Z'yx|$, etc.

Analytically, setting the first derivative of $|Z'xy + Z'yx|$ equal to zero, the angle θ_0 obtained, is given by;

$$\theta_0 = \frac{1}{4}\tan^{-1}\left[\frac{2(R1R2 + I1I2)}{(R1^2 + I1^2 - R2^2 - I2^2)}\right] \qquad \text{D19}$$

where R1, R2 and I1, I2 are the real and imaginary parts of $(Zxx(\omega) - Zyy(\omega))$ and $(Zxy(\omega) + Zyx(\omega))$ respectively.

The above equation is satisfied by eight values of θ_0 between 0 and 360 degrees. The four that give the maximum

values of Z´xy + Z´yx form the two principal axes perpendicular to one another. For a one-dimensional case, rotation does not affect the magnitude of Z, so it plots along a circle. In the case of two and three-dimensional inhomogeneities, the impedance elements plot are elongated in a direction either parallel or perpendicular to the strike (or pseudo-strike), so the principal axes, (the axes of the ellipse) are parallel and perpendicular to the strike direction (Reddy et al., 1977).

Ellipticity.

When the coordinate axes for the computation of the impedance tensor are rotated, the magnitudes of the impedance elements, in a general case, plot on an ellipse, as seen from the previous section. The ratio of the minor to the major axes of the ellipse is called the ellipticity. It can be obtained analytically (Word et al, 1970) from;

$$\text{Ellipticity} = \left| \frac{(Zxx - Zyy)\cos 2\theta_o + (Zxy + Zyx)\sin 2\theta_o}{(Zxy + Zyx)\cos 2\theta_o + (Zxx - Zyy)\sin 2\theta_o} \right| \quad \text{D20}$$

where θ_o is any of the principal axes from above and the impedance elements are for a given frequency.

Note that the ellipticity for one and two dimensional structures is zero (Ting and Hohmann, 1981),

whereas for three dimensional structures, ellipticity is zero only along the axes of symmetry. In this case the maximum values were observed off the corners of the structure.

Skew.

It was noted above that the impedance tensor elements have different characteristics depending on the dimensionality of the body under investigation. For 1D, $Zxx(\omega) = Zyy(\omega) = 0$ and $Zxy(\omega) = -Zyx(\omega)$, for 2D, $Zxx(\omega) + Zyy(\omega) = 0$ and $Zxy(\omega) - Zyx(\omega) =$ constant, whereas for 3D, $Zxx(\omega) + Zyy(\omega) =$ constant and $Zxy(\omega) - Zyx(\omega) =$ constant. Skew, a three-dimensional parameter, is defined as;

$$\text{Skew} = \left(\frac{|Zxx(\omega) + Zyy(\omega)|}{|Zxy(\omega) - Zyx(\omega)|} \right) \qquad \text{D21}$$

Since $Zxx(\omega) + Zyy(\omega)$ is zero for both 1D and 2D, Skew for 1D and 2D is zero. It has been observed by Ting and Hohmann (1981), that skew is also zero for their 3D model along the axes of symmetry.

Tipper.

The horizontal components of the magnetic field could be related to the vertical component as follows;

$$Hz(\omega) = Xzx(\omega).Hx(\omega) + Xzy(\omega).Hy(\omega) \qquad D22$$

Xzx(ω) and Xzy(ω) are unknown complex coefficients which are refered to as the magnetic parameters or magnetic transfer functions (Reddy et al., 1977). The complex coefficients are solved for in an analogous way to the solution for the impedance tensor. Two source polarizations are considered, and the two unknowns are solved from:

$$Hz1(\omega) = Xzx(\omega).Hx1(\omega) + Xzy(\omega).Hy1(\omega) \qquad D23$$

$$Hz2(\omega) = Xzx(\omega).Hx2(\omega) + Xzy.Hy2(\omega) \qquad D24$$

and,

$$Xzx(\omega) = \frac{Hz1(\omega).Hy2(\omega) - Hy1(\omega).Hz2(\omega)}{Hx1(\omega).Hy2(\omega) - Hy1(\omega).Hx2(\omega)} \qquad D25$$

$$Xzy(\omega) = \frac{Hx1(\omega).Hz2(\omega) - Hx2(\omega).Hz1(\omega)}{Hx1(\omega).Hy2(\omega) - Hy1(\omega).Hx2(\omega)} \qquad D26$$

Reddy et al. (1977), plotted polar diagrams for magnetic transfer functions similar to those of the impedance tensor elements by rotating the coordinate axes from 0 through 360

degrees using the relations;

$$X'zx(\alpha) = Xzx\cos\alpha + Xzy\sin\alpha \qquad D27$$

for a given frequency.

For one-dimensional structure, $Xzx(\omega) = Xzy(\omega) = 0$, and for a two-dimensional structure with axis parallel to x', $Hz(\omega) = Xzy'(\omega).Hy(\omega)$ and $Xzx'(\omega) = 0$.

The polar diagrams reduce to a figure eight, with major axis pependicular to the strike direction (or pseudo-strike for 3D). The magnitudes for the magnetic transfer functions are high in the region of the inhomogeneity for the Reddy et al. (1977) 3D model.

The magnetic transfer functions operate on the horizontal magnetic fields to yield the vertical component. The 'tipper' magnitude, $|T|$, is;

$$|T| = (|Xzx(\omega)|^2 + |Xzy(\omega)|^2)^{1/2} \qquad D28$$

It's azimuth, ϕ, which is the angle measured from x-axis in a clockwise direction is;

$$\phi = \frac{(Ar^2+Br^2)\tan^{-1}(Br/Ar)+(Ai^2+Bi^2)\tan^{-1}(Bi/Ai)}{|T|^2} \qquad D29$$

where Ar and Br are the real parts of $Xzx(\omega)$ and $Xzy(\omega)$, and Ai and Bi are the imaginary parts (Jupp and Vozoff,

1976).

The tipper direction for a 2D case is perpendicular to the strike direction. Ting and Hohmann (1981), observed that the tipper points away from a 3D conductive inhomogeneity and the magnitudes tend to have relatively higher values near the inhomogeneity for a frequency of 10Hz compared with the values at 1Hz.

REFERENCES

Aki,K. and K.L. Larner, 1970, Surface motion of a layered medium having an irregular interface due to incident plane waves. JGR, 75,933-954.

Bard, P. and M. Bouchon,1980a, The seismic response of sediment-filled valleys. Part 1. The case of incident SH waves. BSSA, 70, 1263-1286.

Bard, P. and M. Bouchon, 1980b, The seismic response of sediment-filled valleys. Part 2. The case of incident P and SV waves. BSSA, 70, 1921-1941.

Bouchon, M., 1973, Effect of topography on surface motion. Bull. Seism. Soc. Am., 63, 615-632.

Bouchon, M. and K. Aki, 1977, Near-field of a seismic source in a layered medium with irregular interfaces. Geophys. J.R. Astr. Soc., 50,669-684.

Cagniard, L., 1953, Geophysical theory of the magnetotelluric method of geophysical prospecting. Geophysics, 18, 605-635.

d'Erceville, I. and G. Kunetz, 1962, The effect of a fault on the earth's natural electromagnetic field. Geophysics, 27, 651-665.

Dongarra, J.J., Moler, C.B., Bunch, T.R., and G.W. Stewart, 1979, Linpack User's Guide. SIAM, Philadelphia.

Goubau, W.M., Gamble, T.D. and J. Clarke, 1978, Magnetotelluric data analysis: removal of bias. Geophysics, 43, 1157-1166.

Hermance, J. F. and J. Pedersen, 1980, Deep structure of the Rio Grande Rift: a magnetotelluric interpretation. JGR, 85, 3899-3912.

Hibbs, R.D. and F.W.Jones, 1978, Electromagnetic induction in three dimensional structures for various source fields. J. Geomagnetic Geoelec., 30, 1-18.

Hohmann, G.W., 1975, Three-dimensional induced polarization

and electromagnetic modeling. Geophysics, 40, 309-324.

Hohmann, G.W. and S.C. Ting, 1978, Three-dimensional magnetotelluric modeling. ESL Final Rpt. 77-15, DOE Contract EY-76-S-071601, July, 48 P.

Jiracek, G.R., 1973, Geophysical studies of electromagnetic scattering from rough surfaces and from irregularly layered structures. Ph.D. Thesis, Univ. of California, Barkeley, Calif.

Jiracek, G. R., Ander, M. E. and H. T. Holcombe, 1979, Magnetotelluric soundings of crustal conductive zones in major continental rifts, In Rio Grande Rift: Tectonics and magmatism, ed. by R. E. Reiker, American Geophysical Union, Washington, 209-222.

Jones, F.W. and K. Vozoff, 1978, The calculation of magnetotelluric quantities for three-dimensional conductivity inhomogeneities. Geophysics,43,1167-1175.

Jupp, D.L. and K. Vozoff, 1976, Discussion on The magnetotelluric method in exploration of sedimentary basins by K. Vozoff: Geophysics, 41, 325-328.

Kaufman, A. A. and G. V. Keller, 1981, The magnetotelluric sounding method. Elservier, Amsterdam, 595pp.

Lee, K.H., Pridmore, F. and H.F. Morrison, 1981, A hybrid three-dimensional electromagnetic modeling scheme. Geophysics, 46, 796-805.

Lines, L.R. and F. W. Jones, 1973a, The Perturbation of Alternating Geomagnetic Fields Near a Coastline. Canadian Journal of Earth Sciences, vol. 10, 4, 510-518.

Lines, L.R. and F.W. Jones, 1973b, The perturbation of alternating geomagnetic fields by three-dimensional island structures. Geophysics J.R. Astr. Soc., 32, 133-154.

Mann, J.E., 1964, Magnetotelluric theory of sinusoidal interface. JGR, 69, 3517-3524.

Meyer, W.H., 1977, Computer modeling of electromagnetic prospecting methods. Ph.D. Thesis, Univ. of California, Berkeley, Calif.

Neves, A.S., 1957, The magnetotelluric method in two dimensional structures. Ph.D. dissertation , MIT.

Peeples,W.J., 1983, Magnetotelluric theory for multiple non-planar inerfaces. Submitted to Geophys. Pros.

Pridmore, D.F., 1978, Three-dimensional modeling of electromagnetic data using the finite-element method. Ph.D. Thesis, University of Utah.

Rankin, D., 1962, The magnetotelluric effect in a dike. Geophysics, 27, 666.

Rayleigh, Lord (J.W. Strutt), 1896, The theory of sound, vol. 2, 2nd ed. Macmillan, London, England.

Reddy, I.K.,Rankin, D. and R.J. Phillips, 1977, Three-dimensional modelling in magnetotelluric and magnetic variational sounding. Geophy. J.R. Astr. Soc., 51, 313-325.

Sandberg, S. K. and G. W. Hohmann, 1982, Controlled-source audiomagnetotellurics in geothermal exploration. Geophysics, 47, 100-116.

Silvester, p. and C. R. S. Haslam, 1972, Magnetotelluric modeling by the finite element method. Geophys. Pros., 20, 872-891.

Sims, W. E. and F. K. Bostick, Jr., 1969, Methods of magnetotelluric analysis, EGRL tech. rep. no. 58, Univ. of Texas, Austin.

Stanley, W. D., Boehl, J. E., Bostick, F. X., Jr., and H. W. Smith, 1977, Geothermal significance of magnetotelluric soundings in the Snake River Plain -- Yellowstone region. JGR, 82, 2501-2514.

Stodt, J. A., Hohmann, G. W. and S. C. Ting, 1981, The telluric-magnetotelluric method in two- and three-dimensional environments. Geophysics, 46, 1137-1147.

Stratton, J.A., 1941, Electromagnetic Theory. McGraw-Hill, New York.

Swift, C.M., Jr., 1967, A magnetotelluric investigation of an electrical conductivity anomaly in the southwestern United States. Ph.D. dissertation, MIT.

Tichonov, A.H., 1950, Determination of the electrical characteristics of the deep strata of the earth's crust. Dokladi, Akad. Sci., v. LXXIII,295.

Ting, S.C. and G.W. Hohmann, 1981, Integral equation modeling of three-dimensional magnetotelluric response. Geophysics, 46, 182- 197.

Vozoff, K., 1972, The magnetotelluric method in the exploration of sedimentary basins. Geophysics,37, 98-141.

Wannamaker, P.E., Ward, S. H. and G. W. Hohmann, 1982, Magnetotelluric responses of three-dimensional bodies in layered earths. Univ. Utah, Dept. Geology, DOE-ID12079-87, 83p.

Ward, S. H., 1980, Electrical, electromagnetic and magnetotelluric methods. Geophysics, 45, 1659-1666.

Ward, S. H., Peeples, W. J. and J. Ryu, 1973, Analysis of Geoelectromagnetic Data; in Methods of Computational Physics, vol. 13, 163-238, Academic Press, New York.

Weidelt, P., 1975, Electromagnetic induction in three-dimensional inhomogeneities. Geophysics, 36, 38-52.